Controlling Nanostructure for Catalytic and Electrochemical Energy Storage Materials

by

Tapiwa Mushove

A dissertation submitted in partial fulfillment
of the requirements of the degree of
Doctor of Philosophy
(Materials Science and Engineering)
in The University of Michigan
2016

Doctoral Committee:

Professor Levi Theodore Thompson Jr., Co-Chair
Professor Katsuyo S. Thornton, Co-Chair
Associate Professor Bart Bartlett
Associate Professor Pierre Ferdinand Poudeu-Poudeu
Associate Professor Pramod Sangi Reddy

2016

Dedication

To my parents, my family, and my teachers.

Acknowledgements

I would like to thank my advisor, Professor Levi Thompson for his patience, support and mentorship through my PhD work in his research group. He was always honest in his assessment of my work. The projects were challenging, yet very exciting. Prof. T's expectations were always high, and I hope I rose high enough to meet them. Major lessons I learned from Prof. T. were to listen to ideas and critiques from others and to adapt to new and changing challenges of the scientific environment. I loved going into the lab and exchanging ideas with Prof. T. and his talented students during weekly subgroup and group meetings. I will always remember and cherish my time working under Prof. T and am very glad I joined his group. Like Prof. T says, once you are in the group, you stay in the group. Thanks Levi.

I would also like to thank Professor Emeritus Paul Rasmussen. Prof. R allowed me to bother him about a broad range of subjects. He was always keen to answer my questions, and his answers were always insightful. I valued all the discussions I had with him.

I also want to thank my doctoral committee. Professor Katsuyo Thornton, in her role as co-chair, was immensely helpful and patient in helping produce this dissertation. Her critiques and edits were very valuable and I appreciate all the effort and time she put into helping improve my work. Professor Bart Bartlett was helpful in providing critiques on the chemistry part of this dissertation. Her former student Dr. Tanya Breault, who I closely worked with for two years, greatly improved the quality of this work. Professor Ferdinand Poudeu, was a great resource in assessing my work on battery materials, and I appreciate the chats I had with him over various

topics, which even included soccer. Professor Pramod Reddy, with his broad knowledge on nanoscale materials, helped critique various aspects of this work.

My favorite teachers in the past: Trymore Makaza from high school math, and Professor Richard Fell, a great mentor, whose physics courses I enjoyed taking in college shaped my understanding of physics and approaching science. I also appreciate the great conversations I had with Prof. Fell.

I would like to thank all former and present members of the Thompson Research Group, and others outside the group who helped make this work possible. My professional and social interactions with them helped improve my understanding of science and research methods. These include Dr. Saemin Choi, Dr. Alice Sleightholme, Dr. Richard Memie Ezike, Dr. Kanako Okada, Dr. Aaron Shinkle, Dr. Priyanka Pande, Dr. Binay Prasad, Dr. Gaowei Wang, Dr. Tanya Breault, Dr. Peter Aurora, Steven Blodgette, Dr. Jason Gaudet, Dr. Krista Hawthorne, Dr. Wes Brogden, Dr. Yuan Chen, Allison Franck, Ryan Franck, Dr Hui-Chia Yu, Brian Wyvratt, Abdoulaye "Glaye" Djire, Jonathan Kucharyson, Anisha Rehlan, Siu on Tung, Jee-Jay Chen, Wei-Chung Winn Wen, Scott Johnson, Sarah Paleg, Sarah Carl, Olabode Ajenifuja, and Sydney Laramie . In addition, I would like to thank the following high school and undergraduate students: Alex Reeves and Wei Tan. My friends outside the lab were crucial in maintaining a balanced lifestyle: Dr. Arlyne Simon, Yasmine Doleyres, Abdoulaye "Glaye" Djire, Dr. Ben Torralva, Dr. Yioryos Nardis, Milan Paunovic, Dr. Andres Milan, Pride Mudzvova, Max Dogbatse, Rod McPherson, Aiste Socikaite, Mounir Blibeche, Nate Watson, Eongyu Alex Yi, Kevin Kretchmer, Dr. Nate Taylor, Dr. Seyram Avle, Andrew "ACE" Eilbert, Ibrahim Boulares, Casey Steur, Casey Bantle, Kartheek Gangadharra, Julie Prinet, Pratap Sankar, Peter Orchard, Suraj Ramani, Albert Chiwara, Tawanda Chaunzwa, Munyaradzi Chaunzwa, Hillary "Fellow" Masuka, Dustin Smith,

Peter Macko, Joshua “The Boston Josh” Roach, Andrew Mayers, Martin “Dago” Fungura, Collins Tembani, Dunmore Zungu, Eugene Wolfson, Prof. Matt Backus, Ashwin Manthena, and many others whose contributions to my personal growth were so immense.

My funding sources: the National Science Foundation and the US Department of Energy, were crucial in making this dissertation possible. The Electron Microscopy Analysis Lab at the University of Michigan was also very helpful in my research, in particular John Mansfield, Beverly Clampit, Kai Sun, and Haiping Sun. This work would have been impossible without the support from the Materials Science and Engineering department: Renee Hilgendorf, thank you so much for all your help. Harald Eberhart, Shelley Fellers, and Prof. Peter Green were a great help as well. Barbara Perry from the Chemical Engineering department was also very helpful throughout my program.

And to my father, my mother, and siblings, thank you for the support and love always. My father’s immortal saying “read, and read, and read” has kept my keenness in the pursuit of understanding science and nature strong since I was a little boy. Thank you.

Table of Contents

List of Figures

List of Tables

Chapter 1

Introduction: Nanostructuring in Catalytic and Electrochemical Energy Storage Materials

1.1 Motivation

Increased demand for energy is driving increased consumption of fossil fuels [1-2]. While fossil fuels are readily available and relatively inexpensive, their combustion results in the emission of greenhouse gases, which have been linked to global climate change [3]. Increased public awareness that fossil fuels are not an inexhaustible energy source and a growing need to reduce the dependence on foreign oil reserves, is driving efforts towards the large-scale integration of renewable energy into the grid [4-5]. In its 2007 *Energy Independence and Security Act*, the United States government outlined the need for increased production and integration of clean, environmentally friendly, sustainable, and renewable fuels into the country's energy portfolio [6]. Since then, research efforts towards a fundamental understanding of conversion systems for renewable energy sources such as solar, wind, geothermal, and tidal power have been dramatically increased [7-9].

The utilization of renewable sources is inherently entangled with the need for efficient storage systems, as production and peak consumption typically occur out of phase with one another. Advanced grid energy storage systems may provide new solutions to energy needs by collecting excess energy during low demand and releasing it during high demand, reducing the

required peak capacity of power generation facilities and allowing those facilities to deliver at their most efficient output levels. Therefore, advancements of electrical energy storage systems have also become necessary. As such, electrochemical energy storage is now a very active research area.

In addition to the integration of renewables and energy storage into the power grid, the control of greenhouse emissions has been identified as a key area of research towards the creation of a sustainable energy future [6]. A variety of heterogeneous catalysts have been applied towards the capture and conversion of greenhouse gases into environmentally friendly products, as well as in chemical conversion for energy applications and food production. Research efforts in the field of heterogeneous catalysis have mainly aimed to develop catalysts with improved reaction yields and reaction selectivities towards desirable products [10]. The major challenge for new, economically viable catalytic and electrochemical energy storage devices is the poor conversion efficiency that plagues the materials currently in use [8-10]. Materials with precisely controlled nanostructures hold promise towards significantly enhancing the efficiencies of next-generation systems for catalytic chemical conversions and energy storage due to improved electrochemical surface areas, surface reaction rates, and short charge transport distances [9-13].

There is already a large body of literature describing a variety of materials that benefit significantly in performance due to nanostructuring. For instance, Wang et al. demonstrated the quadrupling of the water photo-oxidation rate of a hematite nanonet-based device architecture over a simple planar electrode as a result of improved charge transport in the nanostructured material [14]. In electrochemical energy storage, the nanostructured version of the phospho-olivine $LiFePO_4$ possesses electrochemical performance properties that are significantly

improved over conventional materials due to the increased accessibility of the low diffusion energy [010] crystallographic directions [15]. Another important characteristic for nanoscale materials is the variation in the surface energies based on the crystallographic facets exposed to reactants. Li et al. utilized this effect to control the relative reaction rates of silver nanocatalysts for styrene oxidation using nanoplate, nanosphere, and nanocube nanostructures [13].

This chapter provides motivation for our research to develop efficient materials systems for photocatalysis, electrochemical energy storage, and heterogeneous catalysis. It then provides an overview of nanostructure control considered in the literature for each of these systems and addresses several specific examples of nanostructured materials. The aim is to control nanostructure using light and electrochemical driving forces and to develop structure-function relationships for these systems. The research goals and organization of this dissertation are outlined at the end of the chapter.

1.2 Solar Water Photo-Oxidation

Among renewables, solar is one of the most promising and abundant energy sources. The total solar influx reaching the earth's surface is estimated at $3x10^{24}$ J/yr, which is approximately 10^4 times the current total global energy consumption [16]. Therefore, even if only a very small fraction of the solar influx can be efficiently harvested, current energy demands could be met. Solar energy consumption rose by a remarkable 50%, the highest average percentage increase recorded among all renewables, between 2009 and 2014 [1]. The surge in the growth rate of solar energy harvesting has been spurred by the promise of inexpensive, clean energy. Solar energy harvesting has been dominated by traditional solid-state solar technologies based on silicon; however, the abundance of water on the surface of the planet has driven the development of various other technologies to convert solar energy into chemical fuels. In 1972, using a

semiconducting TiO_2 electrode, Fujishima and Honda reported the Honda-Fujishima effect, or the photo-oxidation of water using ultraviolet radiation from the sun, forming hydrogen fuel along with oxygen [17]. Since the publication of Fujishima's work, there has been a sustained effort to identify and engineer new materials for more efficient photoelectrochemical cell (PEC) systems. Hydrogen has long been used as a combustion fuel for space shuttles, as a feedstock in the chemical and petroleum refining industries, and more recently as a fuel in fuel cells [18]. Some major advantages of using hydrogen produced from PECs as a fuel source are that it is inexpensive, environmentally friendly, energy dense (143 MJ/kg), and sustainable [18-19]. PECs can be easily constructed from inexpensive materials, making them an economical alternative to traditional photovoltaic solar harvesting systems [16]. However, the main challenge to the widespread implementation of PECs is the poor conversion efficiency of photoanode materials currently being used in these devices [8]. The next section introduces the concept of PECs, their advantages, as well as their limitations.

1.2.1 Photoelectrochemical Cells

Photoelectrochemical cells combine photo- and electro-catalytic functions to convert solar energy into chemical energy. For example, these devices have been extensively studied for the photoelectrolysis of water to hydrogen and oxygen [16, 20-25]. A common type of PEC cell incorporates a semiconductor photoanode immersed in an aqueous electrolyte [22-23]. The counter electrode is typically platinum metal, but can be another photoelectrode as well. The purpose of the electrolyte is to conduct ions during the redox processes occurring at the electrodes. Figure 1.1 shows a schematic representation of a PEC constructed from a semiconductor photoanode and a metal counter electrode, as well as the energy band potentials of an ideal semiconductor relative to the water splitting half-reaction potentials [22-23].

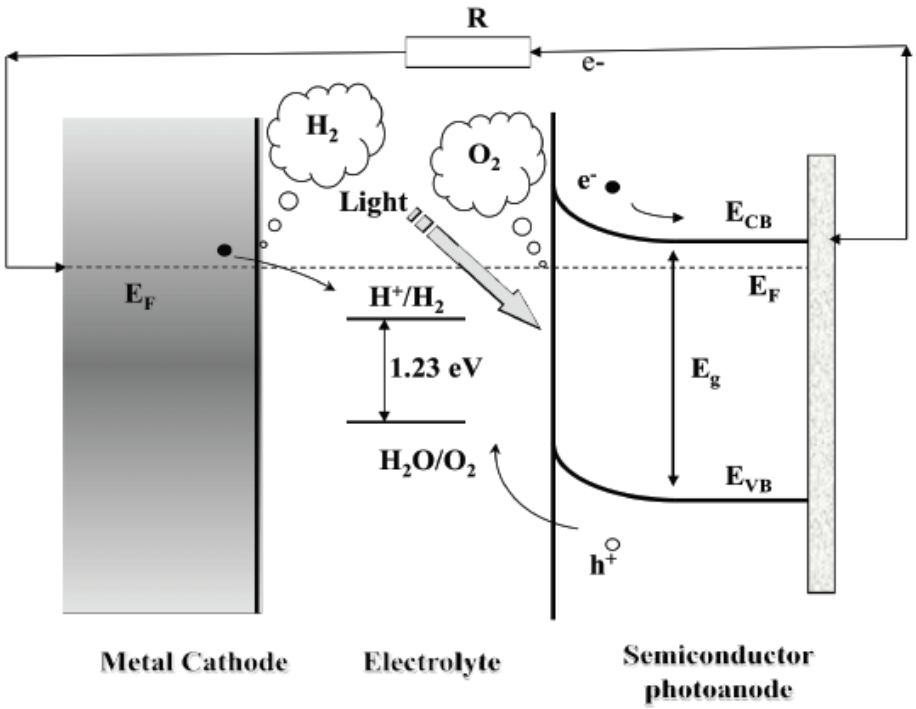

Figure 1.1: Schematic of a photoelectrochemical cell. Photogenerated charges react with water molecules and protons at the electrode surfaces, forming hydrogen fuel and oxygen [22-23].

Upon illumination of the photoanode with photons of energy higher than the semiconductor energy bandgap, an electron-hole pair is generated from the excitation of electrons from the valence band to the conduction band, according to equation (1.1):

$$h\upsilon \rightsquigarrow e^- + h^+ \qquad (1.1)$$

The application of an electric field bias across the photoanode drives the photogenerated electrons in the conduction band through the external circuit. Simultaneously, the photogenerated holes diffuse through the photoanode bulk towards the semiconductor-electrolyte interface, where they photo-oxidize water molecules, forming $H^+_{(aq)}$ ions:

$$2H_2O_{(aq)} + 4h^+ \rightarrow O_{2(g)} + 4H^+ \qquad (1.2)$$

At the counter-electrode/electrolyte interface, the $H^+_{(aq)}$ ions are reduced by the photogenerated electrons, forming the desired product, $H_{2(g)}$:

$$4H^{+}_{(aq)} + 4e^{-} \rightarrow 2H_{2(g)} \qquad (1.3)$$

Overall, this type of PEC utilizes solar irradiation to split water into oxygen and hydrogen gases:

$$2H_2O_{(aq)} \xrightarrow{h\nu} O_{2(g)} + 2H_{2(g)} \qquad (1.4)$$

Although the thermodynamic requirement of this reaction is only 1.23 eV/electron, kinetic limitations, internal cell resistances, and overpotentials at the electrodes or in the external circuit of the PEC (on the order of 0.8 eV) [24], increase the activation barriers for the reaction, pushing the overall practical energy requirement to $\gtrsim$ 2.1 eV. A major obstacle to the widespread implementation of PECs is their poor overall efficiency and the need for identification of more efficient photoanode materials able to provide higher solar absorptivities and photocatalytic conversion efficiencies [8, 20]. Materials selection and engineering are key challenges for improved PEC performance.

1.2.2 Materials Selection for Photoelectrochemical Cells

Desirable properties for a photoelectrode material for spontaneous and efficient photoelectrochemical water splitting include:

(i) a bandgap of ~2.0 eV, slightly higher than the thermodynamic water splitting energy of 1.23 eV (equivalent to photons of 1008 nm wavelength), yet low enough to capture a significant portion of the solar spectrum

(ii) photostability and photocorrosion resistance in aqueous media [16, 25]

(iii) energy band potentials straddling the $H^{+}_{(aq)}/H_{2(g)}$ and $O^{2-}_{(aq)}/O_{2(g)}$ reactions [21-22]

(iv) low recombination rates [8, 26]. (Photogenerated electrons have a finite residence time in the conduction band, eventually decaying back into the valence band through the process of recombination).

A variety of materials, principally transition metal oxides, have been investigated for use as photoelectrodes for water oxidation [8, 16, 20, 25, 27-29]. To date, identifying a material that simultaneously meets all aforementioned requirements has proven to be a major challenge. High bandgap materials, such as zinc oxide (ZnO), tin oxide (SnO_2), titanium dioxide (TiO_2) and silicon carbide (SiC), typically show good stability against photocorrosion in aqueous solutions. However, these materials can only utilize a small portion of the solar spectrum (in the ultraviolet region) towards water photo-oxidation [16]. On the other hand, materials with relatively low bandgaps such as hematite ($\propto$-Fe_2O_3) and tungsten trioxide (WO_3) exhibit excellent solar absorption properties. Because hematite has a bandgap that is almost ideal for solar water splitting (~2.1 eV), significant attention has been devoted to this material. Hematite is also resistant to photocorrosion in alkaline electrolytes, allowing for long-term stability. In addition, the abundance of iron in the Earth's crust and its non-toxicity make hematite an inexpensive, environmentally friendly alternative photoanode material for PECs. However, hematite requires an external potential bias to drive the hydrogen evolution reaction due to the mismatch between its conduction band and the hydrogen evolution potential [29-31]. In addition, the hole diffusion length (2-4 nm) [29-31] for hematite is an order of magnitude smaller than the absorption depth of the material. Coupled with its poor electron conductivity [20], this results in high electron-hole recombination rates, thus significantly reducing the photoconversion efficiencies of the bulk material [20, 26, 29].

Several non-oxides, such as GaP, GaAs, CdSe, and CdS, have also been identified for PEC applications, based on their low bandgaps and good light absorption properties. However, these materials showed poor photocorrosion resistance in aqueous media and are therefore not ideal for PEC applications [16].

Researchers have explored a variety of other approaches to improve the photoconversion efficiencies of PECs. One such approach is to enhance solar absorption and utilization through the use of multi-junction systems, where multiple layers of semiconducting materials with different bandgaps are stacked in one device. The materials are stacked in such a way that the topmost layers absorb high energy photons, while lower energy photons are absorbed in the lower bandgap materials in the layers below [21, 32]. Materials that are not photocorrosion resistant are typically placed within the device architecture, out of contact with the electrolyte. This approach, however, suffers from the major disadvantage of increased electron-hole recombination rates, which lowers the overall efficiency [21, 32].

Another approach to increase photoconversion efficiency is to reduce the bandgap of wide bandgap materials through various bandgap engineering techniques. For example, the electronic structures of materials can be manipulated via doping with aliovalent ions, resulting in the formation of intermediate energy bands slightly above the valence band [33-34] and thus allowing for the absorption of photons from the visible part of the solar spectrum. However, the dopants were shown to act as recombination centers [35], with their detrimental effects to photoconversion efficiency outweighing the advantages of the intermediate band states. Therefore, this approach has not been as widely adopted for increased photoconversion efficiency.

1.2.3 Nanostructure Control for Enhanced Photoelectrochemical Cell Photoanode Performance

Another popular approach to increase PEC efficiency is to decouple the long photon absorption depths from short diffusion distances through nanostructuring. The ideal result is materials that are thick enough for complete light absorption but thin enough to allow

photogenerated charges to efficiently diffuse to the electrode-electrolyte interface. Many previous efforts with hematite have focused on enhancing its performance through nanostructuring [20]. For example, nanorods [26-27, 39], nanoleaves [28], and nanotubes [36], can place the photogenerated holes within the hole diffusion length of the oxide-electrolyte interface, thereby reducing recombination losses [20, 26]. Nanotubes also allow for a significant increase in the surface area available for contact with the electrolyte, while confining charge transport to one dimension, thus reducing the potential for recombination [29-30]. Wang et al. reported that nanonet-structured hematite electrodes, coupled with a highly conductive TiS_2 coating, possessed incident photon to current efficiencies (IPCE) that were more than double those for the corresponding planar electrodes, emphasizing the crucial role played by nanostructuring and conductive additives [14].

Durrant et al. investigated the use of hematite nanoparticles and identified the ultrafast recombination dynamics as a major concern to the adoption of the morphology for PEC applications [37]. In addition, photogenerated electron transport in nanoparticles was shown to follow tortuous pathways, further increasing the likelihood of electron-hole recombination [38].

Hagfeldt et al. employed a precipitation technique to synthesize one-dimensional hematite nanorod arrays with diameters varying from 10-40 nm and thicknesses in the 100-1500 μm range. The arrays were perpendicular to the attached iron substrates. These nanorod arrays achieve an IPCE of 5% at 360 nm. This relatively high IPCE (in comparison to planar electrodes) for pure hematite was ascribed to electrochemical surface area enhancements afforded by the nanorod morphology, sufficient photon absorption due to increased thicknesses of the nanostructure, and the direct pathways provided by the nanorod morphology [39]. Another report detailed the synthesis of hematite nanorod arrays via the direct thermal oxidation of iron

foils [40], yielding nanorods with diameters of 20-40 nm and lengths up to 5000 μm. However, photoelectrodes synthesized through this route were shown to suffer poor performance due to high densities of defects, leading to increased recombination rates [39-41].

In efforts to synthesize hematite nanostructures with high electrochemical surface areas, one-dimensional photogenerated charge transport, and short hole diffusion lengths, Grimes et al. employed an electrochemical anodization technique [36]. They reported the rapid self-assembly of ordered, vertically-oriented iron oxide nanotube arrays after the potentiostatic anodization (in the 30-60 V potential range) of high-purity iron foils in an ammonium-fluoride containing ethylene glycol/water electrolytic solution. A high temperature thermal treatment was required to crystallize the nanotubes into the photoactive hematite phase. Individual nanotubes were smooth and straight, with pore diameters of 30-80 nm, wall thicknesses of ~5-6 nm, and lengths of 1-3.5 μm. This material architecture allowed for sufficient absorption of light [36], charge photogeneration within the hole diffusion range of the electrolyte, and the efficient transport of photogenerated charges. IPCE values of 3.5% at 350 nm were reported, consistent with pure hematite nanotube arrays reported elsewhere [42]. Importantly, using this synthetic technique, Grimes et al. demonstrated precise control over the nanotube diameter, which was found to be a linear function of the anodization voltage (in the 30-60 V range), as well as the nanotube length, which was a linear function of the electrolyte bath temperature in the 25 – 60 °C range. Grimes and co-workers' success in controlling the hematite nanotube morphology offers an opportunity to further study and understand the correlation between nanostructure/properties and the performance of nanotube array architectures. Aurora reported similar trends with regard to titania nanotube array lengths during the electrochemical anodization of titanium foils [43].

With regard to PECs for water photo-oxidation, our research seeks to synthesize hematite nanotube arrays with controlled morphologies using the electrochemical anodization technique demonstrated by Grimes [36] and Aurora [43]. We start with a systematic investigation of the effect of synthesis conditions on properties of the nanotube arrays. Using the resulting materials, we were able to correlate the array structures and properties to their function and performance. Ultimately, the goal is to develop general design rules for the fabrication of hematite photoanodes with superior performance characteristics for photoelectrochemical water splitting. We developed hematite nanotube arrays with two novel morphologies: multilayer and wave-like. Fujimoto et al. electrochemically synthesized multilayer stacks of InP and suggested that they might be applicable as Braggs reflectors [21]. Therefore, we hypothesized that the multilayer nanotube arrays would improve photocatalytic performance as a consequence of enhanced light absorption at the layer interfaces. The wavelike nanotubes were expected to possess increased electrochemical surface areas compared to straight nanotubes, thereby enhancing photocatalytic rates [45].

1.3 Electrochemical Energy Storage

As discussed earlier, increased interest in renewable energy harvesting is driving the development of next-generation electrochemical energy storage (EES) systems. Energy storage systems are diverse, and their development is typically tailored to the requirements of the application. Systems are being developed for the electric grid, electricification of vehicles, as well as portable electronics with enhanced runtimes [46]. The following sections review the literature regarding the development of materials for high-performance electrochemical storage devices, thus setting the stage for our own research efforts to further advance the understanding and development of these devices.

1.3.1 Types and Storage Mechanisms of Electrochemical Energy Storage Systems

Secondary lithium ion batteries and capacitors are among the most widely used devices for electrochemical energy storage applications. Secondary lithium ion battery materials store charge through the reversible intercalation of Li^+ ions in the interstitial sites or crystallographic planes within a bulk electrode material and typically exhibit energy densities in the 150 - 300 mAh/g range, very high in comparison to those of capacitors [47-48]. However, bulk charge storage and poor ionic diffusivities reported for Li^+ ions in the solid state [49] result in kinetic and transport limitations that lower the rate of charge extraction and power densities of these battery materials. In addition, bulk Li^+ ion intercalation results in stresses during cycling and can result in diminished structural integrity over time. The typical lifetime of lithium ion battery materials is on the order of 300 cycles, a relatively short cycle-life compared to those for other electrochemical devices such as capacitors [48]. These performance characteristics limit batteries to applications requiring slow charge/discharge rates [48-49].

Electrochemical double layer capacitors (EDLC) store charge through the non-Faradaic adsorption of electrolyte ions on the surface of the electrode material, forming an electric double layer. Double layer capacitors utilize very high surface area materials such as activated carbon, allowing them to store large amounts of charge at their surfaces [50-52]. Because charge storage is limited to the surface, high rate charge extraction, and hence high power densities, can be achieved [50-52]. Also, due to the lack of bulk storage, the structural integrity of the materials is maintained over thousands and in some cases millions of charge/discharge cycles. However, because charge storage is limited to the electrode surface, the energy density of EDLCs is low in comparison to batteries. Published energy densities are typically less than 10 Wh/kg [52].

EDLCs are very effective for short-pulse, high power applications such as the rapid acceleration of automobiles and trucks and flashlights on cameras [51].

In the quest to accelerate the development of clean transportation systems, the United States Department of Energy is spearheading efforts to identify and develop electrochemical energy storage materials that combine the high energy densities of battery materials with the fast charge transport, high rate power deliveries, and high cycle lives of supercapacitor materials [50, 52]. Recent research efforts aimed at reaching this goal have focused on enhancing the power densities of battery materials and increasing the energy densities of capacitor materials [53-57]. A relatively new class of materials, termed "intercalation pseudocapacitors," has been identified. These materials enable significant bulk charge storage. Because they exhibit fast, long-range charge transport through low energy diffusion pathways, the power densities of devices incorporating these materials can be high. In essence, this class of materials combines the high energy densities of battery materials with the high rates typically seen only for supercapacitor materials. Figure 1.2 depicts the energy storage mechanisms of batteries, supercapacitors, and intercalation pseudocapacitors.

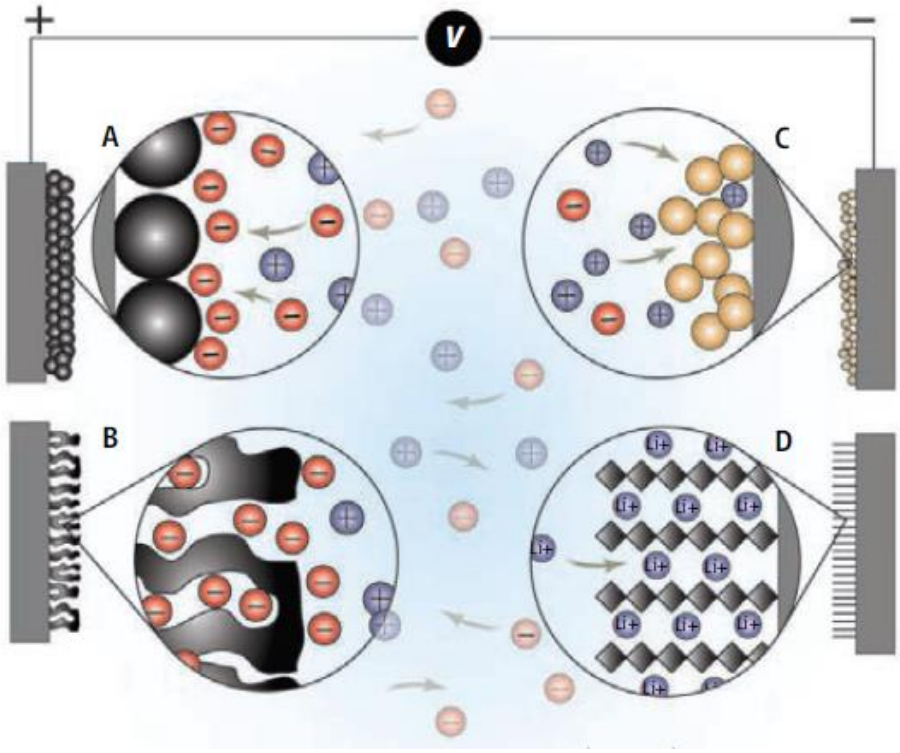

Figure 1.2: Various electrochemical storage mechanisms for: a/b) electric double layer capacitors, c) redox pseudocapacitors, d) battery materials and intercalation pseudocapacitors. The dominant storage mechanism typically dictates the capacity and rate performance characteristics of a material [50].

1.3.2 Nanostructured Materials for Electrochemical Energy Storage Systems

Materials with carefully controlled nanostructures offer a pathway towards high-rate, high-energy performance through enhancements in kinetic and transport characteristics realized at the nanoscale [53-57]. The characteristic timescale for Li^+ diffusion in a solid cathode is defined as $\tau = L^2/D$, where L is the characteristic length, and D is the diffusion coefficient of Li^+ in the material [53]. Therefore, a decrease in the characteristic material feature size results in a significant reduction in the ion diffusion timescale. In general, nanostructuring increases the electrochemical surface area of a material [11, 53]. However, it has even more pronounced effects for some materials. In these cases, such as $LiFePO_4$, anisotropic morphologies can also be

important, and higher surface areas can lead to increased accessibility of the specific diffusion channels that are energetically favorable for intercalation [15, 58].

An interesting case study of nanostructuring in electrochemical energy materials is the phospho-olivine, $LiFePO_4$, a material of little practical significance in bulk despite its low cost and good electrochemical stability. When pulverized to nanoparticulate sizes, $LiFePO_4$ demonstrates dramatic improvements in electrochemical kinetics. Transport in $LiFePO_4$ is highly anisotropic, with Li^+ ion diffusion constrained to the {010} family of crystallographic channels. The presence of only a few defects in the crystal structure results in the blocking of these diffusion channels, hindering lithiation/de-lithiation and significantly lowering the capacity of the bulk version of the material. By reducing the particle size of $LiFePO_4$, the increased accessibility of the desired {010} channels, reduced ion path lengths, and a reduced effect of channel blockage by defects lead to capacity enhancements [15, 58]. Because of nanostructuring, $LiFePO_4$ can possess high ionic conductivities and good electrochemical performance [15, 58]. In fact, nanostructured $LiFePO_4$ is one of the most reliable, high performing battery materials currently on the market [51].

Another interesting effect that is unique to battery materials at the nanoscale and does not appear in the bulk counterparts is in silicon-based materials for battery anodes. At ~4200 mAh/g, Si possesses one of the highest specific capacities among materials investigated for use in lithium ion battery anodes; in particular, the capacity of Si is an order of magnitude higher than that of graphite, the current commercial standard [59]. However, Si undergoes an extreme volume expansion of ~400% during electrochemical cycling. Repeated stress cycling causes rapid pulverization, structural disintegration, and massive capacity fading in the electrodes, making their practicality a major challenge [59-60]. Nevertheless, substantial progress has been reported

in the use of these materials when applied in their nanostructured forms. Nanotube and nanowire arrays, as well as hollow nanospheres, were demonstrated to improve degradation due to lithiation in Si anodes. The stress was reduced by allowing the volume expansion to proceed inwards in the case of the hollow nanospheres or nanotubes, or outwards in the case of nanorod arrays [60]. Park et al. reported excellent performance for nanotubular Si, with a capacity of ~3200 mAh/g and a capacity retention of 89% after 200 charge/discharge cycles at 1C [48]. The discharge rate represents the total time it takes to fully discharge the electrode; for instance, a rate of *n*C indicates that it takes 1/*n* hours to fully discharge the electrode.

1.3.3 Nb_2O_5 Materials for Lithium-Ion Insertion

One promising intercalation material is niobium pentoxide in its orthorhombic phase, T-Nb_2O_5 [61-62]. The 'T' stands for 'tief,' which is German for 'low,' as this material phase is typically attained via the low temperature thermal treatment of amorphous Nb_2O_5. T-Nb_2O_5 was demonstrated to exhibit relatively high capacities of ~110 mAh/g at discharge rates as high as 100C when mixed with carbon black [61-62]. These capacities are typical of battery materials, and the discharge rates are closer to those of supercapacitors, making T-Nb_2O_5 an attractive material for high energy and high power applications. However, a major disadvantage of T-Nb_2O_5 is its poor electrical conductivity (3.4×10^{-6} S/cm at 300 K) [63]. Significant electrochemical performance improvements were reported with modifications such as the addition of carbon black [62]. Dunn et al. demonstrated significant enhancements in the kinetics of lithium transport in mesoporous, nanocrystalline T-Nb_2O_5, attributing these enhancements to improved electron and ion transport due to the shortened Li^+ ion diffusion lengths in nanostructured T-Nb_2O_5, coupled with improved intercalation of Li^+ ions due to increased electrochemically active surface areas [61].

To date, there are no reports of Nb_2O_5 electrodes produced in the nanotubular geometries. Drawing from our experience with electrochemical anodization techniques to synthesize electrodes with carefully controlled nanostructures [64], we fabricated Nb_2O_5 electrodes with planar and nanotubular morphologies. In efforts to further understand the storage mechanism in nanostructured T-Nb_2O_5, we investigated the effect of nanostructuring in this material on key electrochemical performance metrics. Our investigations will also help guide efforts towards high performing electrochemical energy storage devices.

1.4 Photo-Driven Nanostructure Control

Previous sections explored the use of nanostructured materials for PEC and EES applications. Techniques for the fabrication of these materials included precipitation [39], thermal oxidation [40], and electrochemical anodization [36]. Nanostructuring can lead to significant increases in the active surface areas and a reduction in electron/hole and electron/ion transport distances; these in turn can enhance the performance of PEC and EES materials. Increased surface areas and modifications of nanoparticle shape are also important in heterogeneous catalysis, where performance can be structure-sensitive for some reactions [13]. In a number of cases, the observed structural sensitivity has been attributed to variations in the crystallographic facets at the surface; this affects the molecular adsorption modes of the reactants and energy barriers for the reactions [10, 13]. The control of nanostructure using light is a relatively new field of study, which is very promising for many fields, among them, heterogeneous catalysis [10].

Heterogeneous catalysis plays a major role in the production of a variety of chemicals, pollution control, and energy applications [65-66]. Traditional catalyst synthesis methods such as impregnation techniques have limited control over morphologies of the materials, resulting in

suboptimal reaction rates and product selectivities. The following sections detail our efforts to utilize light towards controlling nanostructure in order to understand structure-function relations for heterogeneous catalysts as applied to the catalytic hydrogenation of α,β-unsaturated aldehydes.

1.4.1 Selective Hydrogenation of α,β-Unsaturated Aldehydes

Unsaturated alcohols are important intermediates in the synthesis of various chemicals [65]. Unsaturated alcohols are produced via the hydrogenation of α,β-unsaturated aldehydes; this requires preferential hydrogenation of the C=O group over the C=C group, a very difficult selectivity to achieve. Extensive research efforts have been devoted to the development of catalysts with high rates and selectivities for C=O hydrogenation over C=C hydrogenation. Figure 1.3 shows reaction pathways for the hydrogenation of crotonaldehyde, a model α,β-unsaturated aldehyde. Crotonaldehyde hydrogenation reaction is a simple and attractive reaction to test the activities and selectivities for various catalysts.

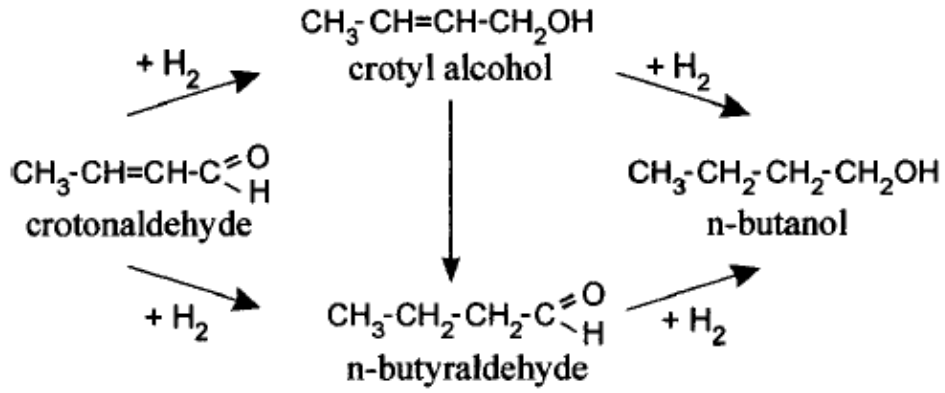

Figure 1.3: Reaction scheme for crotonaldehyde hydrogenation [65]. Different catalysts show variations in conversion rates and product selectivities.

The development of heterogeneous catalysts for chemoselective hydrogenations has focused on controlling nanoparticle shape [10, 13] and size [66-67]. Controlling size allows for

control over the fraction of crystallographic facets exposed to the reactants; this influences the reaction rates and selectivities due to the varying surface energies and reactant adsorption modes [66-67]. For instance, in the gas-phase hydrogenation of crotonaldehyde, high-index planes of nanosized Pt have been shown to be much more reactive than lower index planes due to differences in the densities of surface atoms [68]. Different shapes lead to changes of the crystallographic facets that are exposed to reactants [13].

Lercher et al. reported a significant increase in the selectivity (from 45 to 64%) towards the crotyl alcohol with increasing Pt particle size (from clusters composed of 10 atoms to clusters composed of 1000 atoms) for Pt/TiO_2 catalysts during the gas-phase hydrogenation of crotonaldehyde [68]. They attributed this effect to the higher fraction of Pt(111) facets with increased particle size; these facets favor the adsorption of crotonaldehyde via the C=O group, thus increasing selectivity towards the unsaturated alcohol. The structure sensitivity of the crotonaldehyde hydrogenation has also been reported from studies of single crystal surfaces. Pt(111) surfaces yielded a 65% selectivity (at 10% conversion) towards the crotyl alcohol, while the Pt(110) surface had a selectivity of 63% towards butyraldehyde [69]. Similarly, Hofmeister reported enhancements in the specific activities of Ag/TiO_2 catalysts for crotonaldehyde hydrogenation; there was a marked increase in selectivity towards crotyl alcohol from 28 to 53% for catalysts containing Ag nanoparticles between 1.4 and 3 nm [65]. While there are examples of structure sensitivity for α,β unsaturated aldehyde hydrogenations, the reaction is structure insensitive for some catalysts. Touroude reported the highly selective hydrogenation (60-70% at 5-50% conversion) of crotonaldehyde to crotyl alcohol using a Au/TiO_2 catalyst. However, the reaction was reported to be independent of Au particle size, suggesting structure independence in this case [70].

1.4.2 Light-Induced Control of Metal Nanoparticle Shape and Size

The most widely used methods to synthesize noble metal nanoparticles with some degree of nanostructure control involve chemical synthesis with harsh reducing and capping agents such as sodium tetrafluoroborate ($NaBH_4$) [66] and 1-butyl-3-methylimidazolium tetrafluoroborate ([BMIM][BF_4]) [71],polyvinylpyrrolidone (PVP) [72], oleylamine, and tetradecyltrimethylammonium bromide (TTAB) [73]. Light is an inexpensive alternative tool for noble metal nanoparticle synthesis. Noble metal photodeposition has been demonstrated for a variety of semiconductor supports (SCS) [74-79]. Zheng et al. showed that in addition to simple photodeposition, light can also induce shape transformation for colloidal Ag metal nanocrystals. They demonstrated the truncation of Ag nanospheres into nanoprisms with controlled edge length. They also reported a linear dependence of prism edge length on incident photon wavelength and a shape dependence on illumination time [80]. Amal deposited small spherical Pt nanoparticles (2 – 3 nm diameter) under UV light ($\lambda < 360$ nm) [78]. In the same study, visible light ($\lambda > 420$ nm) irradiation was used to deposit larger Pt nanoparticles (5 – 10 nm diameter), suggesting a dependence of Pt nanoparticle size on incident photon wavelength [78]. In a separate study, Scaiano and co-workers reported the facile photochemical synthesis of Ag nanoparticles of varying shape (including dodecahedra, nanorods, nanoplates) by varying the wavelength of incident light (Figure 1.4) [81]. As demonstrated in these studies, the use of light to control the shape or size of noble metal nanoparticles has been widely reported. However, the simultaneous control of both nanoparticle shape and size in a photodeposition process has not been achieved. Moreover, a fundamental understanding of the mechanism behind the control of the shape of the metal nanoparticles using light is currently lacking.

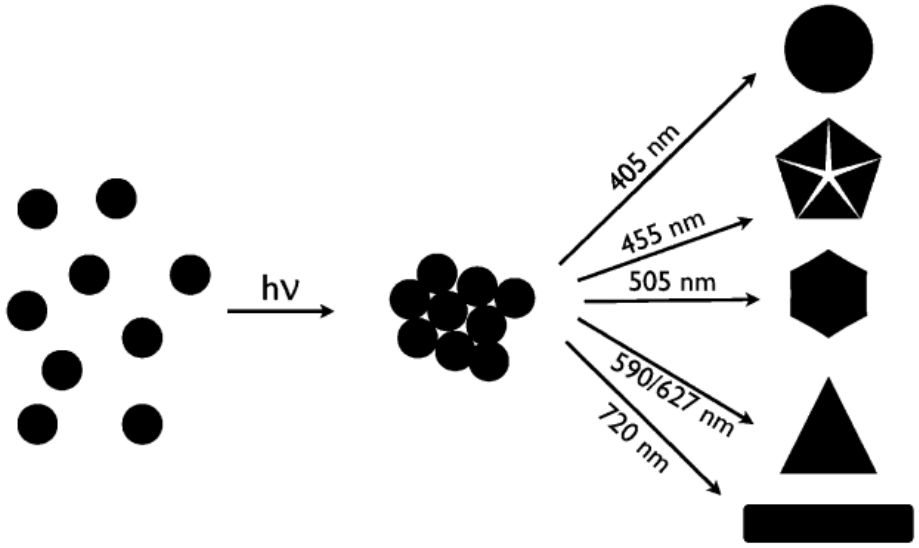

Figure 1.4: Photochemical nanostructure control of citrate-stabilized Ag nanoparticles.

1.4.3 Noble Metal Photodeposition on Semiconductor Supports

Photodeposition is a conceptually easy route for directly depositing metal nanoparticles on a photosensitive support. During photodeposition, light illumination is used to induce the reduction of a metal salt to metal nanocrystals that nucleate and grow directly on a photosensitive support. Upon irradiation with photons possessing energy higher than the semiconductor bandgap, electron-hole pairs are generated. Subsequently, the metal ions adsorbed on the semiconductor surface are reduced by the photogenerated electrons from the semiconductor, forming a metal (in some cases zero-valent) nanoparticle nucleus upon which nanoparticle growth continues, with continued reduction [75, 79]. This leads to the formation of crystallites as illustrated in Figure 1.5. The mean size of nanoparticles depends on the nature of the metal, semi-conducting substrate and experimental conditions [75].

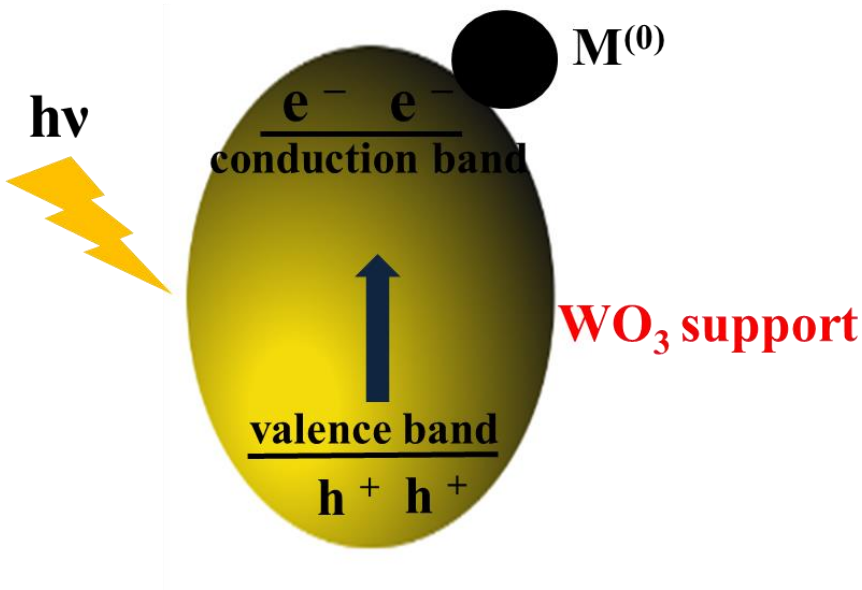

Figure 1.5: Photo-deposition process on a WO_3 support. Noble metal nanoparticles nucleate and grow upon reduction by photogenerated electrons.

Research efforts typically target reducible supports as the reducibility typically shows a good correlation with the catalytic activity for some reactions [82]. Leclerq et al. studied the photodeposition of various noble metals on a TiO_2 substrate. They reported a uniform dispersion of metal crystallites on the TiO_2 support [75]. After irradiation with white light for 10 minutes, weight loadings of 1% and diameters of ~1 nm were observed for photodeposited Pt materials. Weight loadings of 2% and diameters of ~3-5 nm were reported for Ag materials photodeposited under similar conditions. Leclerq et al. also reported comparably fast deposition of Pd and Au on TiO_2 supports; however, Ir required as much as 11 h of light illumination to photodeposit only 1 wt. % of ~1 nm diameter Ir metal particles, while Cu and Ni failed to photodeposit [75]. The lack of Ni deposition was attributed to the misalignment of the flat band potentials of TiO_2 with the redox potential of the Ni^{2+}/Ni^0 couple [75].

In this thesis, we attempted to synthesize WO_3-supported Ag, Au, and Pt nanoparticles of varying shapes via the photodeposition synthesis method. Our goal was to simultaneously

control the size and shape. These photodeposited materials were evaluated for the selective hydrogenation of crotonaldehyde, and the results were correlated with key nanostructural properties of the noble metal particles. Results from the three noble metal systems are expected to assist in the design of chemoselective catalysts for other reactions.

1.5 Research Goals and Thesis Layout

The focus of research described in this dissertation was to demonstrate methods for the synthesis of materials with controlled nanostructural properties, evaluate the performance of these materials in industrially relevant applications, and determine, as necessary, the bases for their performance characteristics. In particular, we investigated hematite ($\propto$-Fe_2O_3) nanotube arrays for photoelectrochemical water oxidation, orthorhombic niobium pentoxide (T-Nb_2O_5) for Li^+ ion intercalation, and photodeposited noble metal (Ag, Au, Pt) nanoparticles for the selective hydrogenation of crotonaldehyde, a α,β-unsaturated aldehyde. The results could enable the development of general design rules and techniques for the synthesis of nanostructured materials with superior performance. In the context of PECs, the objectives are to:

- Prepare hematite nanotubes and understand the formation mechanisms.
- Use the derived information to fabricate novel nanotube arrays; these include multilayers and wavelike nanotube-based photoanodes.
- The results will be used to develop structure-property (water photo-oxidation) relationships for the materials.

In the context of electrochemical energy storage, the objectives are to:

- Synthesize planar and nanotube-based T-Nb_2O_5 electrodes.
- Evaluate the Li^+ intercalation behavior in T-Nb_2O_5 via charge/discharge experiments.

- Correlate electrode morphology to key electrochemical performance metrics and intercalation behavior.

In the context of catalytic materials, the objectives are to:

- Synthesize WO_3-supported Ag, Au, and Pt nanostructures through the photodeposition technique.
- Evaluate the catalytic behavior (chemoselectivity and activity) of WO_3-supported Ag, Au, and Pt nanostructures for crotonaldehyde hydrogenation.
- Correlate the activity and chemoselectivity results with key nanostructural properties of the noble metal particles.

This thesis is divided into six chapters: the current chapter provided an introduction to various nanostructured systems for PEC water splitting, Li ion storage, and catalytic hydrogenation of crotonaldehyde. Chapters Two to Six are briefly summarized below.

Chapter 2: Design and Synthesis of Hematite Nanotube Arrays

The synthesis methods used to fabricate the hematite nanotube arrays (single layer, multilayer, and wavelike) are described. The formation mechanisms are explored. In addition, other common nanotube synthesis techniques are discussed and compared and contrasted with the electrochemical anodization technique used in this work. Bulk and surface properties of the various nanotube morphologies are characterized using X-ray Diffraction and Scanning Electron Microscopy.

Chapter 3: Characterization of Hematite Nanotube Arrays for Photocatalysis

The performance of photoelectrodes with different morphologies are evaluated and discussed. Electrochemical characterization methods utilized in this work include linear sweep voltammetry and cyclic voltammetry. Photoanode efficiencies for arrays with different morphologies are evaluated and correlated with nanotube physical structure and properties.

Chapter 4: Li^+ Intercalation Behavior of Nanostructured T-Nb_2O_5 for Electrochemical Energy Storage: A Comparative Study of Planar and Nanotubular Electrodes

The synthesis of planar and nanotubular T-Nb_2O_5 electrodes is described. Furthermore, the electrochemical performance evaluation and the Li^+ intercalation behaviors of the electrodes are discussed. The electrochemical characterization methods included charge/discharge experiments, cyclic voltammetry, and electrochemical impedance spectroscopy. Bulk and surface properties of the two electrode nanostructures are characterized using X-ray Diffraction and Scanning Electron Microscopy techniques and correlated with key electrochemical performance measurements.

Chapter 5: Nanostructured Au, Ag, and Pt Metals Photodeposited on WO_3 for Crotonaldehyde Hydrogenation

The synthesis (through photodeposition) and characterization of nanostructured Ag, Au, and Pt materials supported on WO_3 are discussed. The activities and chemoselectivities for crotonaldehyde hydrogenation were evaluated, and correlated with the nanostructure of the materials.

Chapter 6: Conclusions and Future Work

A summary of key research findings and conclusions for the three materials systems investigated in this thesis are presented. Recommendations for addressing limitations identified in this work

and extending it towards the development of enhanced materials systems for future devices for catalysis and electrochemical energy storage are also discussed.

1.6 References

[1] International Energy Agency Key World Energy Statistics, **2015**.
[2] U.S. Department of Energy. Basic Research Needs for Electrical Energy Storage, **2007**, <www.sc.doe.gov/bes/reports/abstracts.html#EES2007>.
[3] Intergovernmental Panel on Climate Change (IPCC). **2007**. Fourth Assessment Report <http://www.ipcc.ch/publications_and_data/publications_and_data_reports.shtml>.
[4] McGlade, C.; Ekins, P. The Geographical Distribution of Fossil Fuels Unused When Limiting Global Warming to 2 °C, *Nature* **2015**, *517*, 187.
[5] World Resources Institute, Keys to Achieving Universal Energy Access Series <http://www.wri.org/publication-series/keys-achieving-universal-energy-access>.
[6] Energy Independence and Security Act, United States House of Representatives, **2007,** <http://www.gpo.gov/fdsys/pkg/BILLS-110hr6enr/pdf/BILLS-110hr6enr.pdf>.
[7] Sorensen, B. Renewable Energy Conversion, Transmission, and Storage, Academic Press, **2007**, ISBN: 978-0-12-374622-9.
[8] Sun, J.; Zhong, D. K.; Gamelin, D. R. Composite Photoanodes for Photoelectrochemical Solar Water Splitting. *Energy Environ. Sci.* **2010**, *3*, 1252.
[9] International Electrotechnical Commission. Nanotechnology in the Sectors of Solar Energy and Energy Storage: Technology Report, **2014**.
[10] Zaera F. Nanostructured Materials for Applications in Heterogeneous Catalysis. *Chem. Soc. Rev.* **2013**, *42*, 2746.
[11] Arico, A. S.; Bruce, P.; Scrosati, B.; Tarascon, J.-M.; van Schalkwijk, W. Nanostructured Materials for Advanced Energy Conversion and Storage Devices, *Nat. Mat.* **2005**, *4*, 366.
[12] Nazar, L. F.; Goward, G.; Leroux, F.; Duncan, M.; Huang, H.; Kerr, T.; Gaubicher, J. Nanostructured Materials for Energy Storage, *Int. J. Inorg. Mater*. **2001**, *3*, 191.
[13] Xu, R.; Wang, D.; Zhang, J.; Li, Y. Shape-Dependent Catalytic Activity of Silver Nanoparticles for the Oxidation of Styrene, *Chem. Asian J*. **2006**, *1*, 888.
[14] Lin, Y.; Zhou, S.; Sheehan, S. W.; Wang, D. Nanonet-based Hematite Heteronanostructures for Efficient Water Splitting. *J. Am. Chem. Soc*. **2011**, *133*, 2398.
[15] Zhao, Y.; Peng, L.; Liu, B.; Yu, G. Single-Crystalline $LiFePO_4$ Nanosheets for High-Rate Li-Ion Batteries. *Nano Lett.* **2014**, *14*, 2849.
[16] Gratzel, M. Photoelectrochemical Cells. *Nature* **2001**, *414*, 338.
[17] Fujishima, A.; Honda, K. Electrochemical Photolysis of Water at a Semiconductor Electrode. *Nature* **1972**, *238*, 37.
[18] Ramachandran, R.; Menon, R. K. An Overview of Industrial Uses of Hydrogen. *Int. J. Hydrogen Energ.* **1998**, *23*, 593.
[19] Kanan, M. W.; Surendranath, Y.; Nocera, D. G. Cobalt-Phosphate Oxygen-Evolving Compound. *Chem. Soc. Rev.* **2009**, *38*, 109.
[20] Wheeler, D. A.; Wang, G.; Ling, Y.; Li, Y.; Zhang, J. Z. Nanostructured Hematite: Synthesis, Characterization, Charge Carrier Dynamics, and Photoelectrochemical Properties. *Energy Environ. Sci.* **2012**, *5*, 6682.
[21] Tsuchiya, H.; Hueppe, M.; Djenizian, T.; Schmuki, P.; Fujimoto, S. Morphological Characterization of Porous InP Superlattices. *Sci. Technol. Adv. Mat.* **2004**, *5*, 119.
[22] Licht, S.; Bard A. J.; Stratmann, M. Solar Photoelectrochemical Generation of Hydrogen Fuel: *Encyclopedia of Electrochemistry, Wiley-VCH, Weinheim, Germany* **2002**, 346.
[23] Chandra, S. Photoelectrochemical Solar Cells, *Electrocomponent Science*

Monographs, Gordon and Breach Science Publisher **1985**, Ed. 5.
[24] Morisaki, H.; Watanabe, T.; Iwase, M.; Yawaza, K. Photoelectrolysis of Water With TiO_2-covered Solar-cell Electrodes. *Appl. Phys. Lett.* **1976**, *29*, 338.
[25] Bak, T.; Nowotny, J.; Rekas, M.; Sorrel, C. C. Photoelectrochemical Hydrogen Generation from Water Using Solar Energy. Materials Related Aspects. *Int. J.Hydrogen Energ.* **2002**, *27*, 991.
[26] Carvalho, V. A. N.; Luz, R. A.; Lima, B. H.; Crespilho, F. N.; Leite, E. R.; Souza, F. L. Highly Oriented Hematite Nanorods Arrays for Photoelectrochemical Water Splitting. *J. Power Sources* **2012**, *205*, 525.
[27] Beermann, N.; Vayssieres, L.; Lindquist, S.-E.; Hagfeldt, A. Photoelectrochemical Studies of Oriented Nanorod Thin Films of Hematite. *J. Electrochem. Soc.* **2000**, *147*, 2456.
[28] Ahmadi, M.; Guinel, M. J.-F. Synthesis and Characterization of Tungstite ($WO_3 \cdot H_2O$) Nanoleaves and Nanoribbons. *Acta Mater.* **2014**, *69*, 203.
[29] Sivula, K.; Le Formal, F.; Gratzel, M. Solar Water Splitting: Progress Using Hematite Photoelectrodes. *ChemSusChem.* **2011**, *4*, 432.
[30] Rangaraju, R. R.; Panday, A.; Raja, K. S.; Misra, M. Nanostructured Anodic Iron Oxide Film as Photoanode for Water Oxidation. *J. Phys. D: Appl. Phys.* **2009**, *42*, 135303.
[31] Wang, H.; Turner, J. A. Characterization of Hematite Thin Films for Photoelectrochemical Water Splitting in a Dual Photoelectrode Device. *J. Electrochem. Soc.* **2010**, *157*, F173.
[32] Maheshwar, S.; Bard, A. J.; Stratmann, M. Encyclopedia of Electrochemistry, Semiconductor Electrodes and Photoelectrochemistry, *Wiley-VCH, Weinheim, Germany* **2002** Ed. 6.
[33] Nakamura, R.; Tanaka, T.; Nakato, Y. Mechanism for Visible Light Responses in Anodic Photocurrents at N-doped TiO_2 Film Electrodes. *J. Phys. Chem. B.* **2004**, *108*, 10617.
[34] Irie, H.; Watanabe, Y.; Hashimoto, K. Nitrogen-Concentration Dependence on Photocatalytic Activity of $TiO_{2-x}N_x$ Powders. *Journal of Physcal Chemistry B.* **2003**, *107*, 5483.
[35] Nakano, Y.; Morikawa, T.; Ohwaki, T.; Yasunori, T. Deep-Level Characterization of N-Doped Films Prepared by Reactive Magnetron Sputtering. *Appl. Phys. Lett.* **2005**, *87*, 232104.
[36] Latempa, T. J.; Feng, X.; Paulose, M.; Grimes, C.A. Temperature-Dependent Growth of Self-Assembled Hematite Nanotube Arrays: Rapid Electrochemical Synthesis and Photoelectrochemical Properties. *J. Phys. Chem. C*. **2009**, *36*, 16293.
[37] Pendlebury, S. R.; Wang, X.; Le Formal, F.; Cornuz, M.; Kafizas, A.; Tilley, S. D.; Gratzel, M.; Durrant, J. R.; Ultrafast Charge Carrier Recombination and Trapping in Hematite in Hematite Photoanodes under Applied Bias, *J.Am.Chem.Soc,* **2014**, *136*, 9854.
[38] Ghicov, A.; Patrik Schmuki, P. Self-ordering Electrochemistry: A Review on Growth and Functionality of TiO_2 Nanotubes and Other Self-aligned MO_x Structures. *Chem. Commun.* **2009**, 2791.
[39] Vayssieres, L.; Beermann, N.; Lindquist, S. E.; Hagfeldt, A. Controlled Aqueous Chemical Growth of Oriented Three-dimensional Crystalline Nanorod Arrays: Application to Iron(III)-Oxides. *Chem. Mater.* **2001**, *13*, 233.
[40] Yu, Y. W.; Zhu, X. J.; Xu, K. S.; Yeong, Z. X.; Shen, P.; Chen, C. T.; Lim, J. T. L.; Thong, C. H. Substrate-Friendly Synthesis of Metal Oxide Nanostructures Using a Hotplate. *Small* **2006**, *2*, 80.
[41] Han, Q.; Xu, Y. Y.; Fu, Y. Y.; Zhang, H.; Wang, R. M.; Wang, T. M.; Chen, Z. Y. Towards Large-scale Plasma-assisted Synthesis of Nanowires. *Chem. Phys. Lett.* **2006**, *431*, 100.
[42] Jun, H.; Im, B.; Kim, J. Y.; Im, Y.-O.; Jang, J.-W.; Kim, E. S.; Kim, J. Y.; Kang, H. J.; Hong, S. J.; Lee, J. S. Photoelectrochemical Water Splitting over Ordered Honeycomb Hematite Electrodes Stabilized by Alumina Shielding. *Energy Environ. Sci.* **2012**, *5*, 6375.

[43] Aurora, P. Photoelectrochemical Systems for Hydrogen Production, PhD Thesis – University of Michigan, **2010**.
[44] Wang, L.; Zhou, X.; Nguyen, N. T.; Schmuki, P. Plasmon-Enhanced Photoelectrochemical Water Splitting Using Au Nanoparticles Decorated on Hematite Nanoflake Arrays. *ChemSusChem*. **2015**, *8*, 618.
[45] Ozkar, S. Enhancement of Catalytic Activity by Increasing Surface Area in Heterogeneous Catalysis. *Appl. Surf. Sci*. **2009**, *256*, 1272.
[46] Yoo, H. D.; Markevich, E.; Salitra, G.; Sharon, D. On the Challenge of Developing Advanced Technologies for Electrochemical Energy Storage and Conversion, *Mater. Today* **2014**, *17*, 110.
[47] Zaghib, K.; Dontigny, M.; Guerfi, A.; Charest, P.; Rodrigues, I.; Mauger, A.; Julien, C. M. Safe and Fast-Charging Li-ion Battery with Long Shelf Life for Power Applications *J. Power Sources* **2011**, *196*, 3949.
[48] Goodenough, J. B.; Park, K. S. The Li-Ion Rechargeable Battery: A Perspective *J. Am. Chem. Soc.* **2013**, *135*, 1167.
[49] Ding, N.; Xu, J.; Yao, Y. X.; Wegner, G.; Fang, X.; Chen, C.H.; Lieberwirth, I. Determination of the Diffusion Coefficient of Lithium Ions in Nano-Si, *Solid State Ionics* **2009**, *180*, 222.
[50] Simon, P.; Gogotsi, Y.; Dunn, B. Where Do Batteries End and Supercapacitors Begin? *Science* **2014**, *343*, 6176.
[51] Conway, B. E. Electrochemical Supercapacitors: Scientific Fundamentals and Technological Applications, *Kluwer* **1999**.
[52] Simon, P.; Gogotsi, Y. Materials for Electrochemical Capacitors. *Nat. Mater.*, **2008**, *7*, 845.
[53] Guo, Y.-G.; Hu, J.-S. Wan, L.-J. Nanostructured Materials for Electrochemical Devices. *Adv. Mater*. **2008**, *20*, 2878.
[54] Amatucci, G. G.; Badway, F.; Pasquier, A. D.; Zheng, T. An Asymmetric Hybrid Nonaqueous Energy Storage Cell. *J. Electrochem. Soc*. **2001**, *148*, A930.
[55] Chan, C. K.; Peng, H.; Liu, G.; Mcilwrath, K.; Zhang, X. F.; Huggins, R. A.; Cui, Y. High-Performance Lithium Battery Anodes Using Silicon Nanowires. *Nat. Nanotech*. **2008**, *3*, 31.
[56] Yamada, A.; Hosoya, M.; Chung, S. C.; Kudo, Y.; Hinokuma, K.; Liu, K. Y.; Nishi, Y. Olivine-Type Cathodes: Achievements and Problems. *J. Power Sources* **2003**, *232*, 119.
[57] Fu, L. J.; Liu, H.; Li, C.; Wu, Y. P.; Rahm, E.; Holze, R; Wu, H. Q. Surface Modifications of Electrode Materials for Lithium Ion Batteries. *Solid State Sci.* **2006**, *8*, 113.
[58] Wang, J.; Sun, X. Olivine $LiFePO_4$: the Remaining Challenges for Future Energy Storage. *Energy Environ. Sci.* **2015**, *8*, 1110.
[59] Li, X.; Gu, M.; Hu, S.; Kennard, R.; Yan, P.; Chen, X.; Wang, C.; Sailor, M. J.; Zhang, J.; Liu, J. Mesoporous Silicon Sponge as an Anti-pulverization Structure for High-performance Lithium-ion Battery Anodes, *Nature Communications*. **2014**, *5*, 4105.
[60] Liang, B.; Liu, Y.; Xu, Y. Silicon-based Materials as High Capacity Anodes for Next Generation Lithium Ion Batteries. *J. Power Sources* **2014**, *267*, 469.
[61] Augustyn, V.; Come, J.; Lowe, M. A.; Kim, J. W.; Taberna, P.-L.; Tolbert, S. H.; Abruña, H. D.; Simon, P.; Dunn, B. High-Rate Electrochemical Energy Storage through Li^+ Intercalation Pseudocapacitance. *Nat. Mater.* **2013**, *12*, 518.
[62] Kim, J. W., Augustyn, V.; Dunn, B. The Effect of Crystallinity on the Rapid Pseudocapacitive Response of Nb_2O_5. *Adv. Energy Mater.* **2012**, *2*, 141.
[63] Cava, R. J.; Batlogg, B.; Krajewski, J. J.; Poulsen, H. F.; Gammel, P.; Peck, W. F.; Rupp, L. W. Electrical and Magnetic Properties of Nb_2O_{5-d} Crystallographic Shear Structures. *Phys. Rev. B: Condens. Matter Mate*r. *Phys*. **1991**, *44*, 6973.

[64] Mushove, T.; Breault, T. M.; Thompson, L. T. Synthesis and Characterization of Hematite Nanotube Arrays for Photocatalysis. *Ind. Eng. Chem. Res.* **2015**, *54*, 4285.
[65] Claus, P.; Hofmeister, H. Electron Microscopy and Catalytic Study of Silver Catalysts: Structure Sensitivity of the Hydrogenation of Crotonaldehyde. *J. Phys. Chem. B.* **1999**, *103*, 2766.
[66] Niu, W.; Xu, G. Crystallographic Control of Noble Metal Nanocrystals, *Nano Today* **2011**, *6*, 265.
[67] Pradier, C. M.; Birchem, T.; Berthier, Y.; Cordier, G. Hydrogenation of 3-methyl-butenal on Pt(110); Comparison With Pt(111), *Catal. Lett*. **1994**, *29*, 371.
[68] Englisch, M.; Jentys, A.; Lercher, J. A. Structure Sensitivity of the Hydrogenation of Crotonaldehyde over Pt/SiO_2 and Pt/TiO_2, *J. Catal*. **1997**, *166*, 25.
[69] Birchem, T.; Pradier, C. M.; Berthier, Y.; Cordier, G. Reactivity of 3-Methyl-Crotonaldehyde on Pt(111). *J. Catal.* **1994**, *146*, 503.
[70] Zanella, R.; Louis, C.; Giorgio, S.; Touroude, R. Crotonaldehyde Hydrogenation by Gold Supported on TiO_2: Structure Sensitivity and Mechanism, *J. Catal*. **2004**, *223*, 328.
[71] Firestone, M.A.; Dietz, M. L.; Seifert, S.; Trasobares, S.; Miller, D. J.; Zaluzec, N. J. Ionogel-Templated Synthesis and Organization of Anisotropic Gold Nanoparticles. *Small* **2005**, *1*, 754.
[72] Tao, A. R.; Habas, S.; Yang, P. Shape Control of Colloidal Metal Nanocrystals. *Small* **2008**, *4*, 310.
[73] Lee, H.; Kim, C.; Yang, S.; Han, J. W.; Kim, J.; Shape-Controlled Nanocrystals for Catalytic Applications. *Catal. Surv. Asia* **2011**, DOI: 10.1007/s10563-011-9130-z.
[74] McKone, J. R.; Pieterick, A. P.; Gray, H. B.; Lewis, N. S.; Hydrogen Evolution from Pt/Ru-Coated p-Type WSe_2 Photocathodes. *J. Am. Chem. Soc.* **2013**, *135*, 223.
[75] Herrmann, J.; Disdier, J.; Pichati, P.; Leclerq, C. Photo-assisted Deposition of Noble Metals: Investigation of a New Route for Metallic and Bi-metallic Catalyst Preparation. *Stud. Surf. Sci. Catal.* **1987**, *31*, 285.
[76] Liu, J.; Chen, F. Plasmon Enhanced Photoelectrochemical Activity of Ag-Cu Nanoparticles on TiO_2/Ti Substrates, *Int. J. Electrochem. Sci.* **2012**, *7*, 9560.
[77] McDonald, K. J.; Choi, K-S. Photodeposition of Co-Based Oxygen Evolution Catalysts on Fe_2O_3 Photoanodes. *Chem. Mater*. **2011**, *23*, 1686.
[78] Wicaksana, Y.; Liu, S.; Scott, J.; Amal, R. Tungsten Trioxide as a Visible Light Photocatalyst for Volatile Carbon Removal. *Molecules* **2014**, *19*, 17747.
[79] Yoneyama, H.; Nishimura, N.; Tamura, H. Photodeposition of Palladium and Platinum onto Titanium Dioxide Single Crystals, *J. Phys. Chem.* **1981**, *85*, 268.
[80] Jin, R. C.; Cao, Y. W.; Mirkin, C. A.; Kelly, K. L.; Schatz, G. C.; Zheng, J. G. Photoinduced Conversion of Silver Nanospheres to Nanoprisms, *Science* **2001**, *294*, 1901.
[81] Stamplecoskie, K. G.; Scaiano, J. C. Light Emitting Diode Irradiation Can Control the Morphology and Optical Properties of Silver Nanoparticles, *J. Am. Soc.* **2010**, *1325*, 1825.
[82] Noronha, F. B.; Fendley, E. C.; Soares, R. R.; Alvarez, W. E.; Resasco, D. E. Correlation Between Catalytic Activity and Support Reducibility in the CO_2 Reforming of Methane over $Pt/Ce_xZr_{1-x}O_2$ Catalysts. *Chem. Eng. J.* **2001**, *82*, 21.

Chapter 2

Design and Synthesis of Hematite Nanotube Arrays

Portions of work summarized in this chapter were published in Mushove, T.; Breault, T.; Thompson, L. T. *Ind. Eng. Chem. Res.* **2015**, *54*, 4285.

2.1 Introduction

Chapter One introduced nanostructuring as one promising strategy to enhance the performance of catalytic and electrochemical energy storage materials. In nanostructured photocatalytic materials, improvements in efficiency are a result of reductions in charge carrier diffusion distances to the electrode-electrolyte interface, where catalytic reactions occur [1-2], thereby reducing recombination rates. In addition, nanostructured materials possess larger electrochemical surface areas, which increases the number of active sites for photocatalytic reactions [3]. Among materials that have been investigated for use as photoelectrodes for water oxidation, hematite holds promise because it is inexpensive, is photocorrosion resistant in alkaline electrolytes, and exhibits a relatively low bandgap (~2.1 eV), which allows it to absorb a large fraction of the solar spectrum [1-3]. The various hematite electrode nanostructures that have been explored in the literature for solar water photo-oxidation are illustrated in Figure 2.1. Planar electrodes have long diffusion lengths and therefore high recombination rates [2, 4]. Nanoparticle-based electrodes suffer from recombination losses at the interfaces between adjacent nanoparticles, in addition to poor electron transport to the back contact, which again

increases recombination rates [5]. Nanostructures such as nanorods and nanotubes are advantageous because they confine electron transport to one dimension and have large surface areas available for electrolyte contact, thus reducing recombination and increasing photoconversion efficiency [3]. Because nanotubes utilize their inner and outer wall surfaces towards photocatalytic reactions, this dissertation focuses on nanotube-based electrodes. A number of nanotube fabrication techniques have been explored in the literature. The next section provides a brief overview of the most common techniques.

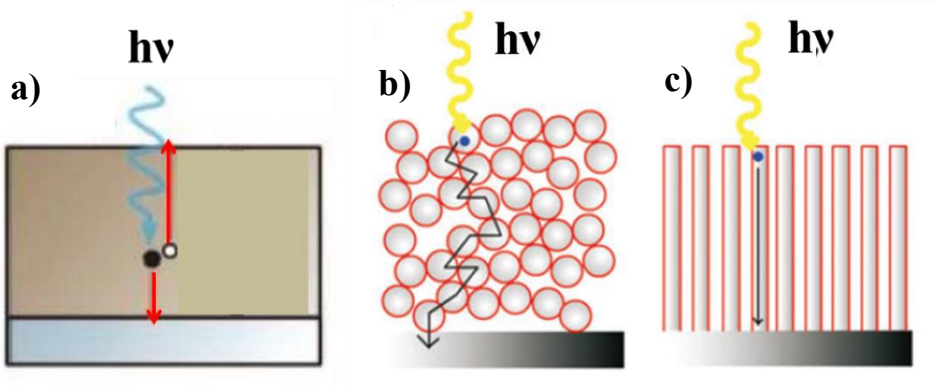

Figure 2.1: Examples of hematite nanostructures applied to photocatalysis: (a) planar film [4], (b) nanoparticle film, and (c) nanotube/nanorod film. Planar and nanoparticle electrodes result in substantial recombination. Nanotube/nanorod electrodes result in improved charge transport [5].

2.2 Hematite Nanotube Synthesis Techniques

Various synthesis techniques for fabricating iron oxide nanotubes have been investigated, including solution-based, vapor phase deposition based, and electrochemical methods. Yan et al. synthesized spindle-like, single-crystalline hematite nanotubes via the hydrothermal treatment of an $FeCl_3$ solution in the presence of small amounts of ammonium phosphate [6]. The nanotubes were roughly vertically oriented, but were sparsely dispersed on the substrate. Park et al. employed the electrochemical deposition method to synthesize vertically aligned hematite nanotubes [7]. First, polyaniline nanorods were electrodeposited into the pores of aluminum

oxide templates through potentiostatic cycling. Next, the samples were dried at 80 °C to reduce the size of the nanorods, which creates spaces between the nanorods and the aluminum oxide template. Iron was then electrodeposited into the empty gaps, after which a thermal treatment was used to simultaneously decompose the polyaniline nanorods and oxidize the iron into hematite. Hematite nanotubes were obtained after the removal of the aluminum oxide template by immersing the samples in 1 M sodium hydroxide solution. While this method could be used to achieve high quality, vertically oriented nanotubes with well-controlled dimensions, the relatively high fabrication cost is a major drawback.

Electrochemical anodization is a robust, inexpensive technique to synthesize metal oxide nanostructures. The experimental setup is simple, and the synthesis method is economical. The method also allows for a high level of morphological control through changes in synthesis conditions. The method has been known for over a hundred years, but it was not until the 1990s that it was discovered that ordered oxide nanostructures of various valve metals could be synthesized under controlled experimental conditions [8]. Prakasam et al. demonstrated the feasibility of nanostructuring iron foils through electrochemical anodization in a glycerol-based electrolyte containing ammonium fluoride, hydrogen fluoride, and nitric acid [9]. Initially, the technique was used to form nanopores, and soon after, it was discovered that hematite nanotubes could also be generated by varying the anodization conditions. Recently, electrochemical anodization has been studied more extensively as a synthesis technique for hematite nanostructures with tailored morphologies [10-12].

While the literature widely explores the application of hematite nanotube arrays for solar water photo-oxidation, to date there has been no investigation to understand the effect of variations in nanotube structure on photocatalytic performance. This chapter describes the

synthesis of hematite nanotube arrays of various morphologies using the electrochemical anodization technique, including two novel morphologies, multilayer and wave-like. The multilayer nanotube arrays were hypothesized to improve the photocatalytic performance as a consequence of enhanced light absorption due to scattering effects at the layer interfaces [5]. The wave-like nanotubes were expected to possess increased electrochemical surface areas compared to straight nanotubes, therefore enhancing photocatalytic rates [13]. By tracking the current and film resistances, the key stages during the synthesis of the nanotube arrays were identified. The bulk and surface structure of the materials were also characterized. The evaluation of the photocatalytic performance of the nanotube arrays for water oxidation is explored in the next chapter.

2.3 Experimental Method

2.3.1 Materials

Iron foil substrates (99.5% and 99.99%, 0.25 mm thick) were purchased from Alfa Aesar. Chemicals for production of the electrolytes, ammonium fluoride (98.5%), ethylene glycol (laboratory grade, < 0.2 wt% water), and potassium hydroxide (ACS grade, 88%) were purchased from Fisher Chemical. Ultrapure water (resistance 18.2 MΩ) was obtained from a Millipore Milli-Q water purification system.

2.3.2 Nanotube Array Synthesis

The nanotube arrays were synthesized via electrochemical anodization. A two-electrode cell was constructed using an iron foil substrate (0.25 mm, 1.70 cm^2) as the anode and a platinum foil (2.50 cm^2) as the cathode (Figure 2.2). The electrodes were set 2 cm apart and an Agilent 3647 power supply was used to apply a voltage across the electrochemical cell. To synthesize the nanotube arrays, an electrolytic solution composed of 2 wt% deionized water, 0.37 wt%

ammonium fluoride, and 97.63 wt% ethylene glycol was used. A customized MATLAB software routine was used to control the power supply, apply the voltage across the cell, and record the corresponding current response during the anodization experiment. Experimental data was collected at 0.5 s time intervals. Measured voltage profiles matched the input voltage profiles, indicating that the voltage drop across the internal resistances of the cell and power supply were negligible. In this dissertation, we present only the measured voltages.

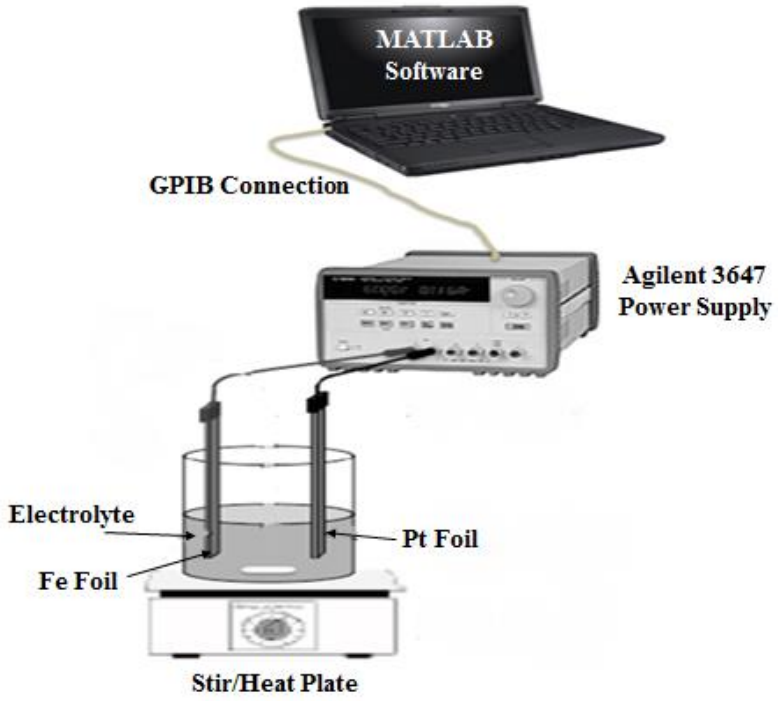

Figure 2.2: Schematic representation of electrochemical anodization cell used for nanotube array synthesis. A customized MATLAB software controls the power supply and records the current response.

Small fluctuations in the measured current, on the order of 0.01 mA, were observed during anodization. These fluctuations remained even when a simple resistor was connected across the power supply. The minimum resolution of the power supply at 25 ± 5 ºC was 0.014 mA, while the noise level was lower than 1.5 µA [14]. This indicated that the fluctuations were

an artifact of the power supply. In a typical anodization experiment, the measured currents were higher than 10 mA, and the effect of the current fluctuations on experimental results was therefore negligible. The measured values of the current were smoothed in order to avoid the fluctuation of the calculated differential resistance (dV/dI) between positive and negative values. Smoothing was performed using a moving average filter in MATLAB, over the span of five data points. The differential resistance was computed to help qualitatively understand the nanotube formation mechanism. The electrolyte temperature was maintained at 25 ± 2 ºC.

2.3.2.1 Single Layer Nanotube Synthesis

During the synthesis of single layer nanotube arrays, the voltage was increased from 0 to a holding voltage in the 30-60 V range at a rate of 25 mV/s. The holding voltage was maintained for between 10 and 30 minutes, depending on the desired nanotube length. For performance characterization (presented in Chapter Three), we used nanotube arrays that were ~3.0 μm in length. The synthesis condition we used to accomplish this for single layer nanotube arrays was a holding voltage of 40 V for 480 s. A typical voltage input and current response for single layer nanotube arrays (synthesized at a holding voltage of 40 V) is shown in Figure 2.3. After anodization, the nanotube samples were rinsed with ethanol to remove any remaining electrolyte from the surface of the film. Thereafter, the samples were sonicated in ethanol for 15 minutes to remove debris covering the openings of the nanotubes. The nanotube samples were then dried in a vacuum oven at 80 °C for 30 minutes. In addition to sonication, multilayer nanotubes (discussed in detail below) also required ultrasonication in order to expose the layers before characterization with SEM.

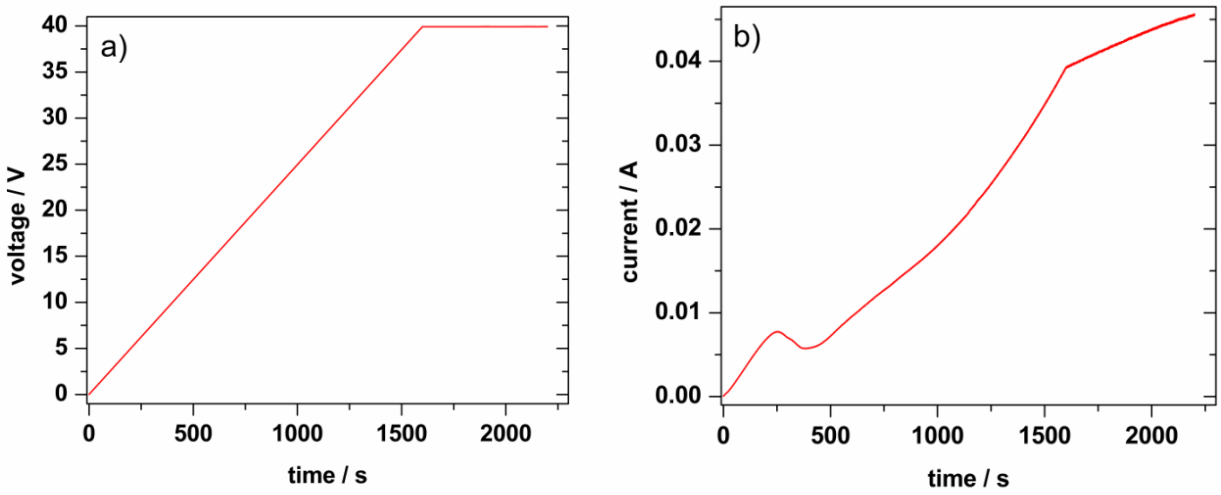

Figure 2.3: a) Measured voltage input and b) current response for single layer nanotube arrays synthesized at a holding voltage of 40 V.

2.3.2.2 Multilayer Nanotube Synthesis

Multilayer nanotube arrays were synthesized by increasing the voltage from 0 V to 45 V at a rate of 2.5 V/s and then pulsing the voltage between 45 V and 20 V. A pulse consisted of a hold at 45 V for a varying duration, from 40-140 s, followed by a hold at 20 V for 60 s. The number of layers (up to seven) could be varied by changing the number of pulse cycles. Beyond seven pulses, no further layer growth occurred due to poor diffusion of oxygen to the lower nanotube layers [15]. Multilayer nanotube arrays that were ~3.0 μm in length and composed of five layers were synthesized using a hold voltage of 45 V for 72 s, followed by a hold at 20 V for 60 s, for five pulses (total anodization time = 660 s). Figure 2.4a shows a typical input voltage used to synthesize multilayer nanotube arrays with five layers, and Figure 2.4b shows the corresponding current response.

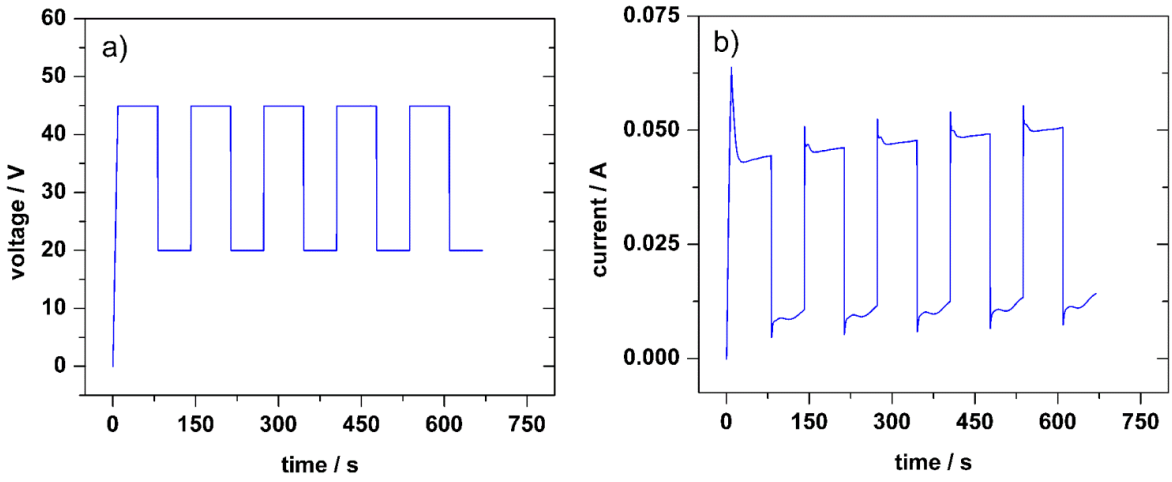

Figure 2.4: a) Measured voltage input, and b) current response for synthesis of multilayer nanotube arrays with five layers.

2.3.2.3 Wave-like Nanotube Synthesis

Wave-like nanotube arrays were synthesized by applying a triangular profile with voltages between 30 and 60 V, a period of 34 s, and a total time of 1260 s. Figures 2.5a and b show the voltage inputs and current responses, respectively. These synthesis conditions were designed to produce films with nanotube arrays that were ~3.0 µm in length. Attempts to synthesize wave-like nanotubes using a sinusoidal input potential were not successful, resulting in multilayer nanotube arrays instead.

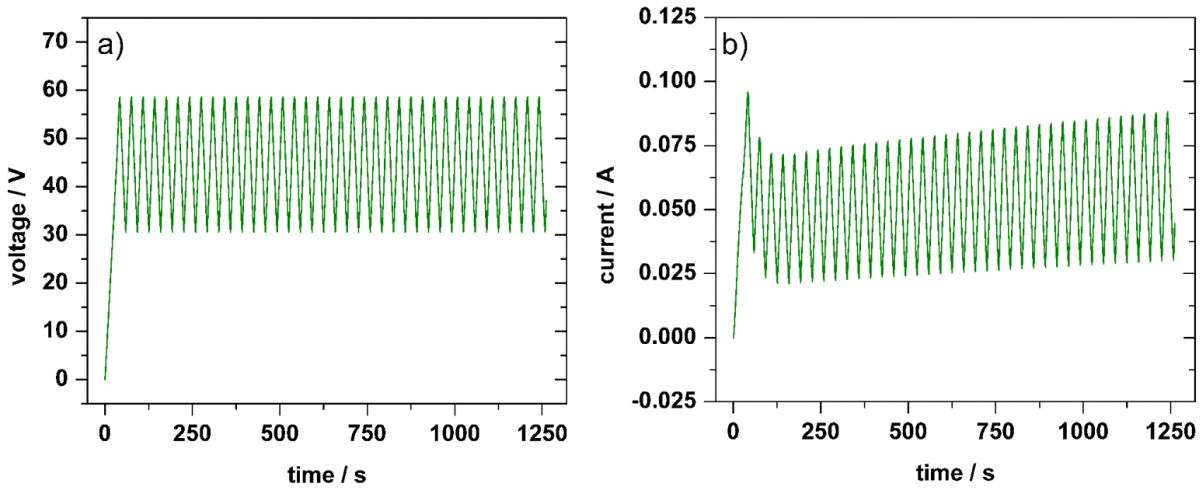

Figure 2.5: a) Measured voltage input and b) current response for synthesis of wave-like nanotube arrays.

2.3.3 Surface and Bulk Materials Characterization

Bulk and surface characterization of materials was done using X-ray diffraction (XRD) and scanning electron microscopy (SEM). XRD patterns of the materials before and after a thermal treatment step were recorded using a Rigaku 600 Miniflex X-ray diffractometer equipped with a graphite monochromator and Cu Kα radiation (λ = 1.5 Å). Patterns were collected at a step size and scan rate of 0.02°/step and 2.00°/minute, respectively. Phases were identified using MDI Jade version 10. The nanotube array surface and cross-sectional morphologies were imaged using a FEI Nova 200 Nanolab field emission SEM. Prior to SEM imaging, the nanotube films were coated with a thin film of Au/Pd using an Anatech Hummer VI sputter coater. The SEM micrographs were used to determine average diameters and lengths of the nanotubes.

2.4 Results and Discussion

2.4.1 Nanotube Array Synthesis and Formation Mechanism

Varying the conditions during electrochemical anodization enabled the synthesis of three different hematite nanotube morphologies: single layer, multilayer, and wave-like. The sequence of physical and chemical events occurring during nucleation and growth of the nanotube arrays was determined from the current response data during anodization. The literature suggests that nanotube array formation proceeds via two competing processes: the voltage-induced formation of an oxide layer and the chemical dissolution of the oxide in the presence of highly complexing fluoride ions [10, 12, 16].

2.4.1.1 Single Layer Nanotube Arrays

The current response, instantaneous resistance (V/I) (Figure 2.6a), and differential resistance (dV/dI) (Figure 2.6b) indicate four distinct stages during synthesis of the single layer nanotube arrays. During Stage I, the current response is Ohmic, a consequence of the iron foil behaving as a simple resistor when a voltage is applied across it. The accompanying differential resistance during Stage I remains fairly constant (Figure 2.6b), suggesting that there are no significant changes in the physical structure of the material. During Stage II, there was a sudden decrease in the current, resulting from a sharp increase in the resistance. This sharp increase was due to the formation of a thin oxide layer on the iron substrate [12]. A negative differential resistance (NDR) is typically observed for semiconductors [18] and is a result of quantum tunneling effects [19]. One possible way NDR arises is that the thin oxide film behaves as a shallow potential well [19], allowing electrons to tunnel through it at the high electric fields that is applied during anodization. UV-vis spectroscopy of the remnant solutions (Figure 2.7) from anodization experiments revealed that the materials exhibited optical properties consistent with

the presence of semiconducting iron oxides [10]. Results from X-ray diffraction experiments (discussed in Section 2.4.2), showed that the thin oxide layer was amorphous iron oxide. A red-brown coloration was simultaneously observed on the electrode during this stage; this suggested that the initial oxide layer was formed according to the following chemical reaction [10, 16]:

$$2Fe + 3H_2O \rightarrow Fe_2O_3 + 6H^+ + 6e^- \qquad (1)$$

The subsequent increase in current and reduction in instantaneous resistance observed during Stage III was likely due to the onset of pitting of the oxide layer by the fluoride ions, resulting in a reduction in the mass of the more resistive oxide. The chemical dissolution of the oxide could occur according to the following reaction, which results in the formation of highly soluble hexafluoroferrate complexes [10, 12]:

$$Fe_2O_3 + 12F^- + 6H^+ \rightarrow 2[FeF_6]^{3-} + 3H_2O \qquad (2)$$

Confirmation of the presence of hexafluoroferrate ions in solution was demonstrated previously by Tilley [20]. Tilley identified the absorbance peak at ~719 nm as hexafluoroferrate ions [20]. Using UV-vis spectroscopy, we were able to show a similar absorbance peak at ~719 nm for solutions after anodization (Figure 2.7), corroborating the reaction path shown in Equation (2) above.

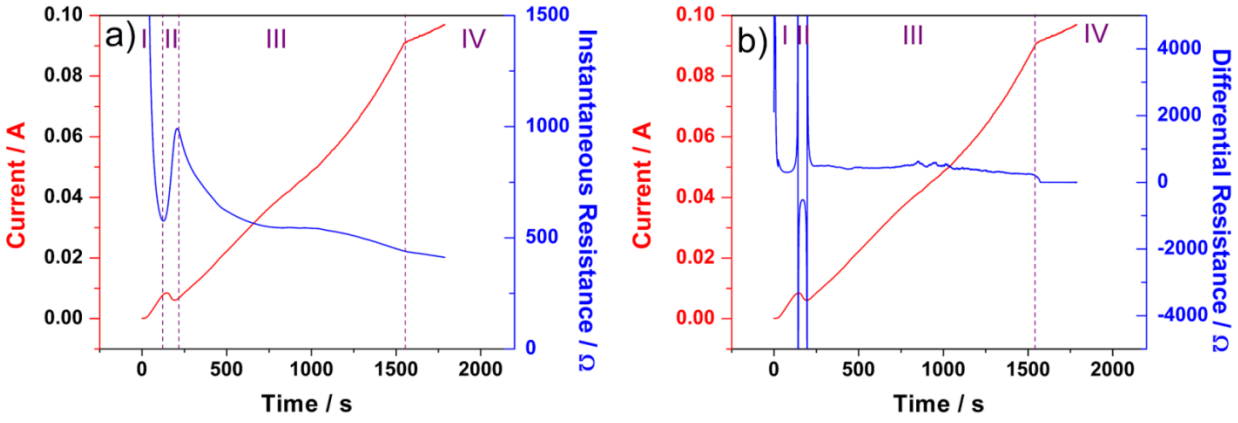

Figure 2.6: Typical current responses and a) computed instantaneous (V/I) and b) differential (dV/dI) resistances during single layer nanotube array synthesis at a holding voltage of 40 V.

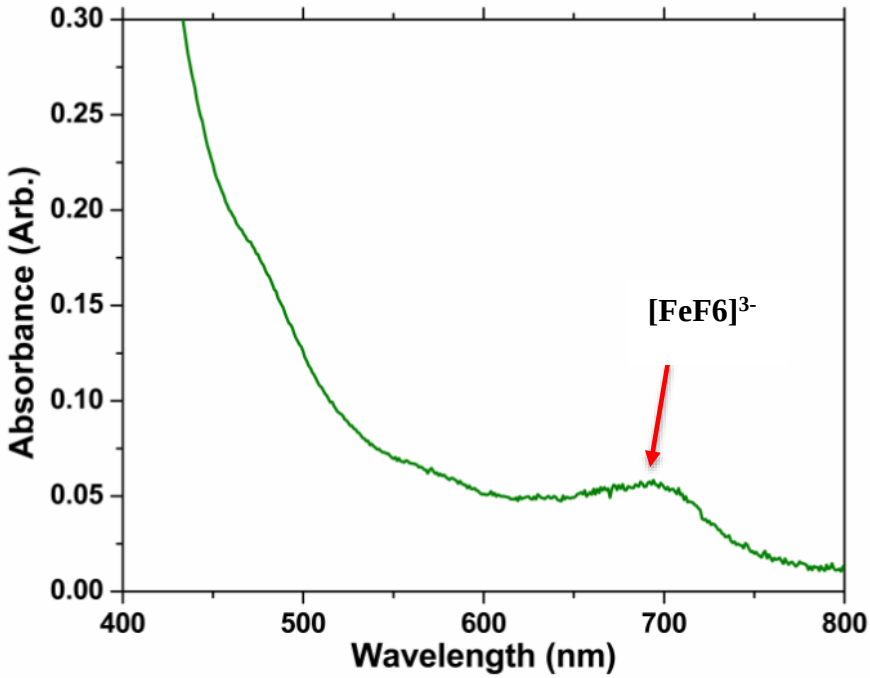

Figure 2.7: Absorbance spectrum of electrolyte after anodization. The chemical dissolution of iron oxide leads to the formation of hexafluoroferrate complexes.

The chemical action of the fluoride ions on the oxide is aided by the strong electric field [10], which likely polarizes and weakens the Fe-O bonds, making it easier for fluoride ions to complex the iron ions. This hypothesis is based on the findings of Maruyama et al., who

observed the polarization of Ti-O bonds in $BaTiO_3$ under the application of electric fields [21]. In our study, nanotube formation was only observed at holding voltages ≥ 30 V. Neophytic nanotube pores become visible under SEM at ~20 V, as shown in Figure 2.8. Surface defects on the compact oxide layer lead to localized variations in the current density, resulting in the initiation of pit formation in areas where the current is more concentrated. Increased local current density leads to local Joule heating and faster reaction rates, thus enhancing the dissolution process. Corrosion continues within the pit, with complementary reduction at the oxide surface, perpetuating pore growth at some points as opposed to others [22-24].

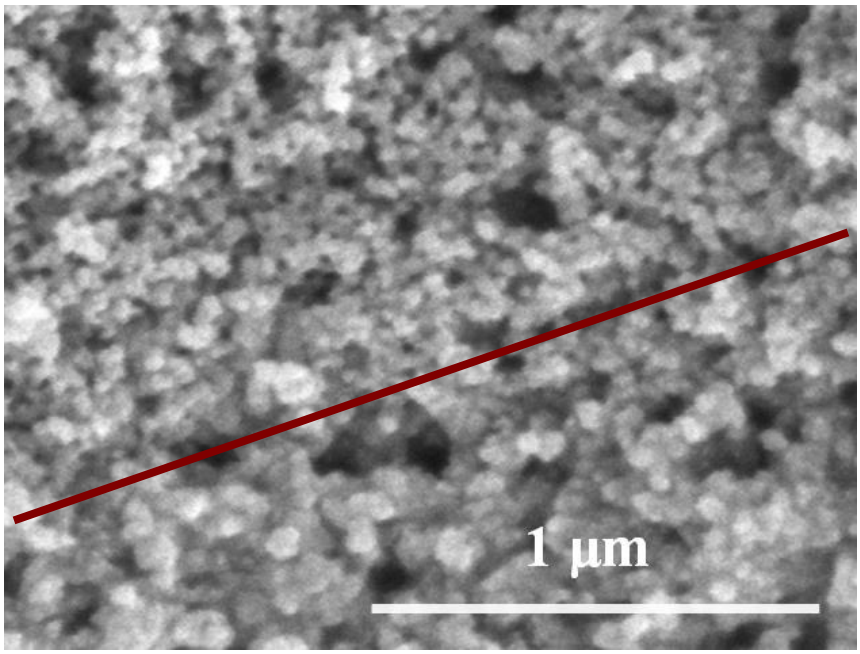

Figure 2.8: Initiation of nanotube formation at ~20 V. Above the line, there is evidence of nanotube formation; below it, the oxide layer is still compact.

During Stage IV, at constant applied potential, the nanotubes grow at a constant rate as evident in the constant current increase observed in Figure 2.3. Figure 2.9 shows the current response for the last 10 minutes (Stage IV) of the anodization process for different final applied

voltages. The rate of nanotube growth increases with increasing holding voltage. Higher holding potentials therefore shorten the amount of time required for complete nanotube formation. However, higher applied potentials also require longer ramping times, resulting in extensive nanotube dissolution. Extended anodization times at lower holding voltages ($\leq$ 40 V) also resulted in nanotube dissolution.

Also, as shown in Figure 2.9, for a final voltage of 20 V, the measured current remains almost constant, suggesting that there are only minimal changes in the resistance of the iron oxide film in Stage IV, and hence minimal pitting or changes in morphology at this voltage. This corroborates the SEM observation shown in Figure 2.8, that is, voltage-aided chemical dissolution occurs only at voltages higher than 20 V under the experimental conditions used in this work. This lower voltage limit was important for the synthesis of multilayer nanotube arrays, discussed below. Figure 2.10 shows a schematic summarizing the single layer nanotube array formation mechanism discussed.

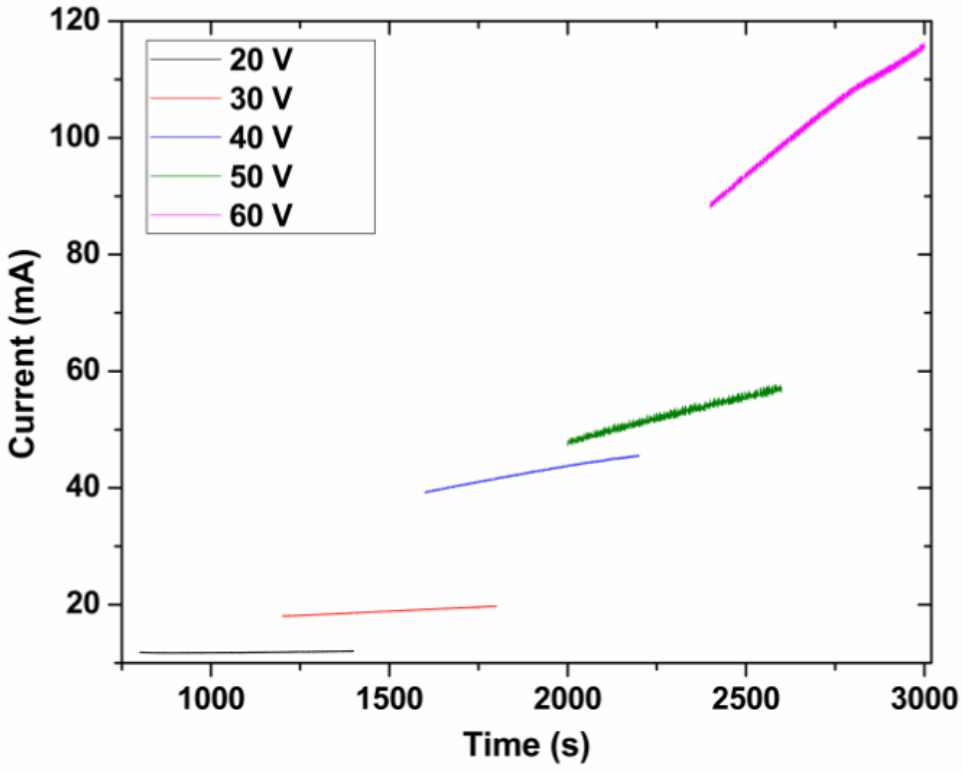

Figure 2.9: Current response for Stage IV of nanotube formation for different final applied potentials. Nanotube formation initiates at ~20 V and nanotube growth rate increases with holding voltage.

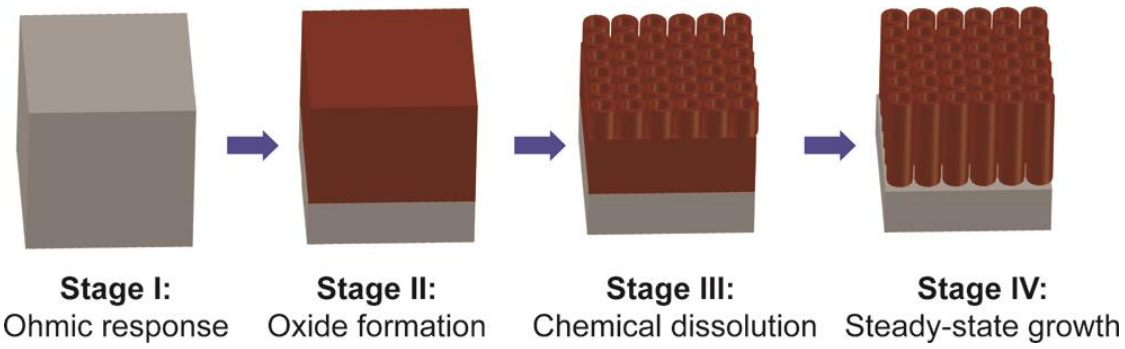

Figure 2.10: Iron oxide nanotube array formation proceeds in four stages.

Representative SEM images of the surface and cross-sectional morphologies for the single layer nanotube arrays are shown in Figure 2.11. The micrographs reveal that the single layer nanotubes were circular with smooth cross sections.

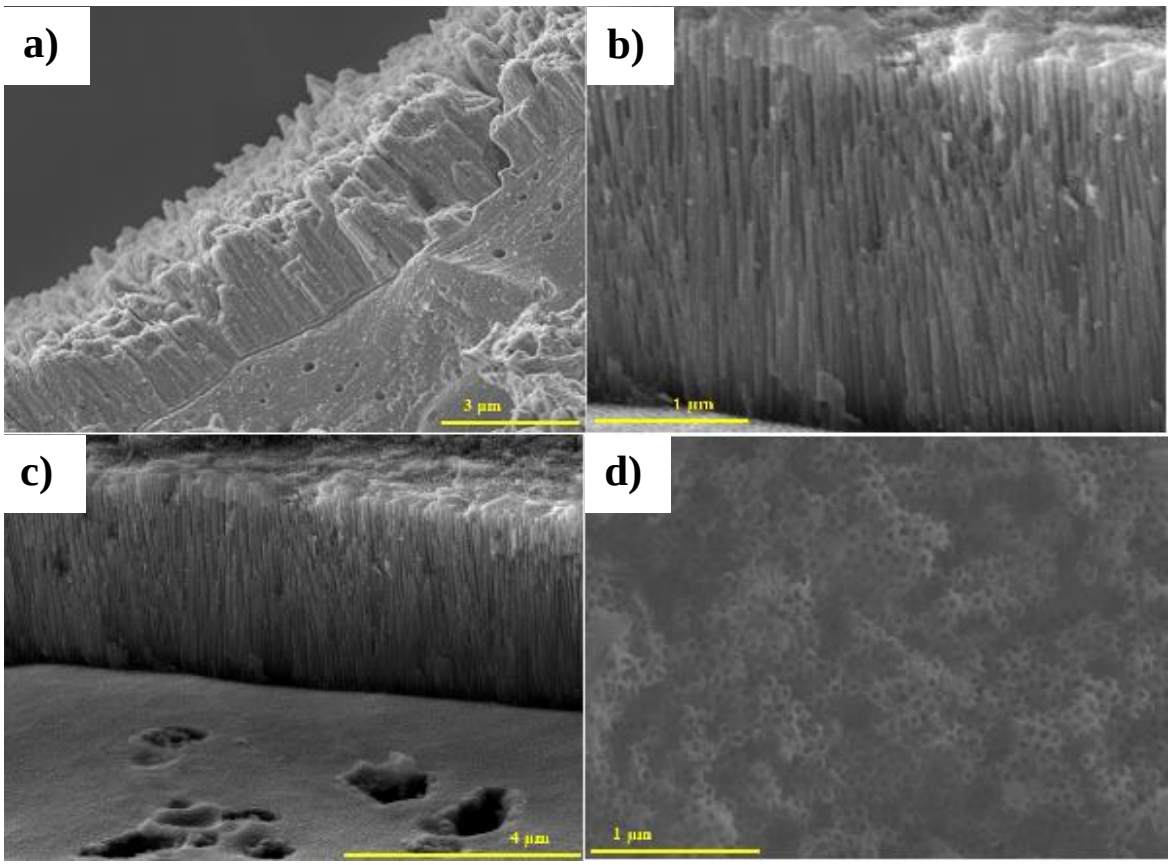

Figure 2.11: Scanning electron micrographs of single layer nanotube arrays showing typical cross-sections (a-c), and d) top view.

2.4.1.2 Multilayer Nanotube Arrays

Growth patterns for the multilayer nanotube arrays were similar to those for the single layer nanotube arrays, except that the layers were stacked on top of each other in the multilayer arrays. Multilayer nanotubes were achieved by alternating the potential from a higher value (45 V) where nanotubes could form, to a lower value (20 V) where no voltage-aided chemical dissolution occurs, thus allowing for separation between layers. At the upper pulse value of 45 V, nanotube formation proceeded in a similar fashion to that of single layer nanotubes as described above. However, upon applying the lower pulse potential, the electric field was too weak for directed nanotube growth. Therefore, dissolution is non-directional, resulting in the formation of layers.

The nanotube layer thickness in multilayer nanotube arrays was a linear function of the upper pulse time (Figure 2.12). Therefore, the number and thickness of nanotube layers could be controlled precisely, with a maximum of seven layers. Extrapolating the plot of the nanotube layer thickness against the upper pulse time revealed that the formation of each new layer of nanotubes started approximately 20 s after the upper voltage pulse was applied. A closer examination of the current response for multilayer nanotube synthesis (Figure 2.13) corroborates this observation. About 20 s after the application of the upper pulse potential, the current begins to increase, indicating the onset of the chemical dissolution stage for the newly formed iron oxide layer. The lower potential only controlled layer separation. Also, the application of the lower potential pulse for time periods less than 30 s resulted in poor layer separation and a nanotube morphology that was similar to that of single layer nanotubes.

Figure 2.14 shows SEM images for nanotube arrays with three, five, and seven layers, synthesized by applying corresponding numbers of voltage pulse cycles. Multilayer nanotubes, like single layer nanotubes, were circular with smooth cross sections. Figure 2.15 shows the nanotube layer boundaries in detail. It is interesting to note that some portions of adjacent layers overlap (Figure 2.15d), thus holding the layers together.

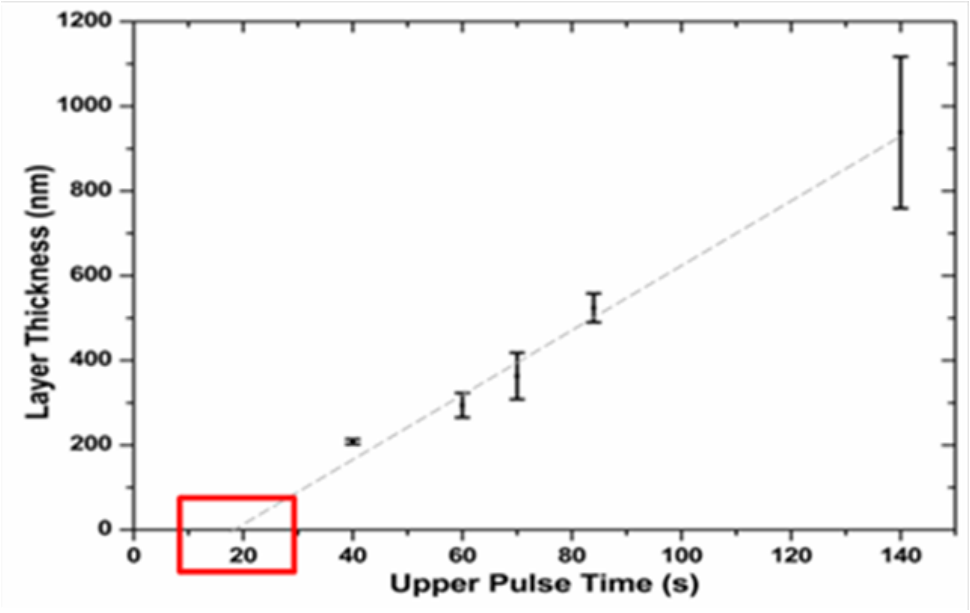

Figure 2.12: Multilayer nanotube layer thickness varies linearly with upper pulse time. New nanotube layer formation begins ~20 s, noted by the red box, after application of the upper pulse potential.

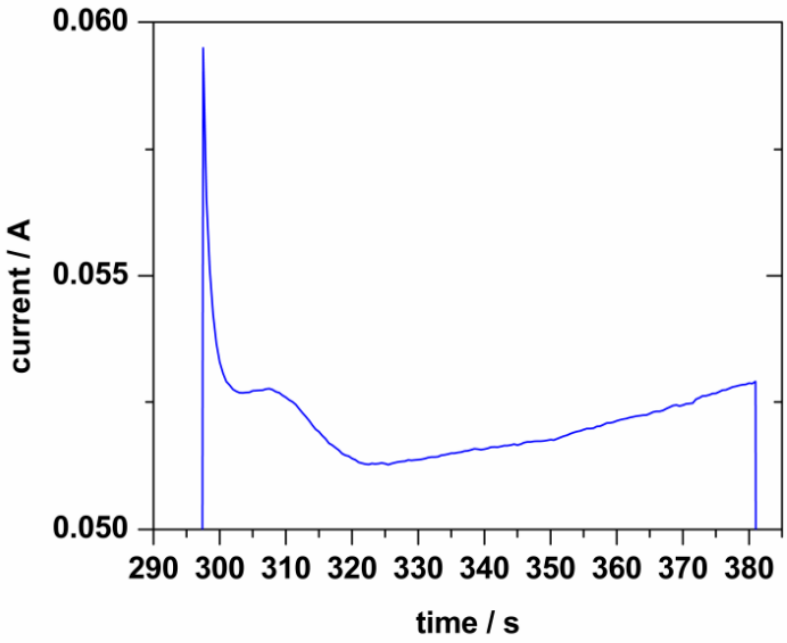

Figure 2.13: A magnified view of current response for one upper cycle during multilayer nanotube synthesis. New layer formation begins ~20 s after application of the upper voltage pulse.

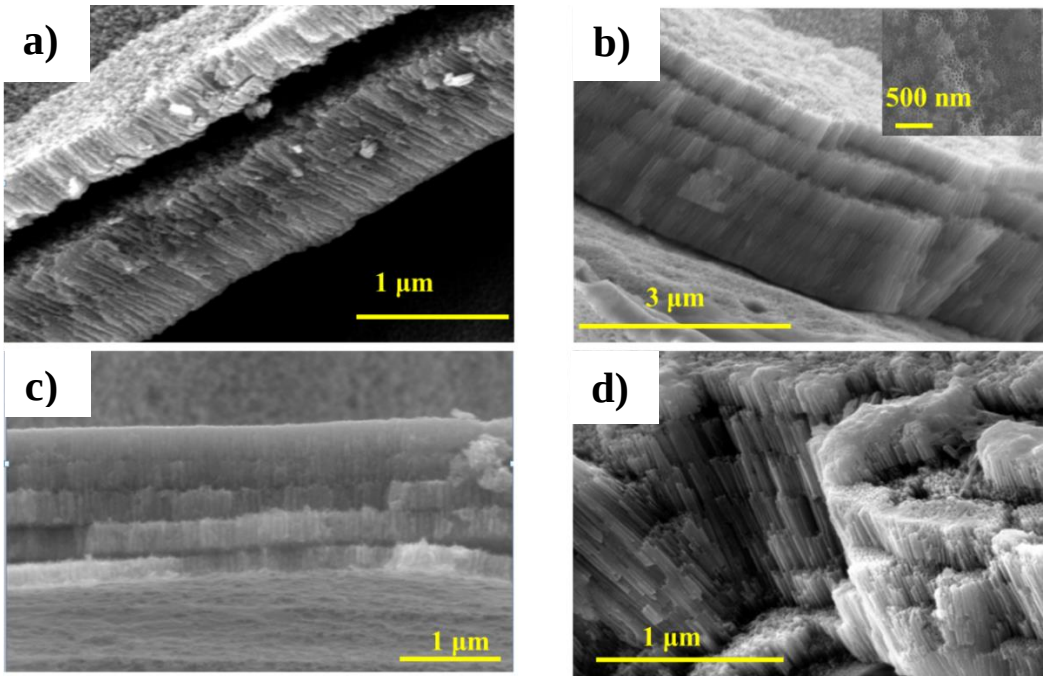

Figure 2.14: Multilayer nanotube arrays with a) three, (b, c) five, and (d) seven layers.

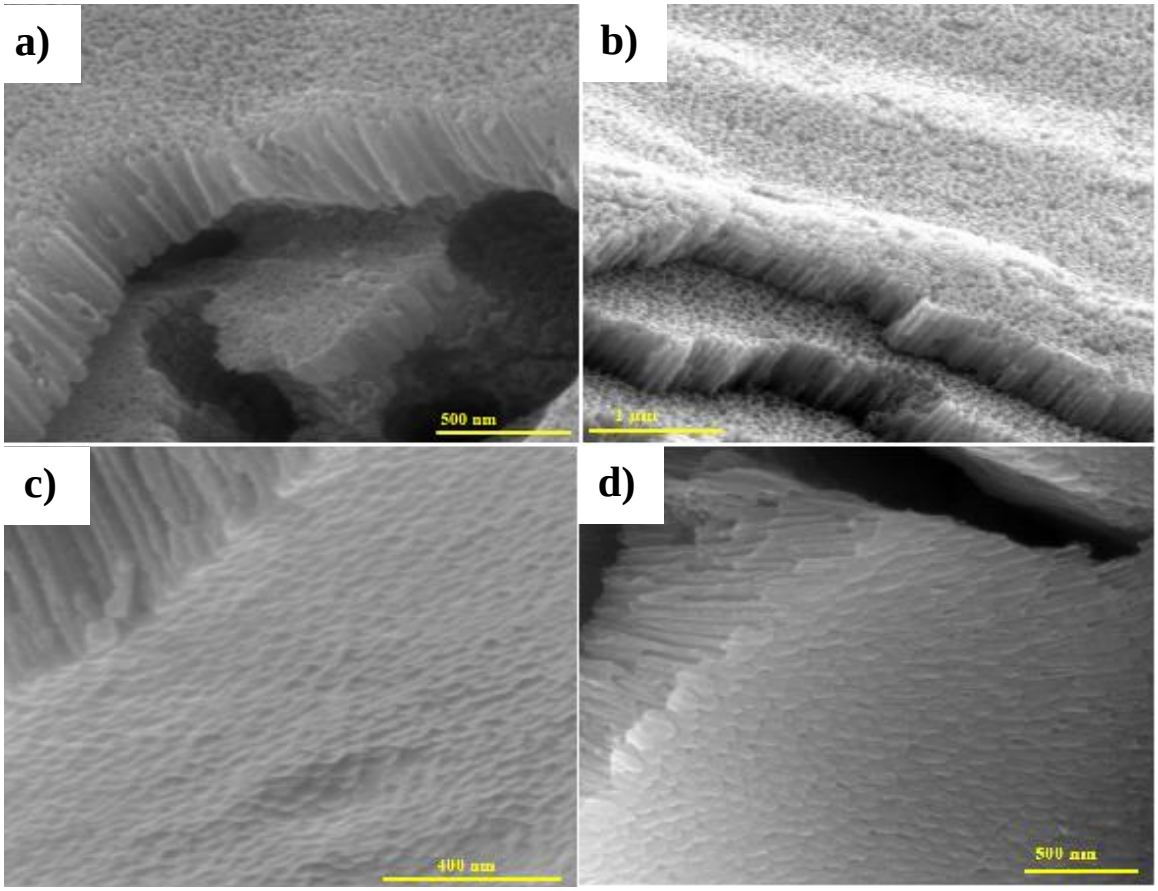

Figure 2.15: a, b) Magnified views of nanotube layer boundaries, c) round nanotube bottoms, and d) interlayer overlap in multilayer nanotube arrays.

2.4.1.3 Wave-like Nanotube Arrays

During single layer nanotube synthesis, it was found that the nanotube diameter varies linearly with the holding voltage (30 – 60 V) (Figure 2.16). A similar trend was observed by other researchers [10]. Therefore, we postulated that a triangular voltage input in the 30 – 60 V range would effect a smooth variation in the diameter of nanotubes, resulting in the formation of the wave-like nanotube morphology. The increase in diameter with holding voltage is to be expected, given that higher voltages are more polarizing to chemical bonds in the oxide structure, making oxide dissolution easier. Also, as observed with single layer and multilayer nanotube array synthesis, the measured current increases as the pitting process continues during the synthesis of wave-like nanotube arrays (Figure 2.5). Representative SEM images for wave-like

nanotube arrays are shown in Figure 2.17. The micrographs reveal that the wave-like nanotubes were circular with an undulating cross section. From a geometrical perspective, an undulating morphology should exhibit a higher surface area, which is observed in Table 3.1.

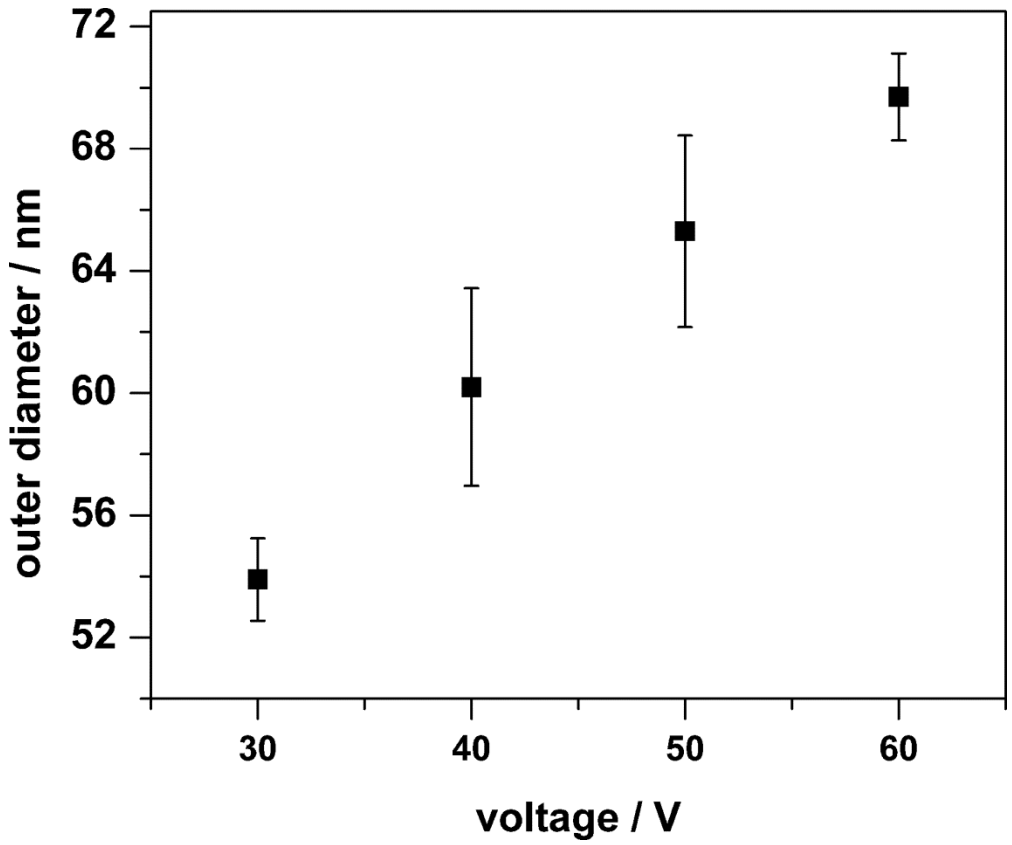

Figure 2.16: Variation of nanotube diameter with holding voltage for single layer nanotube arrays.

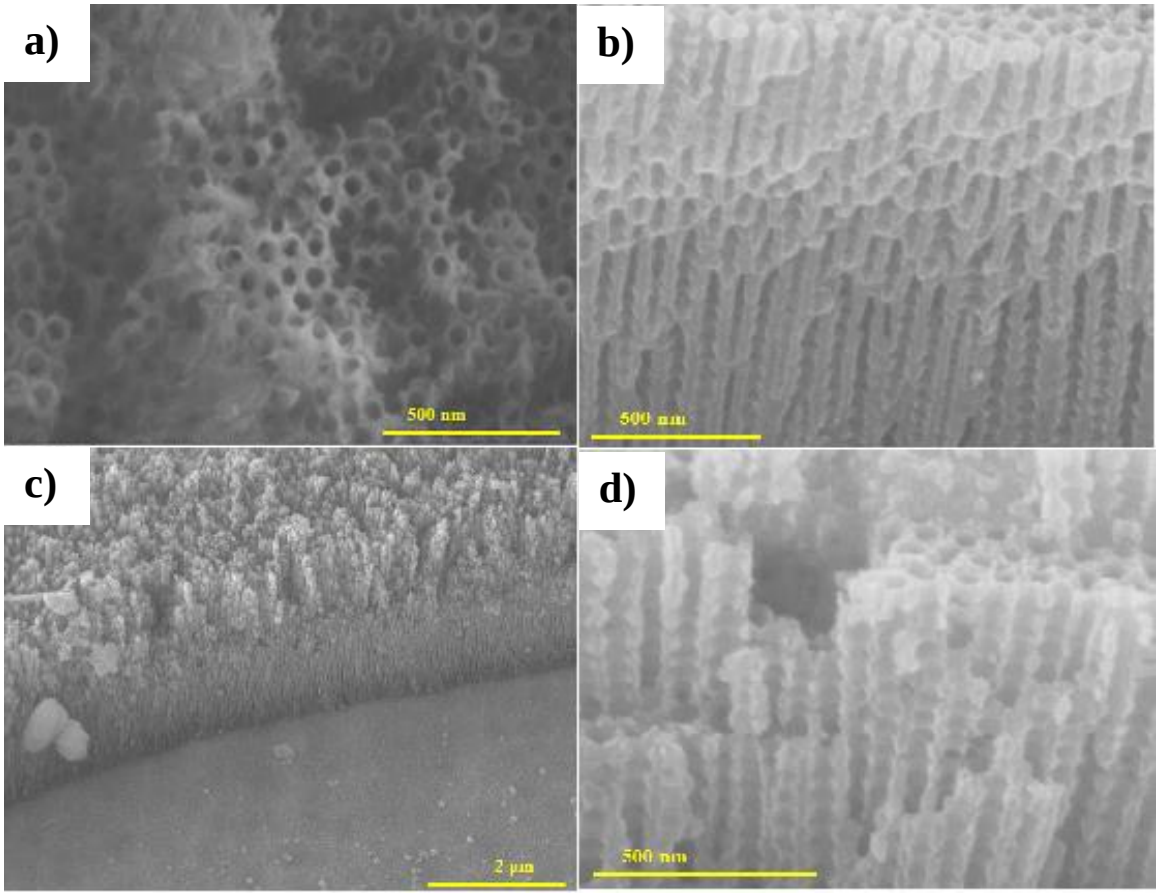

Figure 2.17: SEM showing wave-like nanotube arrays. (a) Top-view, (b-d) cross-sectional view.

2.4.2 Bulk Materials Characterization

The as-synthesized nanotube arrays were amorphous and required thermal treatment to crystallize the films. Various calcination schemes were investigated in air and in oxygen atmospheres; phase pure hematite was achieved in the oxygen atmosphere.

2.4.2.1 Nanotube Annealing in an Oxygen Atmosphere

Following a thermal treatment scheme suggested by the literature, annealing in an oxygen atmosphere at 600 °C for two hours with heating/cooling rates of 2 °C/min caused the crystallization of the nanotube films into phase-pure hematite (JCPDS 04-008-7623) [25]. XRD patterns of the nanotube films annealed under oxygen are shown in Figure 2.18. For all samples, the nanotube film thickness was ~3 µm, therefore; the underlying iron substrate was detected by

XRD (indicated by a diamond above the diffraction patterns). The amorphous and crystalline nanotube films had similar morphologies under SEM. The mean crystallite sizes, as estimated from the Scherrer formula using peak broadening of the XRD patterns, were 11, 11, and 9.6 nm for single layer, multilayer, and wave-like nanotube arrays, respectively (Table 2.1). Mean crystallite sizes were comparable to mean nanotube wall thicknesses for all three morphologies, as shown in Table 2.1. This strongly suggests that the nanotube walls are composed of only one crystallite, an advantageous property for photocatalysis applications as grain boundaries have been shown to act as recombination centers, which reduce the photoconversion efficiency [26-27].

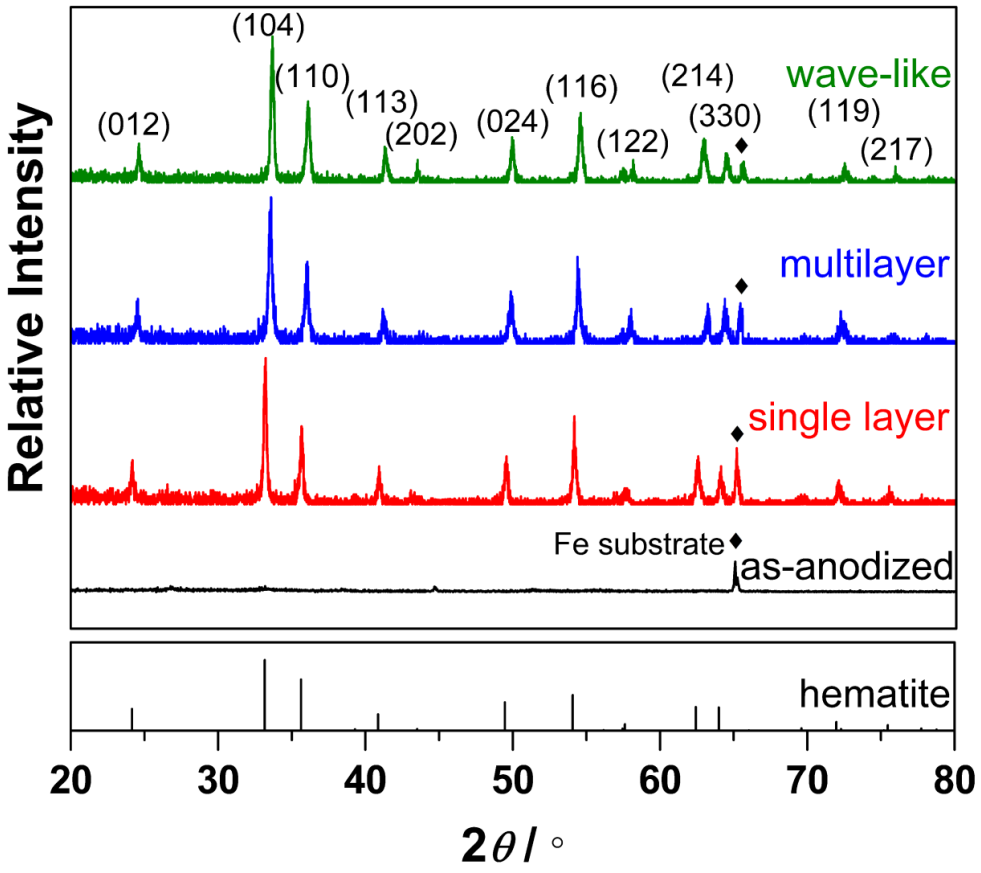

Figure 2.18: X-ray diffraction patterns for as-synthesized and single layer, multilayer, and wave-like nanotube arrays annealed in an oxygen atmosphere. Annealed samples were composed of phase-pure hematite.

Table 2.1: Average crystallite size compared to nanotube wall thickness for single layer, multilayer, and wave-like nanotubes.

	Single Layer	**Multilayer**	**Wave-like**
Mean crystallite size (nm)	11	11	9.6
Mean nanotube wall thickness (nm)	9.6	10	9.5

2.4.2.2 Nanotube Annealing in Air

Initial attempts for the thermal treatment of nanotube arrays used an air atmosphere. Calcining in air was investigated by varying the calcination temperature, heating/cooling rates, and calcination hold times. However, none of the schemes investigated in air resulted in pure-phase hematite. Instead, the materials were composed of mixtures of magnetite, maghemite, and hematite. Magnetite and maghemite, a metastable phase between magnetite and hematite, are typically not applied for photoelectrochemical water splitting. This is due to the low bandgap of magnetite (0.14 eV), which is not sufficient for water photo-oxidation, and the occurrence of a high density of cation vacancies in maghemite, respectively. Cation vacancies in maghemite result in high electron-hole recombination rates [28]. Below is a summary of the experimental investigation carried out in an effort to maximize the yield of the hematite phase in the nanotube films.

2.4.2.3 Effect of Calcination Temperature

Following a previous calcination procedure developed within our research group for iron oxide nanotubes [29], a heating and cooling rate of 1.77 °C/min, and an annealing hold time of 1 h were chosen. Because the nanotube films flaked off of the substrate at temperatures ≥550 °C and because crystallization of the films did not occur below 300 °C, annealing temperatures were

chosen between 300 and 500 °C. Under these conditions, the nanotube films were composed of hematite and maghemite as shown in Table 2.2. During thermal treatment, amorphous iron oxide undergoes the following transformation [28]:

$$\text{Magnetite } (Fe_3O_4) \rightarrow \text{Maghemite } (\gamma\text{-}Fe_2O_3) \rightarrow \text{Hematite } (\alpha\text{-}Fe_2O_3)$$

A hold temperature of 300 °C was too low for the transformation of maghemite to hematite, and the nanotube samples were composed solely of maghemite. There was an increase in the phase fraction of hematite with increasing temperature, up to 450 °C. However, at 500 °C, the phase fraction of hematite dropped to 28%. No further analysis was carried out to explain this trend as the hematite yield was low.

Table 2.2: Phase fraction of hematite under an air atmosphere increases with annealing temperature until a turning point of 450 ℃.

Hold Temperature/ °C	% Maghemite	% Hematite
300	100	0
400	63	37
450	58	42
500	72	28

2.4.2.4 Effect of Heating/Cooling Rate

To investigate the effect of the heating and cooling rate on the phase fraction of hematite achieved, an annealing hold time of 1 h and an annealing time of 450 °C were used. Table 2.3 summarizes our findings. Increasing heating/cooling rates up to 7.5 ℃/min resulted in a decrease in the total phase fraction of hematite because of a reduction in the total annealing time, hence reducing the amount of time for transformation from maghemite to hematite. For a heating/cooling rate of 10 °C/min, no maghemite was observed, suggesting a direct transformation of magnetite to hematite [28].

Table 2.3: Phase fraction of hematite under an air atmosphere increases with a reduction in heating/cooling rates. At the high heating/cooling rate of 10 ℃/min, magnetite transforms directly to hematite.

Heating/cooling Rate (°C/min)	% Magnetite	% Maghemite	% Hematite
1.77	0	58	42
5	0	64	36
7.5	0	68	32
10	50	0	50

2.4.2.5 Effect of Calcination Hold Time

To investigate the effect of the calcination hold time on the total phase fraction of hematite, a calcination temperature of 450 °C and a heating/cooling rate of 1.77 °C/min were used. Short holding times of less than 30 minutes resulted in 100% non-stoichiometric iron oxides (Table 2.4). At an annealing hold time of 1 h, there was a mixture of hematite and maghemite. Beyond 1 h, a disproportionation reaction of maghemite resulted in an increased phase fraction of hematite together with the non-photoactive magnetite [28]. The fraction of hematite increased with longer annealing hold times, up to 71% observed after 2 h. However, while increasing hold times under this annealing scheme seemed promising, extended hold times longer than 2 h resulted in the flaking of the nanotube films from the iron substrate. Figure 2.19 shows diffraction patterns for materials annealed in an air atmosphere at 450 °C, with cooling rates of 1.77 °C/min. After consideration of all annealing schemes investigated, it was decided to anneal all nanotube array samples used for photocatalytic performance testing (described in the next chapter) in an oxygen atmosphere.

Table 2.4: Phase fraction of hematite under an air atmosphere increases with increasing annealing time.

Annealing Hold Time (h)	% Magnetite	% Maghemite	% Hematite	% Non-stoichiometric Iron Oxides
0.5	0	0	0	100
1	0	58	42	0
1.5	34	0	66	0
2	29	0	71	0

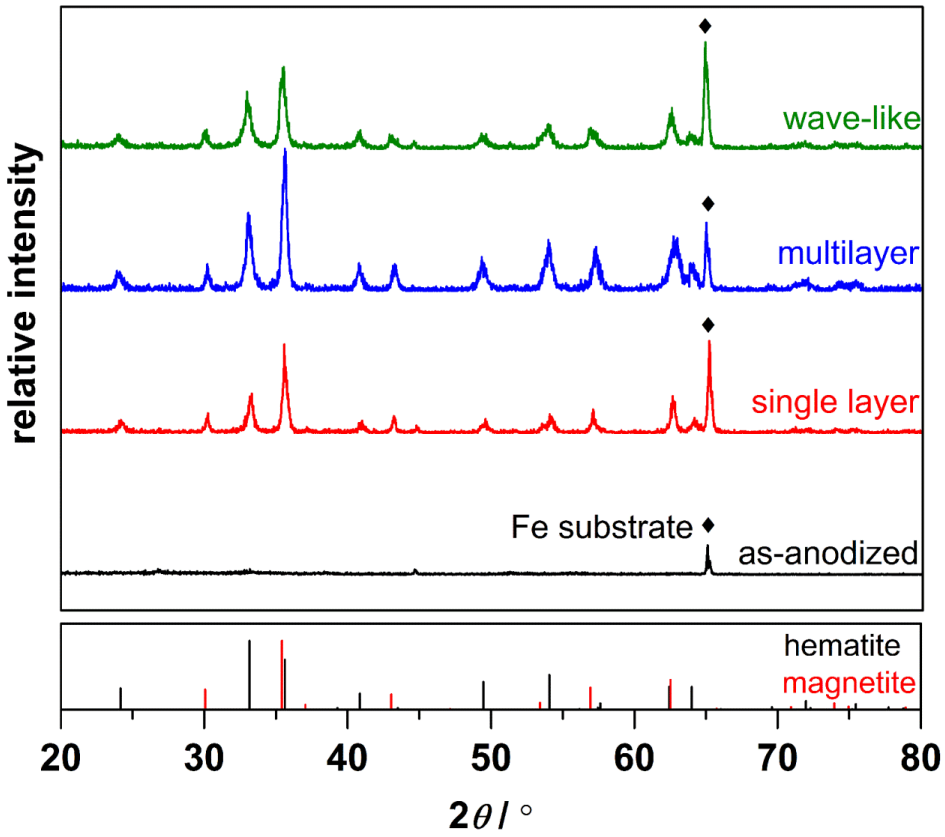

Figure 2.19: X-ray diffraction patterns for as-synthesized and single layer, multilayer, and wave-like nanotube arrays annealed in an air atmosphere at 450 ℃, with cooling rates of 1.77 ℃/min. Samples were composed of a mixture of hematite and magnetite phases.

2.5 Summary and Conclusions

The synthesis of single layer, multilayer and wave-like hematite nanotube arrays using the electrochemical anodization technique and the characterization of their bulk and morphological properties are presented. The multilayer nanotube arrays were hypothesized to improve the photoconversion efficiency as a consequence of enhanced light absorption due to scattering effects at the layer interfaces. The wave-like nanotube arrays were expected to possess increased electrochemical surface areas compared to straight nanotubes, therefore enhancing photocatalytic rates. The nanotube morphology was strongly dependent on the synthesis conditions; four distinct stages of nanotube array formation were identified by tracking the

current response and film resistances during synthesis. Fine tuning of the morphology and understanding the impact of structure on performance could help create improved nanoscale devices for various photoelectrochemical applications, such as water oxidation.

2.6 References

[1] Beermann, N.; Vayssieres, L.; Lindquist, S. -E.; Hagfeldt, A. Photoelectrochemical Studies of Oriented Nanorod Thin Films of Hematite. *J. Electrochem. Soc.* **2000**, *147*, 2456.

[2] Rangaraju, R. R.; Panday, A.; Raja, K. S.; Misra, M. Nanostructured Anodic Iron Oxide Film as Photoanode for Water Oxidation. *J. Phys. D: Appl. Phys.* **2009**, *42*, 135303.

[3] Sivula, K.; Le Formal, F.; Gratzel, M. Solar Water Splitting: Progress Using Hematite (α-Fe_2O_3) Photoelectrodes. *ChemSusChem.* **2011**, *4*, 432.

[4] Walter, M. G.; Warren, E. L.; McKone, J. R.; Boettcher, S. W.; Mi, Q. X.; Santori, E. A.; Lewis, N. S. Solar Water Splitting Cells. *Chemical Reviews* **2010,** *110*, 6446.

[5] Ghicov, A.; Schmuki, P. Self-ordering Electrochemistry: A Review on Growth and Functionality of TiO_2 Nanotubes and Other Self-Aligned MO_x Structures. *Chem. Commun.* **2009**, 2791.

[6] Jia, C-J.; Sun, L-D.; Yan, Z-G.; You, L-P.; Luo, F.; Han, X-D.; Pang, Y-C.; Zhang, Z.; Yan, C-H.; Single-Crystalline Iron Oxide Nanotubes, *Angew. Chem, Int. Ed.* **2005**, *44*, 4328.

[7] A. Mao, K. Shin, J. K. Kim, D. H. Wang, G. Y. Han and J. H. Park, Controlled Synthesis of Vertically Aligned Hematite on Conducting Substrate for Photoelectrochemical Cells: Nanorods Versus Nanotubes, *ACS Appl. Mater. Interfaces* **2011**, *3*, 1852.

[8] Masuda, H.; Fukuda, K. Ordered Metal Nanohole Arrays Made by a Two-Step Replication of Honeycomb Structures of Anodic Alumina. *Science* **1995**, *268*, 1466.

[9] Prakasam, S. E.; Varghese, O. K.; Paulose, M.; Mor, G. K.; Grimes, C. A. Synthesis and Electrochemical Properties of Nanoporous Iron (III) Oxide by Potentiostatic Anodization. *Nanotechnology* **2006**, *17*, 4285.

[10] Latempa, T. J.; Feng, X.; Paulose, M.; Grimes, C.A. Temperature-Dependent Growth of Self-Assembled Hematite Nanotube Arrays: Rapid Electrochemical Synthesis and Photoelectrochemical Properties. *J. Phys. Chem. C.* **2009**, *36*, 16293.

[11] Rangaraju, R., Misra, M., Nanostructured Anodic Iron Oxide Film as Photoanode for Water Oxidation., *J. Phys*. **2009**, *42*, 135303.

[12] Mohapatra, S. K.; John, S.E.; Banerjee, S.; Misra, M. J. Water Photooxidation by Smooth and Ultrathin α-Fe_2O_3 Nanotube Arrays. *Chem. Mater.* **2009**, *21*, 3048.

[13] Ozkar, S. Enhancement of Catalytic Activity by Increasing Surface Area in Heterogeneous Catalysis. *Appl. Surf. Sci.* **2009**, *256*, 1272.

[14] Agilent Technologies, Inc. (2013). *E364xA User's and Service Guide*. Santa Clara, CA.

[15] Guan, D.; Wang, Y. Synthesis and Growth Mechanism of Multilayer TiO_2 Nanotube Arrays. *Nanoscale* **2012**, *4*, 2968.

[16] Susanta, K. M.; Shiny, E. J.; Subarna, B.; Mano, M. Water Photo-oxidation by Smooth and Ultrathin α–Fe_2O_3 Nanotube Arrays. *Chem. Mater*. **2009**, *21*, 3048.

[17] Alexander, B. D.; Kulesza, P. J.; Rutkowska, I.; Solarska. R.; Augustynski, J. Metal Oxide Photoanodes for Solar Hydrogen Production, *J. Mater. Chem*. **2008**, *18*, 2298.

[18] Abdel-All, A.; Elshafieb, A.; Elhawaryb, M. DC Electric-field Effect in Bulk and Thin –film $Ge_5As_{38}Te_{57}$ Chalcogenide Glass., *Vacuum* **2000**, *59*, 845.

[19] Banihashemian, S. M.; Hajghassem, H.; Erfanian, A.; Aliahmadi, M.; Mohtashamifar, M.; Mosakazemi, S. M. Observation and Measurement of Negative Differential Resistance on PtSi Schottky Junctions on Porous Silicon. *Sensors* **2010**, 10, 1012.

[20] Tilley, R. J. D. Understanding Solids: The Science of Materials. 2nd Ed. *Wiley* **2013**.

[21] Isohama, Y.; Nakajima, N.; Watanabe, G.; Mizumaki, M.; Kawamura, N.; Maruyama, H. Intrinsic Effect of the Electric Field on Ti-O Bonding in Ferroelectric $BaTiO_3$ Probed by Resonant X-Ray Emission Spectroscopy. *Jpn. J. Appl. Phys*. **2011**, *50*, 09NE04.
[22] Callister, W. D, Materials Science and Engineering: An Introduction, *John Wiley & Sons, Inc*. **2010**, 8th Ed.
[23] Burstein, G. T.; Pistorius, P. C. Growth of Corrosion Pits on Stainless Steel in Chloride Solution Containing Dilute Sulphate. *Corros. Sci.* **1992**, *33*, 1885.
[24] Burstein, G. T.; Souto, R. M. Observations of Localized Instability of Passive Titanium in Chloride Solution. *Electrochim. Acta* **1995**, *40*, 1881.
[25] Zhang, Z.; Hossain, F.; Takahashi, T.; Self-assembled Hematite Nanotube Arrays for Photoelectrocatalytic Degradation of Azo Dye Under Simulated Solar Light Irradiation, *Appl. Catal. B-Environ.* **2010**, *95*, 423
[26] Dimitriadis, C. A. Influence of Grain Boundary Recombination Velocity and Grain Size on the Minority Carrier Lifetime in Polycrystalline Semiconductors, *Solid State Commun.* **1985**, *56*, 925.
[27] Joshi, D. P.; Bhatt, D. P. Theory of Grain Boundary Recombination and Carrier Transport in Polycrystalline Silicon under Optical Illumination. *IEEE Electron Dev.* **1990**, *31*, 237.
[28] Cornell, R. M.; Schwertmann, U. The Iron Oxides: Structure, Properties, Reactions, Occurrences, and Uses. *Wiley-VCH Verlarg GmbH & Co, Weinheim*. **2003**, 2nd Ed.
[29] Aurora, P. H. Photoelectrochemical Systems for Hydrogen Production, PhD Dissertation - University of Michigan, Ann Arbor, **2010**.

Chapter 3

Characterization of Hematite Nanotube Arrays for Photocatalysis

Portions of work summarized in this chapter were published in Mushove, T.; Breault, T.; Thompson, L. T. *Ind. Eng. Chem. Res.* **2015**, 54, 4285.

3.1 Introduction

The previous chapter described the design and synthesis of hematite photoanodes in various nanotube array structures: single layer, multilayer, and wave-like. Nanostructured materials offer improved performance in photocatalytic reactions due to the decoupling of light absorption and charge carrier transport [1-3], increases in the active electrochemical surface areas [4], and enhancements in light scattering [5, 6]. Scattering effects extend the amount of time that photons are trapped within the nanostructure, allowing for increased photon absorption.

In this chapter, the effects of the different morphological features of the various nanotube array structures on photoconversion efficiency were evaluated. The multilayer nanotube arrays were hypothesized to exhibit enhanced light absorption due to scattering effects at the layer interfaces, thereby improving photocatalytic performance [5]. Wang et al. reported performance improvements in dye-sensitized solar cells when using bilayered TiO_2/CeO_2 photoanodes as compared to monolayer TiO_2 photoanodes. The thin CeO_2 layer was shown to effectively scatter trapped photons, resulting in an 18% enhancement in the photoconversion efficiency [6]. The wave-like nanotube arrays were expected to possess increased electrochemical surface areas

compared to straight nanotubes and higher photocatalytic rates as the result [7]. The nanotube arrays were evaluated for use as photoanodes for water oxidation. Key properties of the materials, including the accessible electrochemical surface area and bandgap, were characterized, and their effects on photocatalytic performance were assessed. The ultimate goal was to construct nanostructure-function correlations in order to understand and develop design rules for superior performing photoanodes. Figure 3.1 is a schematic depiction showing increased light absorption due to increased scattering effects at layer interfaces in multilayer nanotube arrays, as well as increases in electrochemical surface area expected in wave-like nanotube arrays.

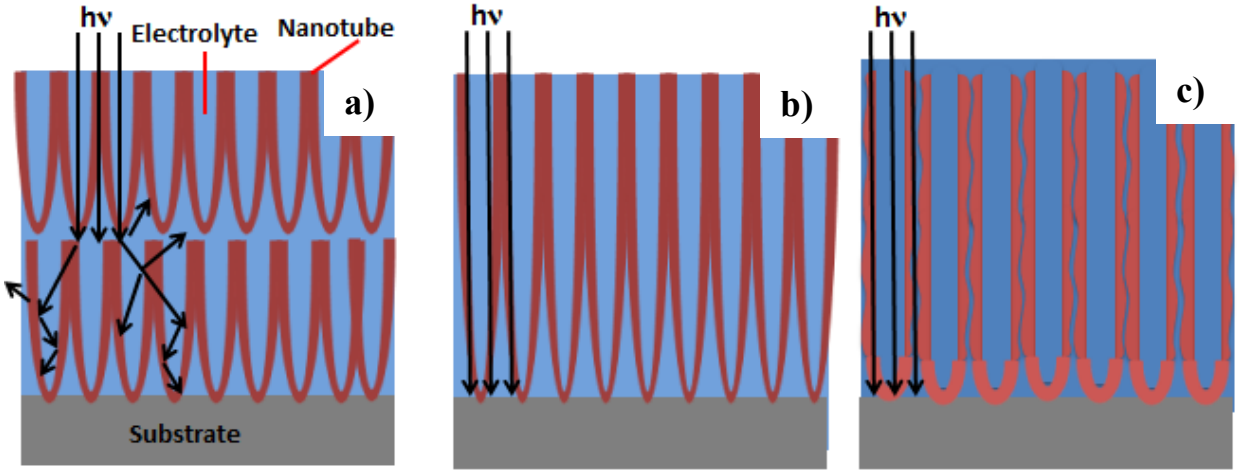

Figure 3.1: Nanotube array types investigated in this dissertation. a) Multilayer nanotube arrays promise increased light scattering at layer interfaces. (b) Single layer nanotube arrays. (c) Wave-like nanotube arrays offer larger electrochemical surface areas for photocatalytic reactions.

3.2 Experimental Method

3.2.1 Materials

Chemicals for production of the electrolytes, potassium hydroxide (ACS grade, 88%), and hydrogen peroxide (ACS grade, 30%) were purchased from Fisher Chemical. Ultrapure water (resistance 18.2 MΩ) was obtained from a Millipore Milli-Q water purification system.

3.2.2 Electrochemical Surface Area Characterization

Cyclic Voltammetry (CV) was used to estimate the nanotube array double layer capacitance based on plots of the measured current versus the scan rate. The electrochemical surface areas were then calculated based on a reference capacitance for metal oxides of 50 $\mu F/cm^2$ [8-10]. This method requires that the properties of the double-layer and space-charge region be similar between the different materials and is sufficient for comparison of such materials when tested under identical conditions [10]. The error of this method is typically measured at < 10 % [8]. Errors in the electrochemical surface area measurements were obtained by taking an average of the surface areas of three electrodes synthesized under the same anodization conditions.

3.2.3 Optical Characterization

UV-vis spectra were recorded using an Agilent-Cary 5000 spectrophotometer equipped with a Praying Mantis diffuse reflectance accessory and an iron foil as the background. Spectra were recorded in reflectance mode from 350 to 800 nm. The Kubelka-Munk function, $F(R) = (1-R)^2/2R$, was used to transform the spectra. Tauc plots were generated using this function. Using Tauc analysis, the bandgap of a material can be calculated through the following equation:

$$(h\nu F(R\infty))^{1/n} = \mathbf{A}(h\nu - E_g) \qquad \text{Equation (3.1)}$$

where h is Planck's constant, ν is the frequency of the incident light, F(R∞) represents the absorption coefficient multiplied by a factor of 2.303 divided by the film thickness [11], **A** is a material constant, and E_g is the material's bandgap. The value of the exponent, *n*, denotes the nature of the electronic transition, with $n = 0.5$ representing an allowed direct transition, and $n = 2$ representing an allowed indirect transition. A plot of $(h\nu F(R\infty))^{1/n}$ against hν can be made and the appropriate bandgap determined at the point where the line extrapolated from the linear region of the plot intersects the energy-axis ($h\nu$). This method assumes a planar electrode and approximately parabolic conduction and valence band edges with respect to the material's crystal momentum [12]. Therefore, some semiconducting materials, when nanostructured, suffer from artifacts of complex geometries, making accurate bandgap determination difficult. However, this is not the case with hematite, which exhibits a small exciton Bohr radius (discussed in detail below).

3.2.4 Photoelectrochemical Measurements

Photoelectrochemical measurements were performed in a three-electrode glass cell, as shown in Figure 3.2. The cell contained a working hematite nanotube photoanode, a Pt foil counter electrode, and a Hg/HgO reference electrode. The electrolyte was 1 M KOH (pH 13.8) degassed with ultrahigh purity nitrogen gas. Potentials are reported *vs.* the reversible hydrogen electrode (RHE) using the following equation: $V_{RHE} = V_{Hg/HgO} + 0.098\ V + 0.059\ V * pH(1\ M\ KOH)$, where 0.098 is the standard electrode potential of the Hg/HgO (1 M KOH) system *vs.* the standard hydrogen electrode (SHE).

A Gamry Instruments Series G750 potentiostat was used to perform linear sweep voltammetry (LSV) and cyclic voltammetry. LSV and CV experiments were performed at a scan rate of 50 mV/s under simulated AM 1.5G illumination using a 300 W Xe lamp (Solar Light

16S-300) at 100mW/cm^2, and the photocurrent was normalized to the geometrical surface area of the photoanode under illumination (0.25 cm^2). The Xe lamp replicates the full solar spectrum and was equipped with an AM 1.5 filter to simulate solar irradiation on the surface of the Earth. The electrolyte used was 1M KOH or 1M KOH + 0.5M H_2O_2, depending on the specific experiment. Light chopping for LSV was manually performed at ~1 Hz. Electrochemical Impedance Spectroscopy (EIS) measurements were performed in the frequency range from 100 kHz to 0.1 Hz at 1.31 V vs. RHE under dark and AM 1.5 illumination.

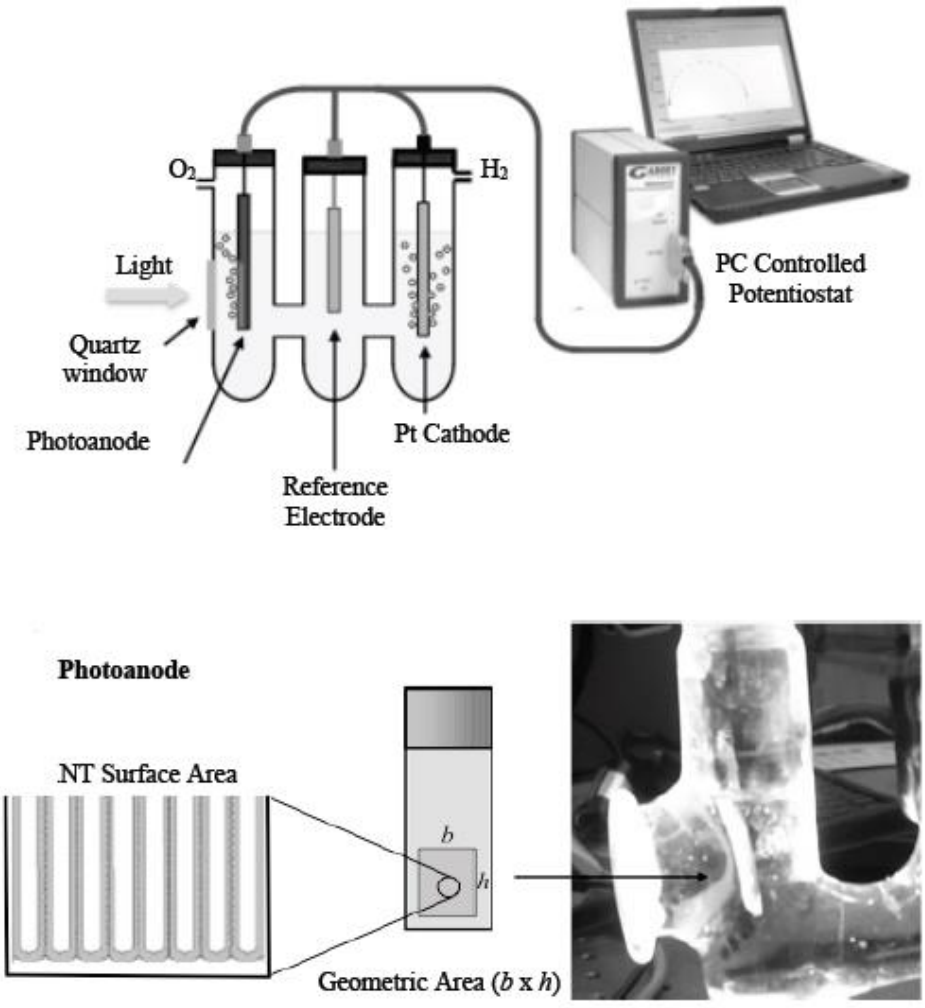

Figure 3.2: Photoelectrochemical cell setup. All electrochemical surface areas were normalized to the geometrical surface area.

The incident photon to current efficiency (IPCE) measurements were carried out using a Newport-Oriel 150 W Xe arc lamp fitted with a quarter-turn single-grating monochromator. IPCE was calculated as the ratio of the measured photocurrent to the incident photon current at each wavelength scanned, in the range of 350 – 800 nm. Sample measurements were recorded using a quartz beam splitter to simultaneously record the light output with a separate Si photodiode to adjust for lamp fluctuations. The potential of the working electrode was held at 1.31 V vs. RHE in 1 M KOH, and the absolute photocurrents were measured using a digital PAR 273 potentiostat. A small potential of 0.08 mV was applied to account for kinetic and thermodynamic overpotentials associated with experimentally splitting water [13-14]. A Stanford Instruments SR830 lock-in amplifier was connected to the output signal, which was co-fed with the reference Si photodiode into a computer equipped with custom-written LabVIEW software.

The Mott-Schottky approach at a measurement frequency of 1 kHz was used to determine the flat band potential and charge carrier densities of the nanotube arrays under dark and illumination conditions. The measurements were repeated on two films for each of the nanotube array morphologies. Measurement frequencies of 0.1, 0.5, and 3 kHz were also examined; the values for the flat band potentials and the charge carrier densities determined at these frequencies were similar to those measured at 1 kHz. A geometric surface area of 0.25 cm^2 was used for the electrodes, and the permittivity of hematite was assumed to be 80 [15]. Mott-Schottky analysis was developed with the assumption of a smooth planar electrode [14]. Therefore, when applied to complex nanostructured geometries, as in our case, the analysis only yielded useful results for single layer nanotube arrays, but not for multilayer or wave-like nanotube arrays.

3.2.5 Electrochemical Techniques

3.2.5.1 Cyclic Voltammetry (CV)

A typical cyclic voltammetry experiment involves the application of a linearly changing voltage across the working electrode. The applied voltage is changed from a lower limit, E_1, at t = 0 s, to an upper limit, E_2, at $t = t_{switch}$, then back to the lower limit, at a constant rate, ν (V/s) (Figure 3.3). Simultaneously, the current flowing through the working electrode is measured and recorded. Typical cyclic voltammograms for hematite are shown in the results section.

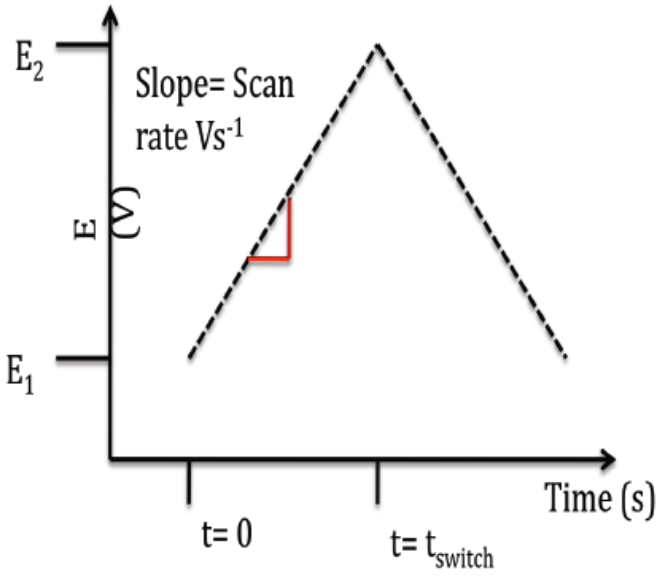

Figure 3.3: Voltage input at a working electrode during a typical cyclic voltammetry experiment.

3.2.5.2 Linear Sweep Voltammetry (LSV)

An LSV experiment is similar to a CV experiment except that the voltage sweep is applied in only one direction, from E_1 to E_2. Example current responses in an LSV experiment under chopped light are shown in the results section.

3.2.5.3 Electrochemical Impedance Spectroscopy (EIS)

EIS is an electrochemical characterization technique that allows the measurement of the impedance of a system over a frequency range. In our experiments, a small alternating voltage signal with a 10 mV amplitude was applied, and the voltage and current responses were measured. When expressed as a Nyquist plot, EIS data reveals the different characteristic behaviors of the material at various frequencies, allowing the transport and kinetic properties to be determined [16].

3.2.5.4 Mott-Schottky Analysis

Mott-Schottky analysis allows for the determination of the flat band potential (V_{fb}) and charge carrier density (N_D) of a semiconductor electrode through a relation of the semiconductor-electrolyte interfacial capacitance (C) to the applied voltage (V) [17-18]:

$$1/C^2 = (2/(\varepsilon\varepsilon_0 \mathbf{A}^2 e N_D)) (V - V_{fb} - k_B T/e) \qquad \text{(Equation 3.2)}$$

where ε is the relative permittivity of the semiconductor material, ε_0 is the permittivity of free space, **A** is the geometric surface area of the electrode, e is the elementary charge, k_B is Boltzmann's constant, and T is the absolute temperature. At room temperature and pressure, the last term, k_BT/e, is negligible compared to the term $V - V_{fb}$. From a plot of $1/C^2$ against V, V_{fb} can be determined from the intercept on the voltage axis, while the value of N_D can be computed from the slope. The permittivity of free space, ε_0, for hematite was assumed to be 80 [15], and the geometric surface area, **A**, for our electrodes was 0.25 ± 0.03 cm^2.

3.3 Results and Discussion

3.3.1 Electrochemical Surface Area Characterization

The wave-like nanotube arrays possessed higher electrochemically active surface areas than the single layer and multilayer nanotube arrays based on results from cyclic voltammetry.

The cyclic voltammograms used to determine the electrochemical surface areas are illustrated in Figure 3.4.

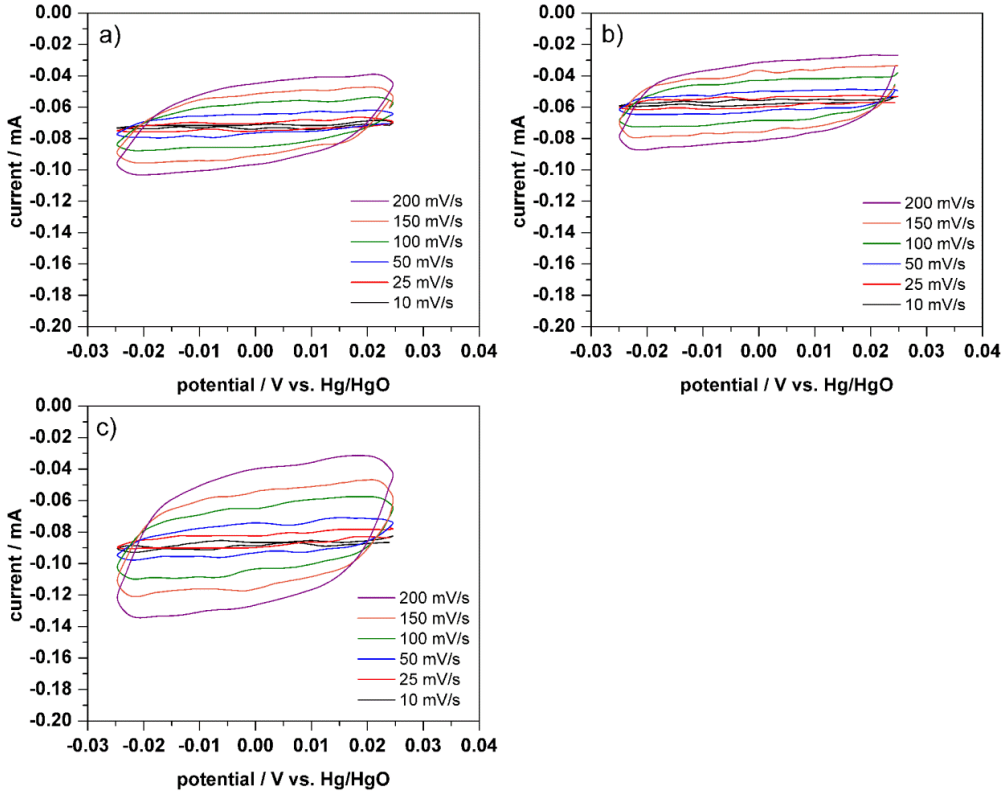

Figure 3.4: Cyclic voltammograms for a) single layer, b) multilayer, and c) wave-like nanotube arrays at varying scan rates showing the double layer capacitive current in the various nanotube morphologies.

The current at 0 V (the midpoint of the voltage range -25 to 25 mV) was plotted as a function of scan rate (Figure 3.5), and the slope was used to estimate the double layer capacitances. The estimated electrochemical surface areas for the single layer, multilayer, and wave-like nanotube arrays were determined using a reference capacitance of 50 $\mu F/cm^2$ [8-10] and are shown in Table 3.1. Single layer and multilayer nanotube arrays exhibited similar electrochemical surface areas, but both of these were less than half the electrochemical surface area of wave-like nanotube arrays. Geometric surface areas for all of the films were 0.25 cm^2.

Table 3.1: Properties of the single layer, multilayer, and wave-like nanotube arrays.

	Indirect Bandgap (eV)	Electrochemical Surface Area per Geometric Surface Area (cm^2/cm^2)	IPCE at λ = 350 nm (%)
Single layer	2.4	9.9 ± 1	4.1
Multilayer	2.4	11 ± 1	1.2
Wave-like	2.5	18 ± 2	14

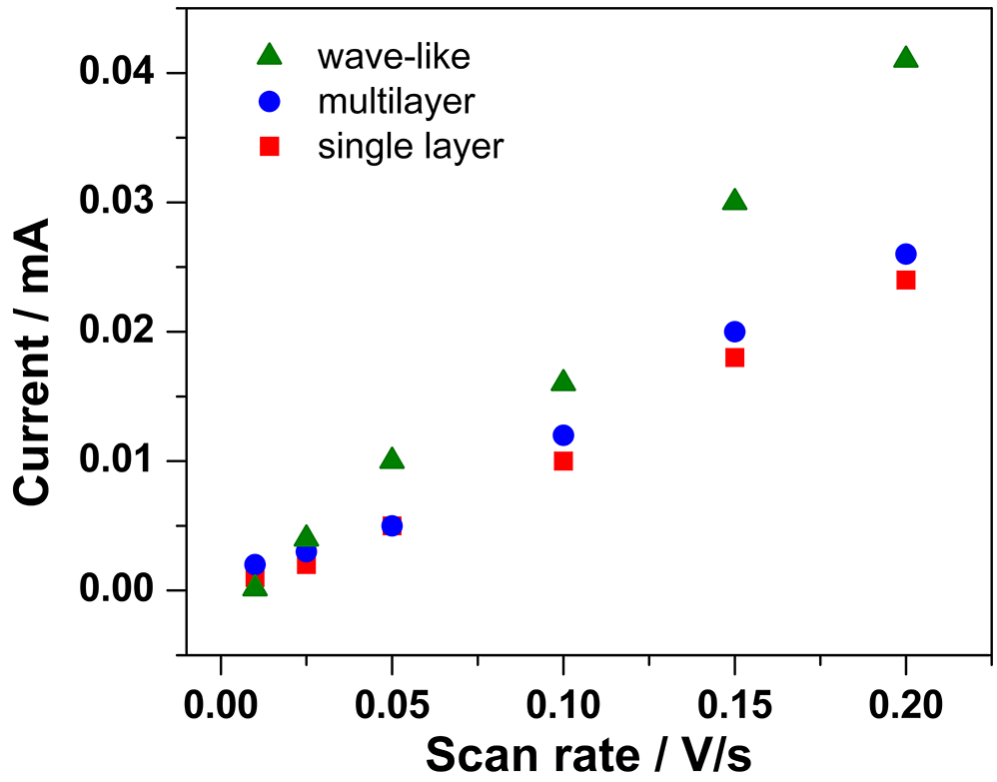

Figure 3.5: Variation of nanotube capacitive current with scan rate for single layer (red square), multilayer (blue circle), and wave-like (green triangle) nanotube arrays. The slope is proportional to the double layer capacitance, from which the electrochemical surface area was calculated.

3.3.2 Optical Characterization

Normalized diffuse reflectance spectra [12] for the single layer, multilayer, and wave-like nanotube arrays are illustrated in Figure 3.6a. Similar optical properties were observed for all three morphologies, with the absorption onset occurring at ~ 600 nm and additional absorption at ~ 450 nm. The optical characteristics of the nanotube films are consistent with hematite

exhibiting a direct bandgap of ~2.4 eV as determined from the Tauc plot in Figure 3.6b and an indirect bandgap of ~1.9 eV (from Figure 3.7). These bandgap values are consistent with the optical absorption properties of hematite reported in literature [1, 19-22]. Because Tauc analysis was developed for planar electrode architectures, using such an analysis for some semiconductor materials, especially when nanostructured, can yield inaccurate data for the optical and electronic properties. For thin films and other low-dimensional nanostructures, the exciton Bohr radius is an important parameter, defining electronic and optical behavior. Quantum confinement effects arise when the material size is smaller than the exciton Bohr radius [12, 23]. The exciton Bohr radius is the distance over which a bound state can be formed via the Coulombic interaction between an electron in the conduction band and a hole in the valence band. Because the exciton Bohr radius of hematite (~5 nm) [12] is smaller than the wall thickness (~10 nm) of the nanotube arrays synthesized in this work (discussed in previous chapter), changes in the band structures of the nanotube arrays developed herein from the bulk characteristics can be assumed as negligible, and no artifacts due to nanostructuring are expected [24].

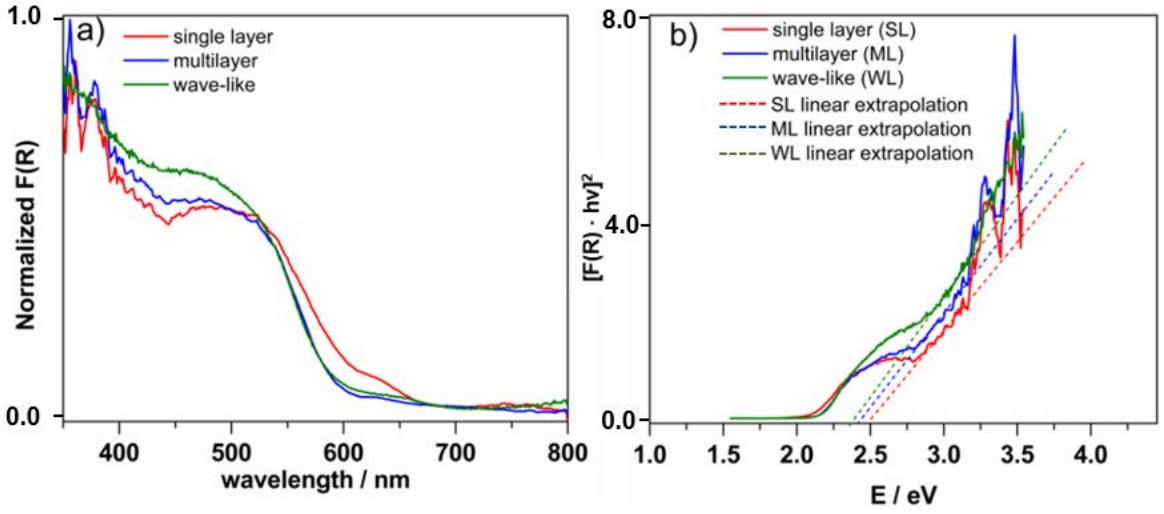

Figure 3.6: a) Diffuse reflectance spectra of single layer, multilayer, and wave-like nanotube arrays. b) Tauc plot for direct bandgap determination for the different nanotube arrays.

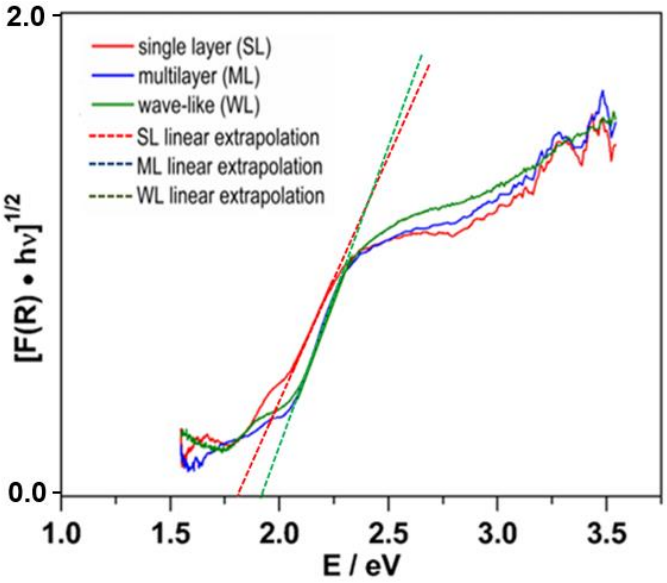

Figure 3.7: Tauc plots for indirect bandgap determination for single layer, multilayer, and wave-like nanotube arrays.

3.3.3 Photocatalytic Performance

To evaluate the photocorrosion resistance of the hematite materials synthesized in this work, chronoamperometry experiments were performed on single layer nanotube array electrodes at 1.3 V *vs.* RHE. Since photocorrosion resistance was being tested for the hematite phase and the different morphologies that we synthesized were composed of hematite, it was sufficient to evaluate only one of the three morphologies. The two photoanodes shown in Figure 3.8 were synthesized at a holding voltage of 30 V. Photoanode 1, shown in red, was evaluated before the photon flux from the lamp in the solar simulator equilibrated. A steady photocurrent was reached after approximately 1.5 h. Photoanode 2, shown in blue, was evaluated immediately after the first photoanode. As shown in Figure 3.8, the photoanodes exhibited steady photocurrents for at least 3 h, demonstrating their stability under photo-illumination [25].

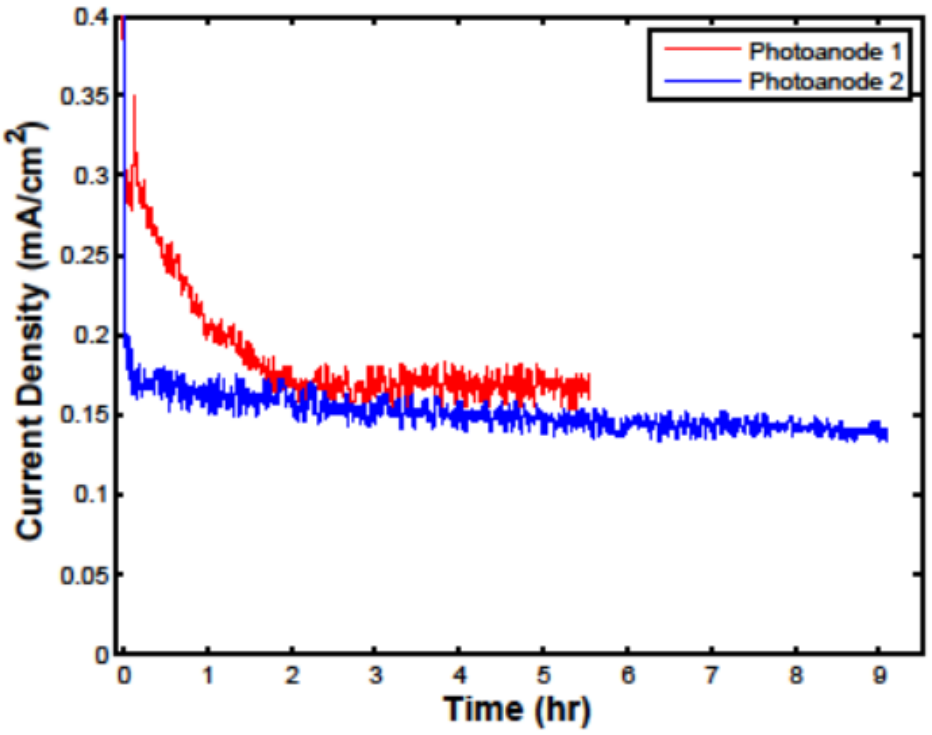

Figure 3.8: Current density of hematite nanotube arrays measured by chronoamperometry. The materials were photocorrosion resistant for at least 3 h.

As discussed above, Tauc analysis revealed that the nanotube arrays prepared in this work exhibited an indirect bandgap of ~1.9 eV and a direct bandgap of ~2.4 eV. While both bandgaps are thermodynamically sufficient to drive the water oxidation reaction (1.23 eV), incident photon to current efficiencies (IPCE) for the nanotube samples suggest that the indirect bandgap is not utilized during water oxidation (Figure 3.9). This poor utilization has been attributed to charge trapping associated with the lower energy electronic transition [13]. Other techniques, such as doping [4] and surface modification [14] could increase utilization in the longer wavelengths for water oxidation. However, such techniques are beyond the scope of this dissertation.

The IPCE values for the water photo-oxidation reaction measured for the single layer nanotube arrays were consistent with previous literature reports regarding hematite [13, 26-27].

At an illumination wavelength of 350 nm, the IPCE value for the wave-like nanotube arrays was ~3 times higher than that for the single layer nanotube arrays and ~12 times higher than that of the multilayer nanotube arrays. The water photo-oxidation efficiency in a material is a product of the photon absorption efficiency, the photogenerated charge separation efficiency, and the hole consumption efficiency at the semiconductor-electrolyte interface [28]. The photon absorption efficiency depends on the semiconductor's optical properties, while the charge separation efficiency depends on the recombination dynamics of the material [4]. We showed that single layer, multilayer, and wave-like nanotube arrays exhibited similar optical properties. This strongly suggests that the differences in the photocatalytic performances of three morphologies were due to differences in either the bulk charge transport properties of the electrodes or to the rate of hole consumption at the semiconductor-electrolyte interface. Following the work of Warren et al. [28], we distinguished the effects of bulk and surface charge recombination in the different morphologies by performing linear sweep voltammetry and electrochemical impedance spectroscopy as further discussed below.

The differences in the IPCE values at low wavelengths were a result of differences in the nanostructures, with factors such as accessible electrochemical surface area and the presence of layer interfaces playing a central role. The electrochemical surface areas for the single layer and multilayer nanotube arrays were similar (see Table 3.1), while that for the wave-like nanotube arrays was approximately 1.8 times that for the single layer nanotube arrays. The IPCE values and LSV results (Figure 3.10) exhibited a similar trend with regard to the electrochemical surface areas for the single layer and wave-like nanotube arrays, as would be expected. Based on the similarities in the surface areas of the single layer and multilayer nanotube arrays, we ruled out surface area differences between the two morphologies as the cause of the observed

photocatalytic performances. The major structural difference between single layer and multilayer nanotube arrays was the presence of layer interfaces in the multilayer morphology. This led us to hypothesize that differences in the photocatalytic performance between these morphologies were a result of the layer interfaces. The effect of the interface layers on the water photo-oxidation efficiency was investigated using electrochemical impedance spectroscopy as described below.

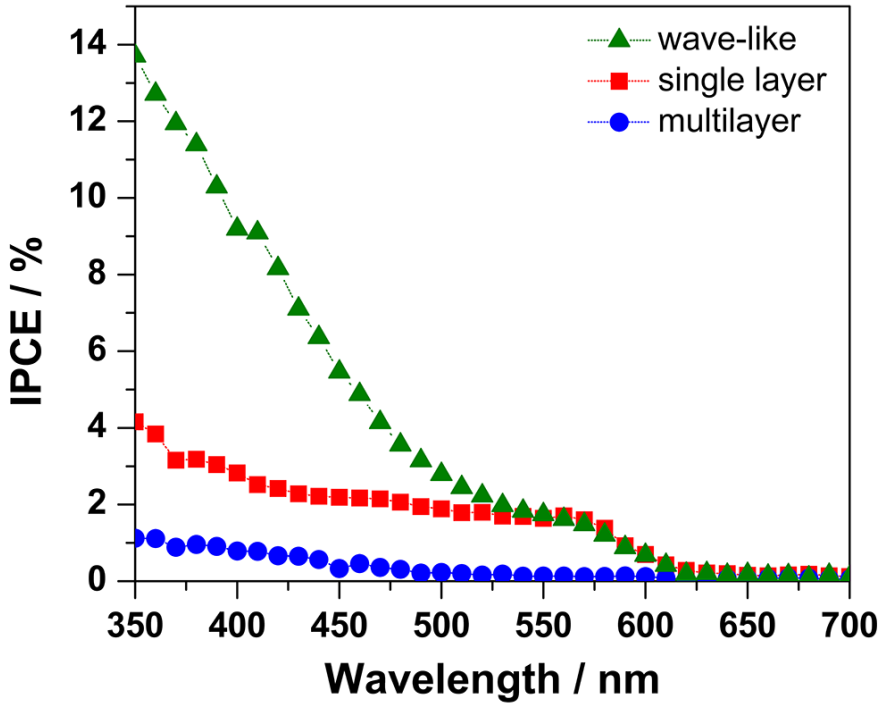

Figure 3.9: IPCE for the water photo-oxidation reaction for single layer, multilayer, and wave-like nanotube arrays at 0.4 V vs. Hg/HgO in 1M KOH.

The photocurrent response to applied anodic potentials for the three morphologies was investigated under chopped light using linear sweep voltammetry, as shown in Figure 3.10. Significant performance enhancements in the wave-like nanotube arrays over the single layer and multilayer nanotube arrays were observed at potentials greater than 0.91 V vs. RHE. For all three morphologies, similar photocurrent onset potentials (around 0.4 V vs. RHE) were observed, owing to the similarity in their direct bandgap values.

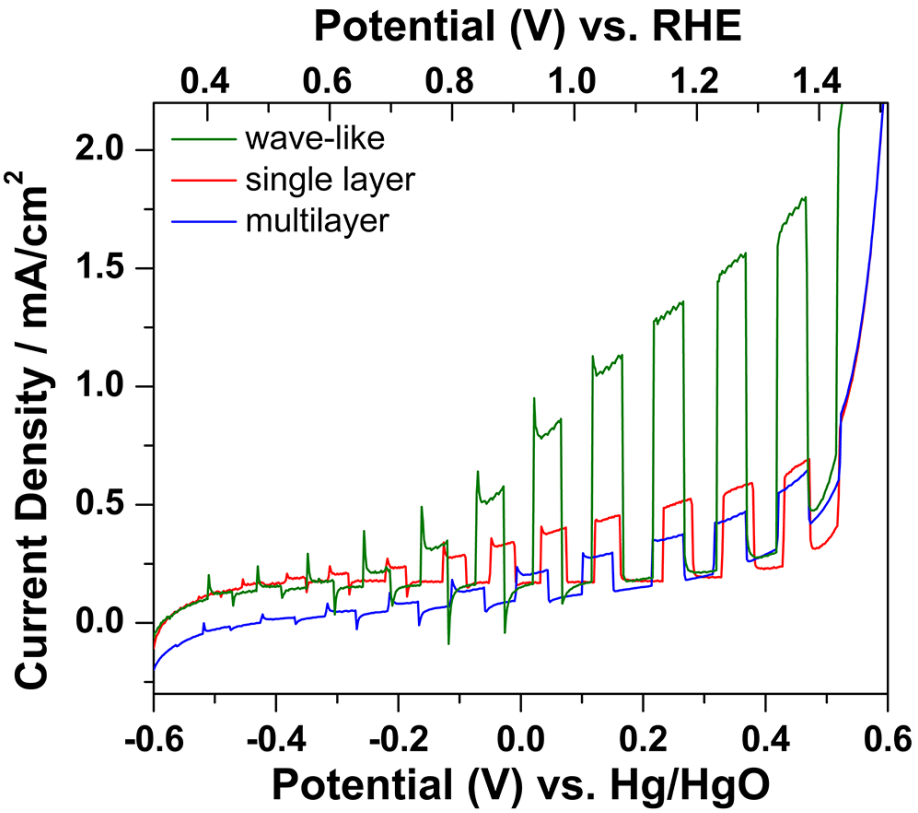

Figure 3.10: LSVs for single layer, multilayer, and wave-like nanotube arrays in 1M KOH.

Chopped light linear sweep voltammetry revealed large transients at low overpotentials for all morphologies, evident in Figure 3.10. Comparison of chopped light LSVs between an electrolyte with and without a hole scavenger allows one to understand the extent of surface recombination. In this work, we employed hydrogen peroxide as the hole scavenger due to its higher rate constants for oxidation as compared to water.

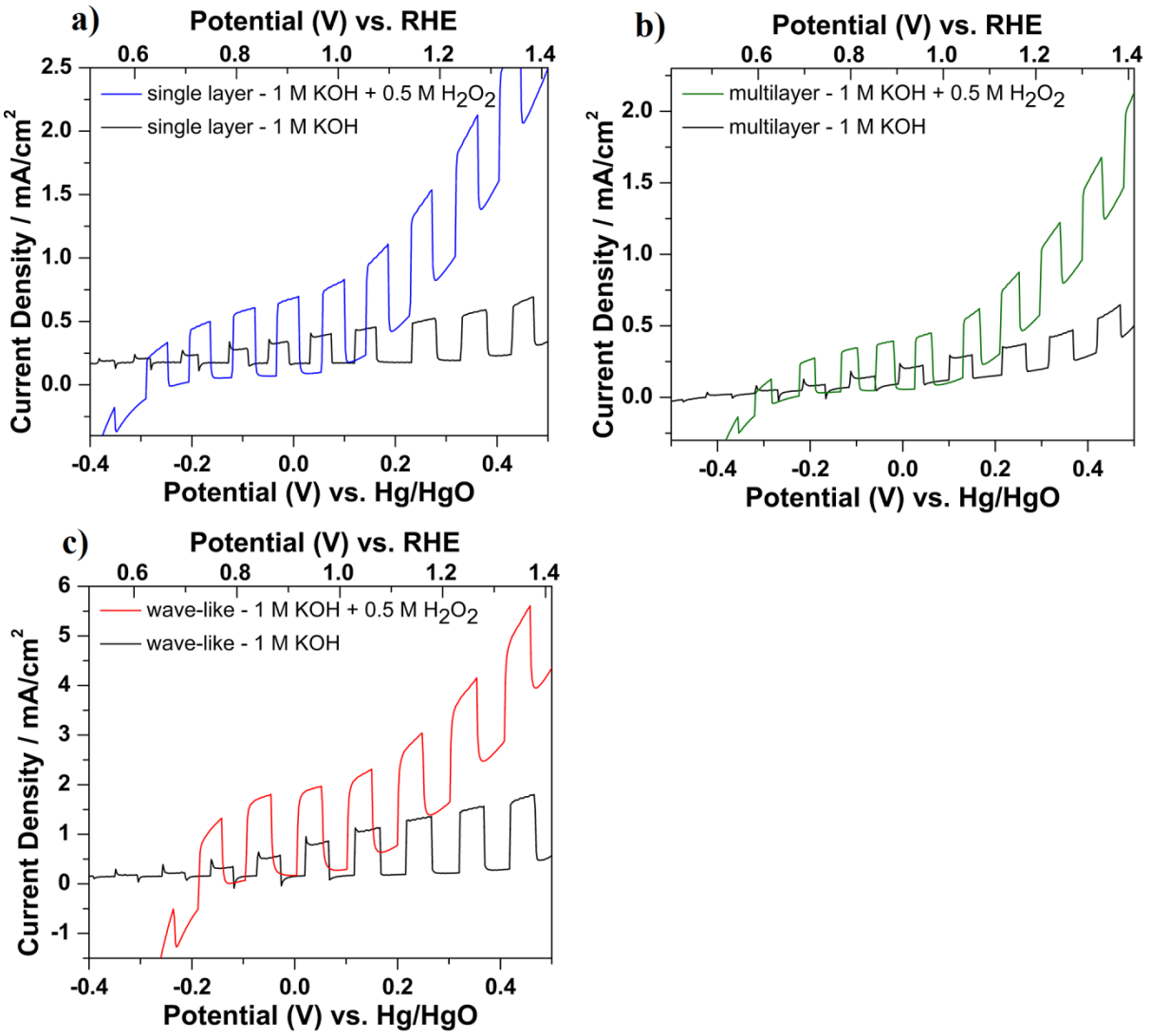

Figure 3.11: LSVs in 1 M KOH + 0.5 M H_2O_2 hole scavenger. Results for a) single layer, b) multilayer, and c) wave-like nanotube arrays.

Figure 3.11 above illustrates chopped light LSVs for the three morphologies. For all of the morphologies, the measurements performed without hydrogen peroxide in the electrolyte show transient photocurrents with no steady Faradaic currents observed until high overpotentials were applied. The positive photocurrent that occurs at low potentials upon turning the light on corresponds to holes accumulating at the electrode/electrolyte interface, without injection into the electrolyte. Upon turning the light off, negative photocurrents are also observed, indicating

that the back reaction of photogenerated electrons to the conduction band occurs with the accumulated holes. The photocurrent transient decreases with increasing overpotential, indicating that the injection barrier does not hinder hole transfer to the electrolyte. This response indicates that surface recombination is suppressed and that the photocurrent is dominated by hole transfer from the bulk. When hydrogen peroxide was added to the electrolyte, the photocurrent transients were suppressed at all potentials, suggesting a complete injection of all photogenerated holes reaching the semiconductor-electrolyte interface into the electrolyte and the suppression of recombination between photogenerated electrons and photo-oxidized species at the semiconductor-electrolyte interface [28]. Similarities in the trends for the measured photocurrents for single layer, multilayer, and wave-like nanotube arrays, both with and without the hole scavenger, suggest that the reason for the differences in the photocatalytic performances across the three morphologies is unlikely to be recombination at the semiconductor-electrolyte interface. And because the optical properties were similar for all the morphologies we studied, we concluded that the reason for variations in the water photo-oxidation efficiency between single layer and multilayer nanotube arrays was the bulk charge transfer properties. Further studies to understand the motion of photogenerated charges in the different hematite nanostructures are discussed below.

We performed electrochemical impedance spectroscopy (EIS) in the dark and under illumination in order to correlate the charge transfer properties of the three nanotube morphologies to the photoelectrochemical performance. Nyquist plots for single layer, multilayer, and wave-like nanotube arrays (shown in Figure 3.12) reveal large charge transfer resistances under dark conditions for all three morphologies. However, upon illumination, all three morphologies showed significantly reduced charge transfer resistances. We attributed the

reduction in charge transfer resistance in the hematite electrodes to photogenerated charge carriers at the semiconductor-electrolyte interface [27, 29]. Typically, larger semiconductor/electrolyte interfacial areas correlate directly with improved hole transport to the interface [27]. Under illumination, single layer, multilayer, and wave-like nanotube arrays had calculated charge transfer resistances of approximately 3,390, 10,900, and 1,920 Ω, respectively. Charge transfer resistances were estimated by electrochemical circuit fitting of the low frequency semi-circle, which represents the semiconductor-electrolyte interface, to a constant phase element in parallel with a resistor (Figure 3.12d) [27, 30]. The smaller semicircle in the Nyquist plots represents the contact resistance between the nanotube arrays and the iron substrates [31]. This resistance was between 500 and 700 Ω for the single layer, multilayer, and wave-like nanotube arrays, suggesting that the nanotube arrays were attached to the substrate in a similar manner. This was expected as all three nanotube array morphologies were synthesized using the electrochemical anodization technique.

As discussed, the surface recombination (from LSV) and optical (and therefore charge separation) properties across the three nanotube array morphologies were similar. This strongly suggests that the higher charge transfer resistance exhibited by the multilayer nanotube arrays under illumination is a result of poor transport of holes to the semiconductor-electrolyte interface due to low charge mobility across layer interfaces. Detailed views of the layer interfaces shown in Figure 2.16 reveal the presence of a discontinuity between adjacent nanotube layers. These discontinuities likely impeded the efficient motion of charges between layers, resulting in high recombination rates and low yields of holes reaching the semiconductor-electrolyte interface as evidenced by the high charge transfer resistance observed in the multilayer nanotube arrays. Indeed, Sargent et al. demonstrated the role of interfaces in limiting the performance of TiO_2-

PbS photovoltaic cells. They observed a two-fold increase in the recombination rates at the TiO_2-PbS interfaces layer interfaces, indicating the deleterious effects of the layer interfaces to cell performance [32]. In the single layer and wave-like nanotube arrays, we attributed the difference in the charge transfer resistances partly to differences in the surface areas of the two morphologies. It is likely that photogenerated charge carrier densities vary across morphologies based on the packing density of hematite.

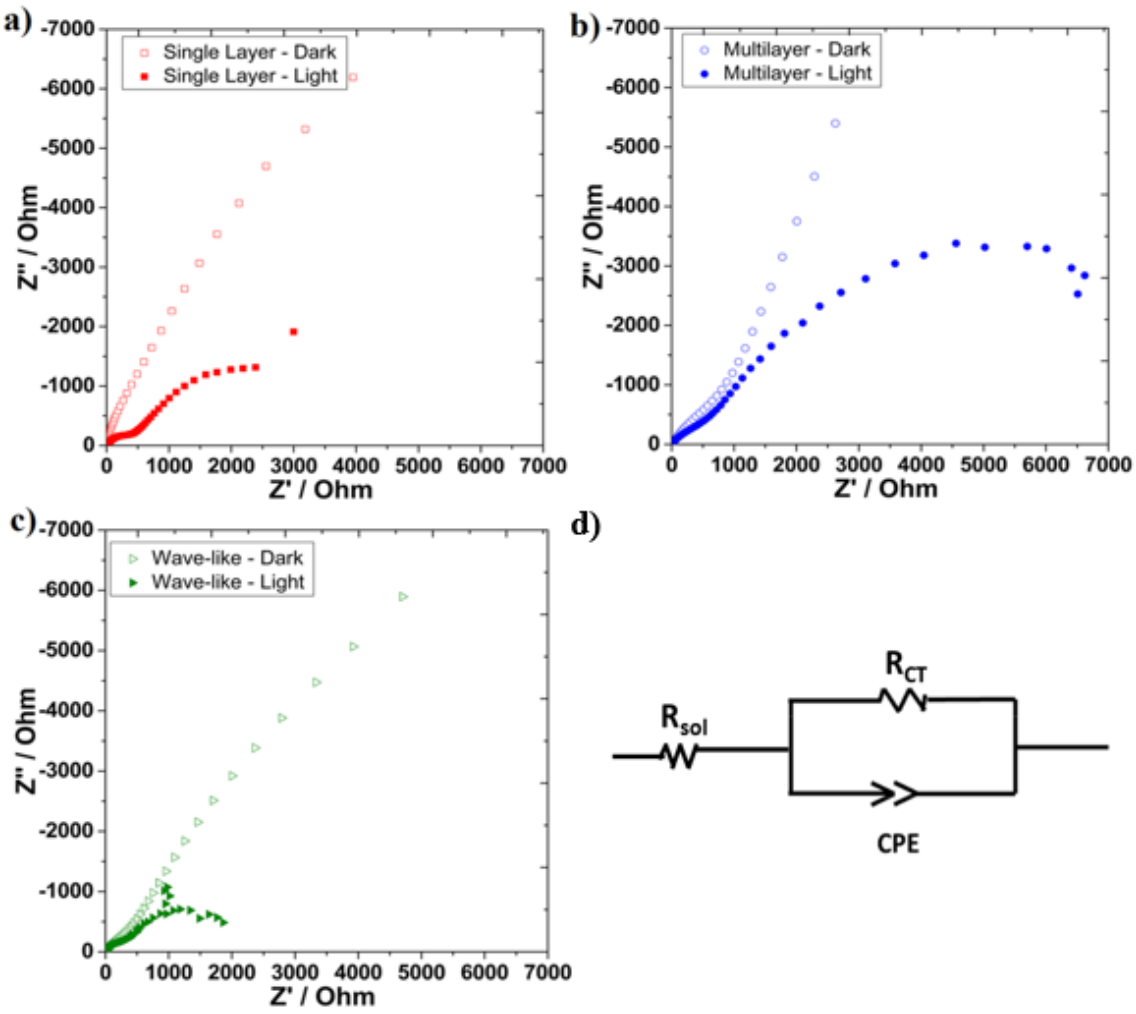

Figure 3.12: Nyquist plots for a) single layer, b) multilayer, and c) wave-like nanotube arrays in 1M KOH under dark and illumination conditions. The equivalent electrochemical circuit for estimating the charge transfer resistances (R_{CT}) from EIS is shown in d). The constant phase element (CPE) is connected in parallel with R_{CT}. R_{sol} represents the solution resistance.

Mott-Schottky analysis is typically used to quantify charge carrier densities in semiconductor materials. Even though the method is only strictly valid for planar electrodes, several researchers have used it for non-planar electrodes, while pointing out the possible pitfalls of such analysis [14]. Applying the analysis here failed to yield meaningful values of charge carrier density and flat band potential for the multilayer and wave-like electrodes, likely due to complications such as extra roughness in wave-like nanotube arrays and the multilayer interfaces [17, 18]. This made it difficult to compare charge carrier density across the morphologies. Figure 3.13 shows a Mott-Schottky plot for single layer nanotube arrays under dark and illumination conditions. The flat band potential for single layer nanotubes was estimated at ~0.5 V *vs.* RHE, consistent with literature reports on hematite [33]. This estimate also corroborates the onset potential observed using LSV (Figure 3.10). Charge carrier densities of 3.4 x 10^{18} /cm^3 and 5.8 x 10^{18} /cm^3 under dark and illumination conditions, respectively, were determined from Mott-Schottky analysis, showing a slight increase in the number density of charge due to charge photogeneration under illumination. The increase was surprisingly small, and this might be due to artifacts resulting from applying the Mott-Schottky analysis to nanostructured samples. For instance, Wang et al. previously applied this type of analysis to nanonet-based hematite nanostructures and reported failing to obtain meaningful results due to the non-planar nature of the semiconductor-electrolyte interfaces [14].

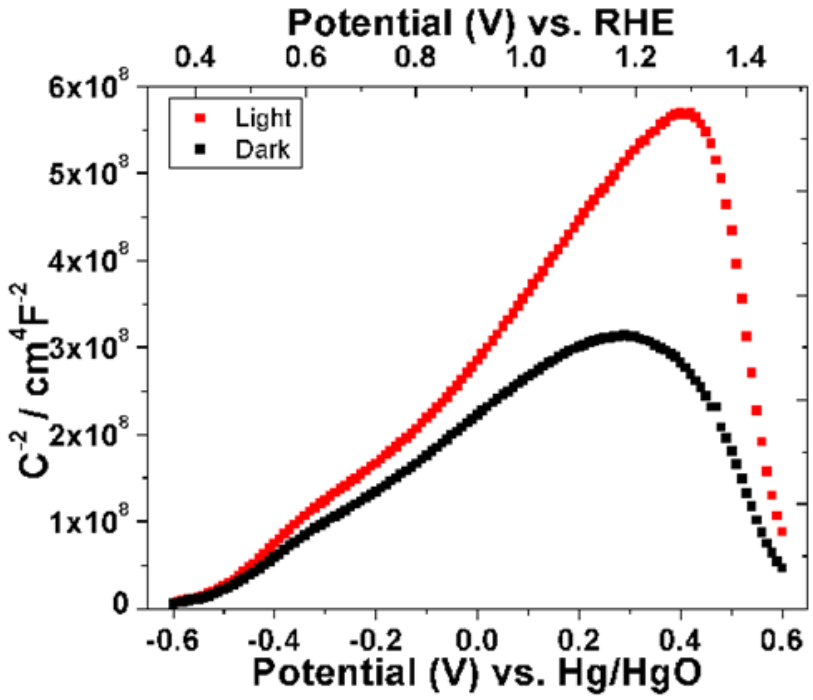

Figure 3.13: Mott-Schottky plot for single layer nanotube arrays under dark and illumination conditions. A flat band potential of ~0.5 V *vs.* RHE was determined.

Combining the electrochemical surface area, photocurrent density, IPCE, and impedance results, we concluded that the relatively lower photocurrents observed for the multilayer morphology were a result of poor charge mobility across layer interfaces, while differences in the performance between single layer and wave-like nanotube arrays were partly a result of differences in the active electrochemical surface area.

3.3.4 Variation of Photocatalytic Performance with Nanotube Diameter

For single layer nanotube arrays, a reduction in diameter caused an increase in the measured photocurrent, as shown in Figure 3.14. We hypothesized that reducing nanotube diameter enabled an increase in the nanotube packing density, allowing for an increase in the electrochemical surface area. However, only small changes in the measured electrochemical surface areas were observed, suggesting that differences in the photocatalytic performance might have been due to an increased photogenerated charge carrier density as a result of an increase in

the photoactive mass for nanotube arrays with smaller diameters. Charge carrier photogeneration, as determined by Mott-Schottky analysis, yielded similar results for nanotube arrays of different diameters. However, this experimental technique was developed for smooth, planar electrodes and can give unreliable data for complex nanostructures such as nanotubes [14, 18]. This made a complete understanding of the effect of varying the diameter of the nanotube arrays on the performance difficult.

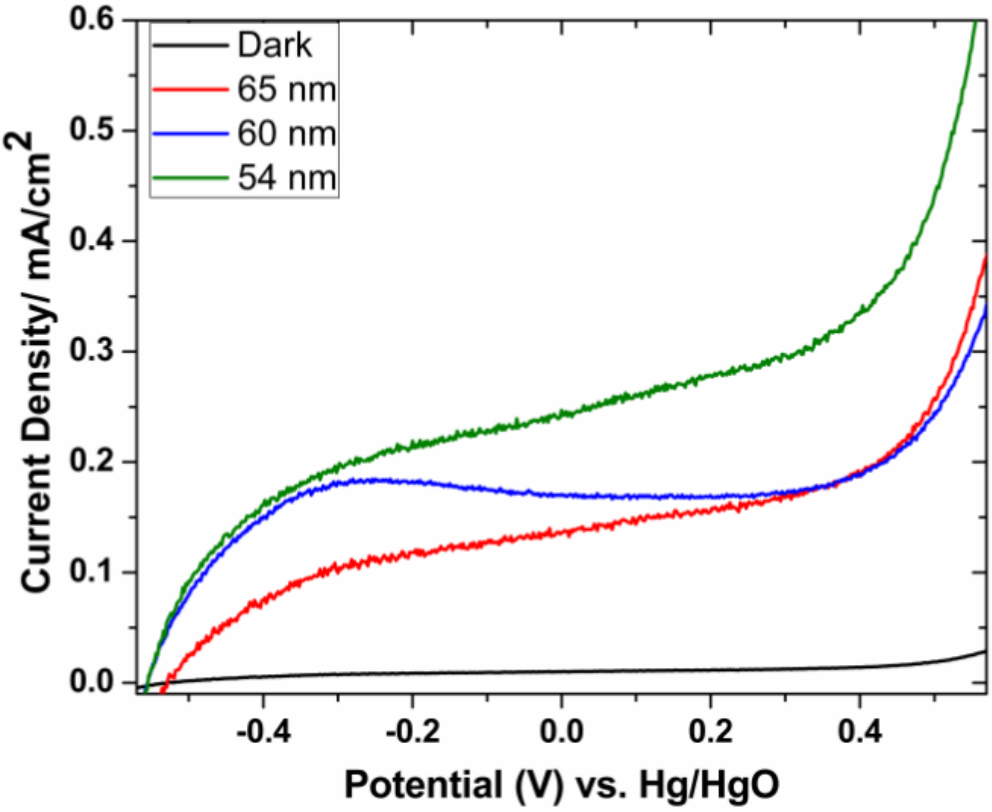

Figure 3.14: LSV showing variations in photocatalytic performance with nanotube diameter.

3.3.5 Variation of Photocatalytic Performance with Number of Nanotube Layers

Results from LSV (Figure 3.15) revealed that within the multilayer nanotube morphology, an increase in the number of layers resulted in a corresponding increase in the photocatalytic performance up to five layers, likely due to an increase in the photogenerated charge carrier density as a result of scattering effects at layer interfaces. Beyond five layers, a

reduction in the photocatalytic performance was observed, likely due to increased recombination rates at layer interfaces. However, due to the poor photocatalytic performance of multilayer nanotube arrays when compared to single layer and wave-like nanotube arrays, as well as difficulties in obtaining meaning data for charge carrier photogeneration, no further detailed experiments were carried out to ascertain the reasons for the observed trends.

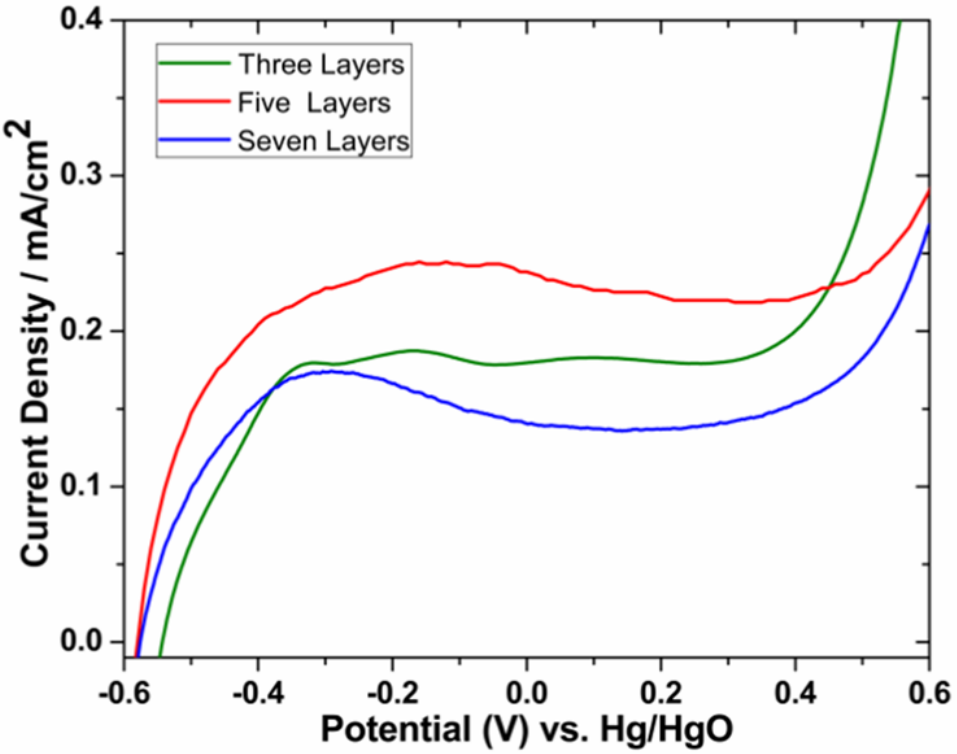

Figure 3.15: LSVs for nanotube arrays composed of three, five, and seven layers. Increased photocatalytic performance was achieved up to five layers.

3.3.6 Effect of Iron-Foil Purity on Nanotube Morphology and Photocatalytic Performance

Schmuki et al. recently reported that iron foil purity has a significant effect on nanotube array growth as well as the photocatalytic performance of the resulting nanotubes [29]. They observed a nine-fold increase in the measured photocurrent, from 0.028 to 0.25 mA/cm^2 at 1.4 V *vs.* RHE for hematite nanotubes synthesized from 99.5% pure iron foils compared to those synthesized from 99.99% pure foils. They also noted a reduction in the nanotube growth rate for

the lower purity foil, which they attributed to the high content of manganese (5000 ppm) in these foils. They concluded that the high manganese content led to the selective dissolution of manganese in the oxide layers of the materials, causing the dissolution of nanotube walls and poor nanotube wall structure definition. High purity iron foils (99.99%) contained only 2.7 ppm manganese, leading to nanotubes with well-defined walls and higher photocatalytic activity.

Contrary to Schmuki's findings, our study with hematite nanotubes, under the synthesis conditions used, revealed no observable effects of iron foil purity on the nanotube morphology. Similar growth conditions for 99.5% and 99.99% pure iron foils resulted in similar nanotube lengths and thicknesses, as highlighted in Table 3.2 for single layer nanotubes grown at a holding voltage of 40 V for 10 min. This discrepancy in results might be explained by the fact that Schmuki et al. used a concentration of 0.14 M ammonium fluoride and a temperature of 60 °C [29] for their anodization electrolyte, as compared to 0.1 M ammonium fluoride at 23 °C in our case. We attempted to replicate Schmuki's synthesis condition of 60 °C, but this resulted in the dissolution of the nanotube arrays.

Table 3.2: Effect of iron foil purity on single layer nanotube growth. Only small changes resulted from the changes in foil purity, contrary to the findings of Schmuki et al. [29].

Foil Purity (%)	Thickness (μm)	Outer Diameter (nm)
99.5	3.5	60
99.99	3.1	62

However, foil purity played a significant role in our study with regards to photocatalytic performance. Figure 3.16 shows IPCE measurements for single layer, multilayer, and wave-like nanotube arrays made from 99.5% pure iron foils. Due to the presence of magnetite in the nanotube samples, there was an absorption tail in the absorption of the samples, leading to a low residual photocatalytic activity beyond 590 nm. The electrochemical surface areas for the single

layer, multilayer, and wave-like nanotube samples are shown in Table 3.3 and were comparable to those for nanotubes synthesized from higher purity foils. As seen with nanotubes synthesized from higher purity foils, surface area played a significant role in improving the photocatalytic performance of wave-like nanotube arrays as compared to single layer nanotube arrays. Moreover, as with the case of nanotube arrays fabricated from higher purity foils, multilayer nanotube arrays exhibited the lowest photocatalytic performance. For all cases, nanotube array samples made from lower purity foils exhibited photoconversion efficiencies that were an order of magnitude lower than those for samples made from higher purity foils. Due to this trend in performance across morphologies for nanotube arrays synthesized from high and low purity foils, we conclude that low foil purity is detrimental to photocatalytic performance, in agreement with Schmuki's findings.

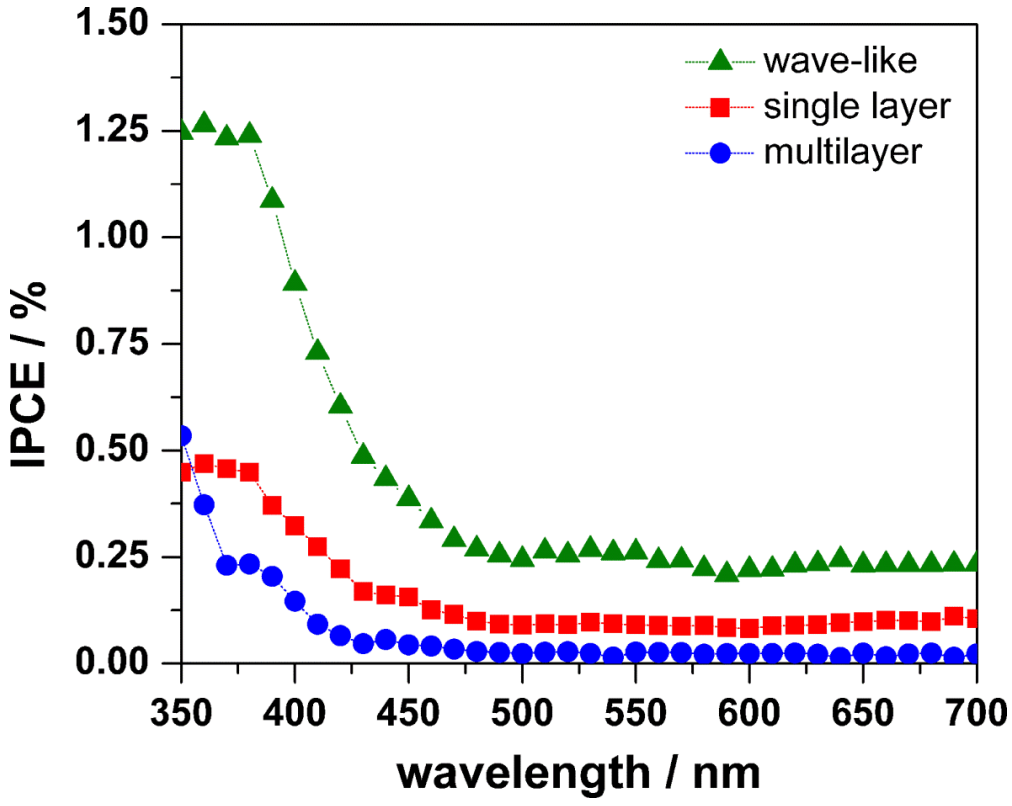

Figure 3.16: IPCE for single layer, multilayer, and wave-like nanotube arrays (synthesized from 99.5% pure iron foils) at 0.4 V vs. Hg/HgO in 1M KOH.

Table 3.3: Properties of the single layer, multilayer, and wave-like nanotube arrays synthesized with 99.5% pure iron foil.

	Percent Hematite	Electrochemical Surface Area (cm^2)	IPCE at λ=380nm (%)
Single layer	39.3	9.8	0.45
Multilayer	34.1	6.1	0.23
Wave-like	36.7	19	1.24

3.4 Summary and Conclusions

Single layer, multilayer, and wave-like hematite nanotube arrays were synthesized, and their optical and photoelectrochemical properties for water oxidation were determined. Optical properties were found to be similar across the single layer, multilayer, and wave-like nanotube array morphologies. The nanotube morphologies played critical roles in the

photoelectrochemical performance. Among the morphologies studied in this work, the wave-like nanotube morphology exhibited the highest photoconversion efficiency (IPCE), partly due to increased electrochemical surface area. Applying Mott-Schottky analysis failed to yield meaningful data to compare charge carrier densities and flat band potentials for the single layer, multilayer, and wave-like nanotube arrays, likely due to complications such as extra roughness in wave-like nanotube arrays, and the multilayer interfaces [18]. The multilayer nanotube arrays exhibited the lowest IPCE, due to reduced charge mobility across layer interfaces. In addition, the effect of the iron foil purity on the performance of the hematite nanotube arrays was studied. Nanotube arrays synthesized from higher purity foils exhibited a significantly higher (one order of magnitude) photocatalytic performance. It was found that manganese impurities were detrimental to the photocatalytic performance [29]. Control of the morphology of the various nanostructures and developing structure-function relations could allow the engineering of nanoscale devices with superior performance.

3.5 References

[1] Wheeler, D. A.; Wang, G.; Ling, Y.; Li, Y.; Zhang, J. Z. Nanostructured Hematite: Synthesis, Characterization, Charge Carrier Dynamics, and Photoelectrochemical Properties. *Energy Environ. Sci.* **2012**, *5*, 6682.

[2] Roy, P.; Berger, S.; Schmuki, P. Titania Nanotubes: Synthesis and Applications. *Angew. Chem., Int. Ed.* **2011**, *50*, 2904.

[3] Sun, J.; Zhong, D. K.; Gamelin, D. R. Composite Photoanodes for Photoelectrochemical Solar Water Splitting. *Energy Environ. Sci.* **2010**, 3, 1252.

[4] Sivula, K.; Le Formal, F.; Gratzel, M. Solar Water Splitting: Progress Using Hematite (α-Fe_2O_3) Photoelectrodes. *ChemSusChem*. **2011**, *4*, 432.

[5] Roy, P.; Berger, S.; Schmuki, P. Titania Nanotubes: Synthesis and Applications. *Angew. Chem., Int. Ed*. **2011**, *50*, 2904.

[6] Yu, H.; Bai, Y.; Zong, X.; Tang, F.; Lu, G. Q.; Wang, L. Cubic CeO_2 Nanoparticles as Mirror-like Scattering Layers for Efficient Light Harvesting in Dye-sensitized Solar Cells. *Chem. Commun.* **2012**, *48*, 7386.

[7] Ozkar, S. Enhancement of Catalytic Activity by Increasing Surface Area in Heterogeneous Catalysis. *Appl. Surf. Sci.* **2009**, *256*, 1272.

[8] Trasatti, S.; Petrii, O. A., Real Surface Area Measurements in Electrochemistry. *J. Electroanal. Chem.* **1992**, *327*, 353.

[9] Abdi, A.; Trari, M. Investigation on Photoelectrochemical and Pseudocapacitance Properties of Non-stoichiometric Hematite Elaborated by Sol-gel. *Electrochim. Acta* **2013**, *111*, 869.

[10] Liu, Y.; Zhou, J.; Gong, J.; Wu, W-P.; Bao, N.; Pan, Z-Q.; Gu, H-Y. The Investigation of Electrochemical Properties for Fe_3O_4/Pt Nanocomposites and Enhancement Sensing for Nitrite, *Electrochim. Acta* **2013**, *111*, 876.

[11] Anwar, M.; Hogarth, C. A.; Optical Properties of Amorphous Thin Films of MoO_3 Deposited by Vacuum Evaporation. *Phys. Status Solidi*. **1988**, *109*, 469.

[12] Fondell, M.; Jacobson, T. J.; Boman, M.; Edvinsson, T. Optical Quantum Confinement in Low Dimensional Hematite. *J. Mater. Chem. A.* **2014**, *2*, 3352.

[13] LaTempa, T. J.; Feng, X.; Paulose, M.; Grimes, C.A. Temperature-Dependent Growth of Self-Assembled Hematite Nanotube Arrays: Rapid Electrochemical Synthesis and Photoelectrochemical Properties. *J. Phys. Chem.C*. **2009**, *36*, 16293.

[14] Lin, Y.; Zhou, S.; Sheehan, S. W.; Wang, D. Nanonet-Based Hematite Heteronanostructures for Efficient Water Splitting. *J. Am. Chem. Soc*. **2011**, *133*, 2398.

[15] Huang, Z.; Lin, Y.; Xiang, X.; Rodríguez-Córdoba, W.; McDonald, K. J.; Hagen, . S.; Choi, K-S.; Brunschwig, B. S.; Musaev, D. G.; Hill, C. L.; Wang, D.; Lian, T. In Situ Probe of Photocarrier Dynamics in Water-Splitting Hematite Electrodes, *Energy Environ. Sci.* **2012**, *5*, 8923.

[16] Bard, A. J.; Faulkner, L. R. Electrochemical Methods: Fundamentals and Applications, 2nd Ed., *Wiley*. **2004**, 226-230.

[17] Gelderman, K.; Lee, L.; Donne, S. W. Flat-Band Potential of a Semiconductor: Using the Mott–Schottky Equation. *J. Chem. Educ.* **2007**, *84*, 685.

[18] Cardon, F.; Gomes, W. P. On the Determination of the Flat-band Potential of a Semiconductor in Contact With a Metal or an Electrolyte From the Mott-Schottky Plot. *J. Phys. D: Appl. Phys.* **1978**, *11*, L63.

[19] Beermann, N.; Vayssieres, L.; Lindquist, S.-E.; Hagfeldt, A. Photoelectrochemical Studies of Oriented Nanorod Thin Films of Hematite. *J. Electrochem. Soc*. **2000**, *147*, 2456.
[20] Souza, F. L.; Lopes, K. P.; Longo, E.; Leite, E. R. The Influence of the Film Thickness of Nanostructured α-Fe_2O_3 on Water Photooxidation. *Phys. Chem. Chem. Phys*. **2009**, *11*, 1215.
[21] Abdi, A.; Trari, M. Investigation on Photoelectrochemical and Pseudocapacitance Properties of Non-stoichiometric Hematite Elaborated by Sol−Gel. *Electrochim. Acta* **2013**, *111*, 869.
[22] Sivula, K.; Zboril, R.; Le Formal, F.; Robert, R; Weidenkaff, A.; Tucek, J.; Frydrych, J.; Gratzel, M. Photoelectrochemical Water Splitting with Mesoporous Hematite Prepared by a Solution-Based Colloidal Approach. *J. Am. Chem. Soc*. **2010**, *132*, 7436.
[23] Wang, Y.; Herron, N. Nanometer-Sized Semiconductor Clusters: Materials Synthesis, Quantum Size Effects, and Photophysical Properties. *J. Phys. Chem.* **1991**, *95*, 525.
[24] Lu, Y.; Rongsheng, C.; Joon, I. J.; Wenhui, Z.; Chao, W.; Yiqian, W.; Guangwen, Z. Morphological Transformation of Hematite Nanostructures during Oxidation of Iron. *Nanoscale* **2013**, *5*, 7581.
[25] Sherif, E. M.; Abdo, H. S.; Khalil, A. K.; Nabawy, A. M. Corrosion Properties in Sodium Chloride Solutions of Al-TiC Composites in situ Synthesized by HFlHF. *Metals* **2015**, *5*, 1799.
[26] Wang, H.; Turner, J. A. Characterization of Hematite Thin Films for Photoelectrochemical Water Splitting in a Dual Photoelectrode Device. *J. Electrochem. Soc.* **2010**, *157*, F173.
[27] Jun, H.; Im, B.; Kim, J. Y.; Im, Y-O.; Jang, J-W.; Kim, E. S.; Kim, J. Y.; Kang, H. J.; Hong, S. J.; Kim, J. Y.; Photoelectrochemical Water Splitting Over Ordered Honeycomb Hematite Electrodes Stabilized by Alumina Shielding, *Energy Environ. Sci.* **2012**, *5*, 6375.
[28] Dotan, H.; Sivula, K.; Gratzel, M.; Rothschild, A.; Warren, S. C. Probing the Photoelectrochemical Properties of Hematite (α-Fe_2O_3) Electrodes using Hydrogen Peroxide as a Hole Scavenger. *Energy Environ. Sci*. **2011**, *4*, 958.
[29] Lee, C-Y.; Wang, L.; Kado, Y.; Killian, M. S; Schmuki, P. Anodic Nanotubular/porous Hematite Photoanode for Solar Water Splitting: Substantial Effect of Iron Substrate Purity, *ChemSusChem*. **2014**, *7*, 934.
[30] Kim, J. Y.; Magesh, G.; Youn, D. H.; Jang, J.-W.; Kubota, J.; Domen, K.; Lee, J. S. Single-crystalline, Wormlike Hematite Photoanodes for Efficient Solar Water Splitting. *Sci Rep.* **2013**, 3, 2681.
[31] Qu, Y.; Baumann, T. F.; Santiago, J. G.; Stadermann, M. Characterization of Resistances of a Capacitive Deionization System. *Environ. Sci. Technol.* **2015**, *49*, 9699.
[32] Kemp, K. W.; Labelle, A. J.; Thon, S. M.; Ip, A. H.; Kramer, I. J.; Hoogland, S.; Sargent, E. H. Interface Recombination in Depleted Heterojunction Photovoltaics based on Colloidal Quantum Dots. *Adv. Energy Mater.* **2013**, *3*, 917.
[33] Mohapatra, S. K.; John, S. E.; Banerjee, S.; Misra, M. Water Photooxidation by Smooth and Ultrathin α-Fe_2O_3 Nanotube Arrays. *Chem. Mater*. **2009**, *21*, 3048.

Chapter 4

Electrochemical Storage through Li^+ Ion Intercalation in Nb_2O_5

4.1 Introduction

In Chapter Two, we demonstrated a remarkable level of control over the synthesis of various iron oxide nanostructures. Synthesis was carried out via the electrochemical anodization of iron foils in electrolytic solutions containing ammonium fluoride. In this chapter, we apply the experience gained in the synthesis of iron oxide nanotube arrays described in Chapter Two to develop nanostructured architectures based on niobium for applications in electrochemical energy storage.

Nanostructure control presents new opportunities for designing high performance secondary Li^+ ion storage materials. The enhanced electrochemical performance exhibited by nanostructured materials over their bulk analogues has been attributed to more efficient charge transport kinetics (due to shortened ion diffusion path lengths and one-dimensional electron transport at the nanoscale) [1-2]. The phrase 'one-dimensional' is being applied to the transport of electrons through the nanostructure (for instance, through nanotubes) unless otherwise stated. Cao et al. explored the use of V_2O_5 electrodes, including planar, nanorod, nanocable, and nanotube morphologies, for applications in electrochemical energy storage. They found the electrochemical behavior of V_2O_5 to be a strong function of the morphology, with the planar electrodes showing the poorest specific energies and powers due to poor ion transport properties [3]. While much progress has been made towards the development of nanostructured secondary

storage materials, many fundamental questions towards developing an understanding of how the properties of nanoscale storage materials differ from those of bulk materials and how such an understanding could be applied to optimize electrochemical performance still remain unanswered. For instance, there is debate in the scientific community over why the electrochemical changes observed from bulk to nanostructured $LiFePO_4$, a material that allows one-dimensional Li^+ ion diffusion, is fundamentally different from those in nanostructured materials that allow transport in two or three dimensions such as $LiCoO_2$ and Li_2MnSiO_4 [4-5]. Moreover, it has long been believed that improvements in the electrochemical performance of $LiFePO_4$ at the nanoscale were a result of an increased accessibility of the low-energy (010) crystallographic planes that favor Li^+ ion diffusion [6-7]. However, new evidence has recently surfaced indicating that amorphous nano-$LiFePO_4$ electrodes exhibit excellent Li^+ ion intercalation kinetics and rate capabilities [8-10], contradicting the former belief. Therefore, further investigations are needed to gain a full understanding of the effects of nanostructuring in electrochemical energy storage materials.

Traditional battery applications include portable electronics such as cell phones, laptops, and camcorders [11]. Over the last several years, new applications that demand high power and energy densities, such as hybrid electric vehicles, have emerged. This has brought about the need to identify materials that exhibit both high charge storage capacities and high rate capabilities. Niobium pentoxide (Nb_2O_5) has been identified as a potential candidate for a battery material satisfying both performance criteria [11-12]. Several polymorphs of Nb_2O_5 are currently known to exist. Among these, the orthorhombic phase (T-) has been demonstrated to exhibit the lowest Li^+ ion intercalation energy and the highest capacity [12]. Moreover, high rate capabilities were demonstrated in both thin (< 100 nm) and thick (~40 μm) film T-Nb_2O_5 electrodes, with high

capacities of ~130 mAh/g at a discharge rate of 10C and only a small drop to ~110 mAh/g at 100C when mixed with carbon black [12]. (The discharge rate represents the total time it takes to fully discharge the electrode; for instance, a rate of *n*C indicates that it takes 1/*n* hours to fully discharge the electrode.) These charge capacities are typical of battery materials, and the power densities are close to those of supercapacitors, making T-Nb_2O_5 an attractive material for high-energy and high-power applications.

Dunn et al. demonstrated two-dimensional Li^+ ion intercalation in T-Nb_2O_5 through (180) planes [12]. These planes represent the lowest energy barrier planes in the crystal and are therefore most favorable for the high rate intercalation of Li^+ ions [5]. Figure 4.1 shows a schematic representation of the T-Nb_2O_5 unit cell, with the parallel planes showing the (180) planes.

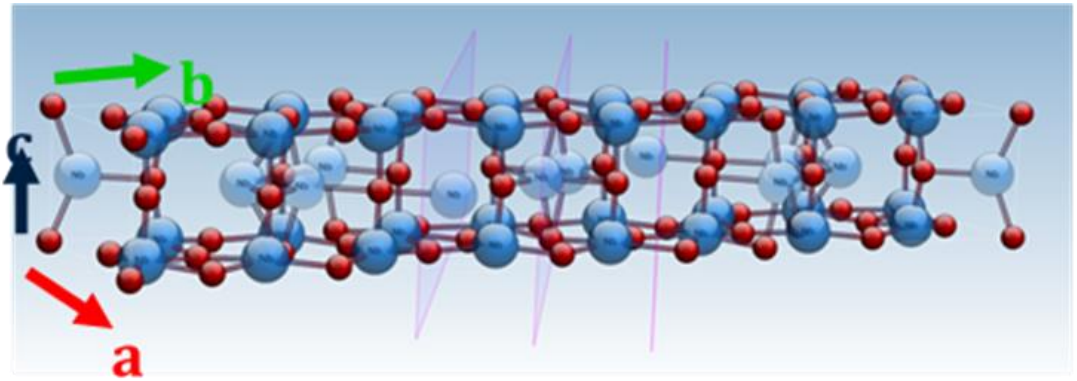

Figure 4.1: The unit cell of T-Nb_2O_5 showing the arrangement of oxygen (red) and niobium (blue) ions in the crystal. Li^+ intercalation proceeds via the low-energy (180) planes.

Nanostructured T-Nb_2O_5 geometries such as nanotube arrays hold the promise of higher electrochemical surface areas and therefore higher exposure of low energy intercalation planes, resulting in increased ion intercalation rates and enhanced capacities. Nanotube arrays are one-dimensional, forcing electron transport to proceed in one-dimension. Ion transport distances are

also reduced, meaning higher rates of charge insertion and extraction from the electrodes [1, 13]. Low-dimensional structures have also been reported to better withstand stress accumulation from volume changes due to ion intercalation in lithium ion batteries, giving them longer cycle life [13, 14].

In this chapter, we sought to understand the effect of nanostructure on the Li^+ ion intercalation behavior of T-Nb_2O_5, and investigate the feasibility of its application in high-rate secondary charge storage devices. Nb_2O_5 electrodes were synthesized via the electrochemical anodization of niobium foils in an electrolytic solution containing ammonium fluoride. By varying the synthesis conditions, electrodes with nanotube array and planar morphologies were achieved (Figure 4.2). We identified key nanostructural properties of the T-Nb_2O_5 electrodes and correlated them to various electrochemical performance metrics. Materials properties that were investigated included the crystallographic phase, electrochemical surface area, and diffusion distance. Electrochemical performance metrics included the Li^+ ion intercalation kinetics, rate capability, and total Li^+ capacity.

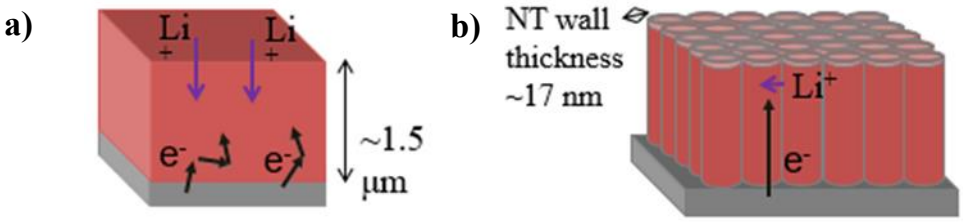

Figure 4.2: Morphologies of Nb_2O_5 synthesized and studied in this chapter. a) Planar electrodes result in tortuous electron transport pathways as opposed to one-dimensional electron pathways in b) nanotube array electrodes. Nanotubes also significantly shorten ion diffusion pathways.

4.2 Experimental Method

4.2.1 Materials

Niobium foil substrates (99.99%, 0.25 mm thick) were purchased from Alfa Aesar. Chemicals for production of the anodization electrolytes, ammonium fluoride (98.5%) and glycerol (laboratory grade, < 0.2 wt% water) were purchased from Fisher Chemical. Ultrapure water (resistance 18.2 MΩ) was obtained from a Millipore Milli-Q water purification system. Chemicals for production of electrolytes for electrochemical performance evaluation, bis-trifluoromethane sulfonamide lithium salt (LiTFSI), lithium foils, and propylene carbonate (PC) were purchased from Sigma-Aldrich.

4.2.2 Nanotube Array and Planar Electrode Synthesis

The Nb_2O_5 electrodes were synthesized via electrochemical anodization. A two-electrode cell was constructed using a niobium foil substrate (0.25 mm, 1.70 cm^2) as the anode and a platinum foil (2.50 cm^2) as the cathode. The electrodes were set 2 cm apart and an Agilent 3674 power supply was used to apply a voltage across the electrochemical cell. A customized MATLAB software routine was used to control the power supply, apply the voltage across the cell, and record the corresponding current response during the anodization experiment. To check whether there were no significant voltage drops across the internal resistances of the power supply and that of the anodization cell, we measured the voltage across the electrochemical anodization setup. Measured voltage profiles matched the input voltage profiles, indicating that the voltage drops across the internal resistances of the cell and the power supply were negligible. The voltages presented in this dissertation were the measured voltages. All experiments were carried out at room temperature and pressure. The electrochemical anodization cell for the synthesis of the Nb_2O_5 electrodes is shown in Figure 2.2 of Chapter Two of this dissertation.

Electrolytic solutions composed of 0.2 and 0.6 M ammonium fluoride in glycerol were used to synthesize the planar and nanotube array electrodes, respectively. A higher fluoride concentration was used for the synthesis of nanotubes to aid in the oxide dissolution process and increase the rate of nanotube array formation [15]. During the synthesis of nanotube arrays, the voltage was increased from 0 to a holding voltage of 30 V at a rate of 5 V/s. The holding voltage was then maintained for 2 h. A typical voltage input and current response for Nb_2O_5 nanotube array synthesis is shown in Figure 4.3. The synthesis of planar electrodes was carried out at 20 V for 0.5 h. The conditions used for planar electrode synthesis were not sufficient for the chemical dissolution of the Nb_2O_5 films. The various stages of planar and nanotube array formation were discussed in Chapter Two of this dissertation. After anodization, the planar and nanotube array electrode samples were rinsed with ethanol to remove electrolyte remnants from the surface of the film. The samples were then dried in a vacuum oven at 80 °C for 30 minutes.

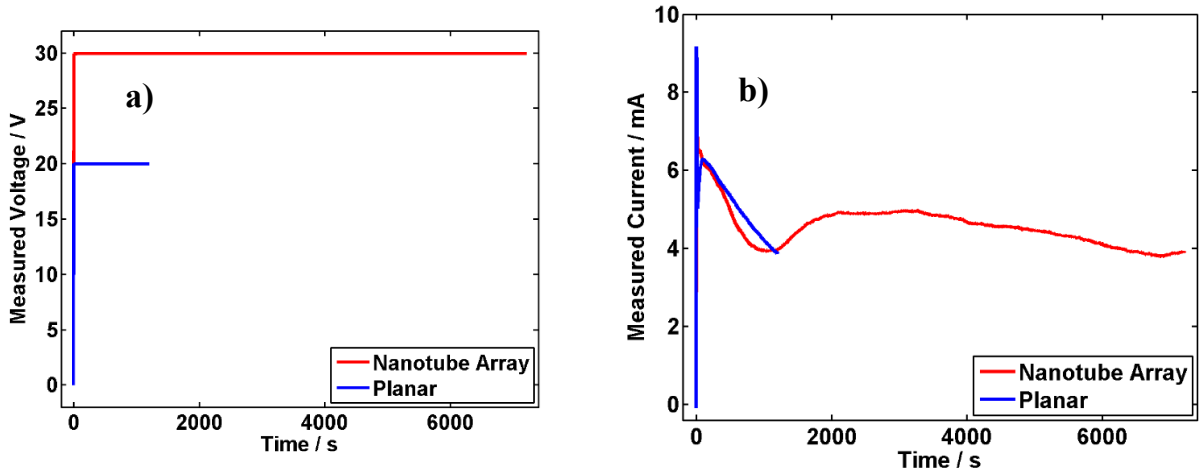

Figure 4.3: a) Measured voltage input and b) current response for planar and nanotube array Nb_2O_5 synthesis. Planar electrodes were synthesized at 20 V in an electrolyte with a 0.2 M F^- ion concentration. Conditions for planar electrode synthesis were not sufficient for the chemical dissolution of the Nb_2O_5 film. Nanotube array electrodes were synthesized at 30 V in an electrolyte with a 0.3 M F^- ion concentration.

4.2.3 Characterization of Bulk and Surface

Bulk characterization of the materials was performed using X-ray diffraction (XRD), as detailed in the experimental section of Chapter Two. Ex-situ XRD was used to investigate the structural changes of the electrodes during electrochemical cycling, including the volume changes.

The nanotube array and planar electrode surface and cross-sectional morphologies were imaged using a FEI Nova 200 Nanolab field emission scanning electron microscope (SEM). The SEM micrographs were used to determine the dimensions of the nanotube arrays and the planar electrodes.

4.2.4 Electrochemical Characterization

Cyclic Voltammetry (CV) was performed to investigate the electrochemical behavior of the Nb_2O_5 electrodes. CV was carried out in an El-cell with an Nb_2O_5 working electrode, a Li metal foil counter and reference, a 1.55 mm thick glass fiber separator, and a 0.5 M LiTFSI/PC electrolyte. CV was performed between 0.1 and 3.4 V *vs.* Li/Li^+ using a PGSTAT302N Autolab potentiostat. Measured currents were normalized by the mass of the electroactive material, Nb_2O_5. The measurement of peak currents in CV is imprecise because of uncertainties in the correction for polarization currents. Consequently, the CV technique is not ideal for the quantitative determination of system properties that are derived from peak heights, such as the rate constant of a reaction. Therefore, the technique is typically used alongside other methods that are better suited for the quantitative evaluation of electrochemical behavior, such as charge/discharge and electrochemical impedance measurements [16]. The CV technique is usually ideal for solution-based systems but has been extensively applied to probe the electrochemical behavior of thin-film and nanostructured intercalation electrodes as well [17].

The method has been widely demonstrated to be reliable for the qualitative evaluation of electrodes of thickness ranging from a few microns to as much as 20 μm thick [12, 18]. Moreover, CV is useful for a qualitative interpretation of trends in the electrochemical behavior of electrodes of the same thickness and chemical compositions but different morphologies [3]. Electrodes synthesized in this work were ≤ 1.5 μm thick, allowing CV to be a powerful tool for studying the intercalation dynamics in the Nb_2O_5 electrodes. Cell assembly and CV measurements were carried out in an argon-filled glovebox with oxygen and water levels ≤ 1 ppm.

Charge/Discharge (C/D) experiments to investigate the rate performances of the electrodes were carried out using the same electrode set-up as CV experiments, using a Maccor Series 4000 battery tester. All experiments were conducted at constant current (galvanostatic) unless otherwise explicitly stated. Inductively Coupled Plasma (ICP) spectroscopy measurements to determine the total capacity of the discharged materials were done at Galbraith Laboratories, Inc.

Electrochemical Impedance Spectroscopy (EIS) was utilized to measure the charge transfer kinetics of the Nb_2O_5 electrodes, and was performed in the frequency range from 100 kHz to 0.1 Hz at various potentials ranging from 0.1 to 3.4 V *vs.* Li/Li^+ and a voltage signal with an amplitude of 10 mV.

4.3 Results and Discussion

4.3.1 Nanotube Array and Planar Electrode Synthesis

Varying the conditions during electrochemical anodization enabled the synthesis of nanotube array and planar electrode morphologies with controlled dimensions. Representative

SEM images of the surface and cross-sectional morphologies for the electrodes are shown in Figure 4.4. The film thicknesses of the planar and nanotube array morphologies were ~1 µm. The nanotube arrays had approximately circular cross-sections and a nanotube wall thickness of ~17 nm. The effect of electrode dimensions on the electrochemical performance is discussed below.

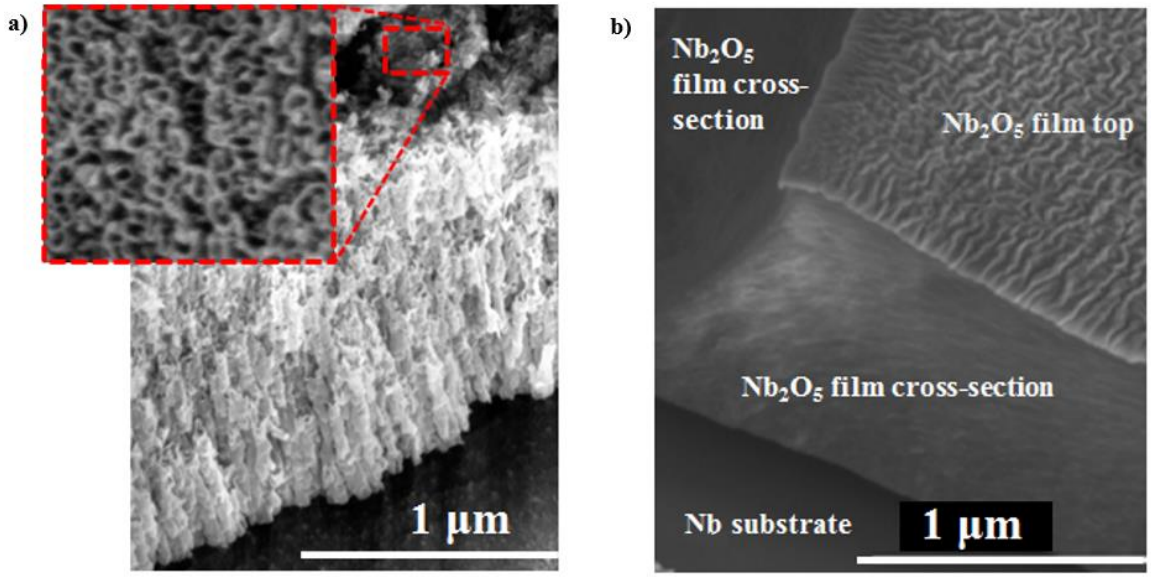

Figure 4.4: Representative SEM images of a) Nb_2O_5 nanotube arrays and b), planar electrodes.

4.3.2 Bulk Characterization

XRD patterns for the as-synthesized and calcined nanotube-array Nb_2O_5 electrode samples are shown in Figure 4.5. Planar electrodes had similar XRD patterns to those of nanotube arrays and are not shown here. As shown in the figure, the only peaks appearing in the as-anodized samples were those of the niobium metal substrate, indicating that the as-anodized electrodes were amorphous. The as-synthesized electrodes required calcination in air at 750 °C to crystallize into the orthorhombic phase (JCPDS index: 30-0873) [19]. Crystallite sizes for the nanotube array and planar electrodes determined by the Scherrer equation were 24 and 36 nm, respectively. The crystallite sizes played a crucial role in the total charge capacity of the planar and nanotube array electrodes, as further discussed below.

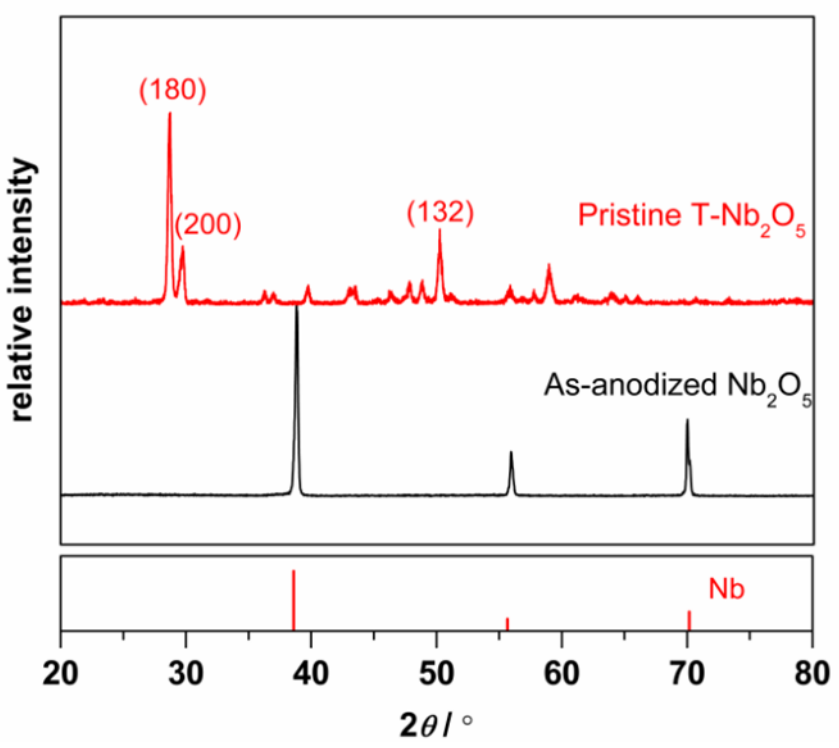

Figure 4.5: Representative XRD patterns for amorphous and orthorhombic Nb_2O_5 nanotube arrays. Nanotube array and planar electrodes have similar XRD patterns.

4.3.3 Electrochemical Characterization

Dunn et al. demonstrated that Li^+ ion charge storage in T-Nb_2O_5 proceeds via the insertion of Li^+ ions into the low diffusion energy (180) planes. The intercalation of Li^+ ions is associated with the simultaneous reduction of Nb^{5+} to Nb^{4+} [12]. The thermodynamics of the T-Nb_2O_5 system are governed by a single-well energy potential, resulting in the single-phase solid solution diffusion of Li^+ ions during intercalation and de-intercalation, as represented in Equation 4.1 [12, 20]:

$$Nb_2O_5 + xLi^+ + xe^- \rightarrow Li_xNb_2O_5 \qquad \text{(Equation 4.1)}$$

Here, x represents the state of discharge, ranging from 0 to 2, for a theoretical capacity of ~200 mAh/g [21].

4.3.3.1 Effect of Crystallinity on Charge Storage

The electrochemical behaviors of amorphous and T-Nb_2O_5 nanotube array electrodes were investigated using CV. Figure 4.6 shows the CV response for amorphous and crystalline samples of the nanotube arrays of the same dimensions (~1 μm thick) and geometrical surface areas (1 cm^2) at 2 mV/s. For the amorphous electrode sample, very negligible electrochemical activity was observed as compared to the crystalline electrode sample. Clearly defined oxidation and reduction peaks were observed at 2.1 and 1.5 V, respectively, for the crystalline electrode. The large voltage peak separation between the redox potentials is characteristic of battery materials and is a result of slow Li^+ ion diffusivity (~ 10^{-10} cm^2/s) in the T-Nb_2O_5 crystal [12, 21].

The differences in the CV responses of the amorphous and crystalline phases suggests that charge storage in Nb_2O_5 only occurs in significant amounts when the material has long-range ordering, as in the case of the crystalline phase. The amorphous phase lacks long-range ordering, and only minimal Li^+ ion intercalation occurs. Also, because the amorphous phase shows negligible electrochemical activity, we concluded that surface storage was not the main charge storage mechanism in T-Nb_2O_5, but it was bulk intercalation storage instead. This result corroborates previous findings by Dunn [12] and Koshiba [11]. The Li^+ intercalation reaction was associated with a change in the coloration of the crystalline electrode from an off-white to a navy-blue coloration. The color did not completely return to white at the end of the de-intercalation reaction, indicating that some Li^+ ions could not be fully extracted from the electrode. The blue coloration observed was due to the electrochromic properties of crystalline Nb_2O_5 [22]. It was also interesting to note that the amorphous electrode did not undergo the color transition, a result of the minimal intercalation of Li^+ ions into the material as mentioned above.

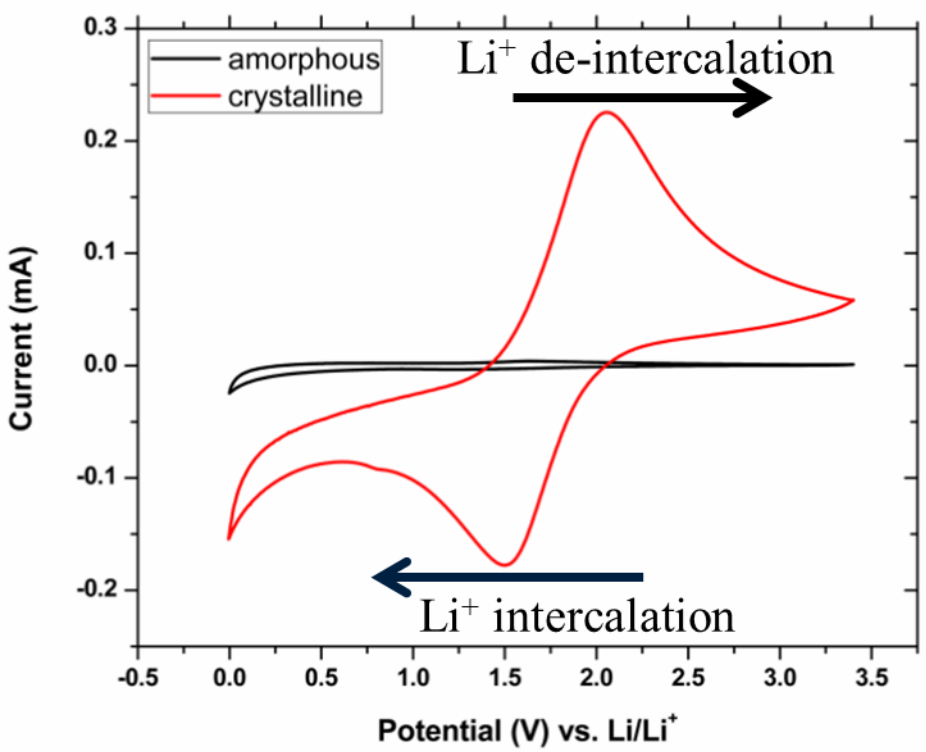

Figure 4.6: Cyclic voltammograms (at 2 mV/s) for amorphous and crystalline electrodes. Amorphous electrodes exhibited negligible electrochemical activity in comparison to crystalline electrodes.

4.3.3.2 Structural Changes in T-Nb_2O_5 during Electrochemical Cycling

First principles computational studies by Ceder et al. indicated that the strongest barrier to ion intercalation in battery materials is the electrostatic repulsion between the intercalating ions and the metal cations within the crystal lattice [5]. They showed that the activation barrier for Li^+ ion migration increased dramatically, by as much as 200%, for only a 4% reduction in the inter-planar spacing of a material. Therefore, crystallographic planes with the largest lattice spacings offer the least resistance to the diffusion of Li^+ ions in the crystal. For our electrode samples, the highest lattice spacing was for the (180) planes. As such, it was expected that intercalation would occur in the (180) planes.

Ex-situ XRD patterns for unlithiated T-Nb_2O_5, lithiated planar, and lithiated nanotube array materials are shown in Figure 4.7. The XRD patterns showed that Li^+ ion intercalation occurs in the (180) planes, as previously demonstrated by Koshiba and co-workers [11]. The nanotube array electrode was discharged to 0.1 V at a rate of 0.067C. As determined by the JADE software, the *a*, *b*, and *c* lattice constants of the nanotube array T-Nb_2O_5 increased from 6.31, 29.3, and 3.93 Å to 6.35, 29.4, and 3.94 Å, respectively, after lithiation. This represented a volume change of 1.2% and is typical for many intercalation materials [23]. The (180) peak shifted from 2.98 to 3.13 Å, indicating a 5.3% increase in the (180) inter-planar spacing (Figure 4.7). Meanwhile, only insignificant shifts occurred in the other planes such as the (200) planes. This demonstrated that the high-rate intercalation of Li^+ ions during discharge thermodynamically favored the (180) planes. We also observed a significant decrease in the peak intensities of the discharged materials. Similar findings were previously reported by Koshiba and co-workers in their studies on mesoporous T-Nb_2O_5 electrodes [11]. Koshiba et al. attributed the decrease in the XRD peak intensities to a reduction in the crystallite size caused by an increase in the stress within the crystal lattice due to the intercalation of Li^+ ions into the Nb_2O_5 [11]. An interesting finding in this study that had not been reported in the literature was that when the same discharging conditions were applied to a planar electrode, the (180) plane remained un-shifted, but had a lower intensity, as shown in Figure 4.7. Additionally, an extra peak also appeared at lower angles, representing an increase in the (180) inter-planar spacing due to the intercalation of Li^+ ions. Some of the (180) planes remained un-shifted because of the incomplete lithiation of the electrode. As mentioned earlier, nanotube array and planar electrodes had crystallite sizes of 24 (18 nm after discharge) and 36 nm, respectively, indicating that the materials were polycrystalline. Therefore, in planar electrodes, we hypothesized that

polycrystallinity resulted in the misalignment of (180) planes of adjacent crystallites, preventing the full lithiation of the material and resulting in the appearance of a lower intensity (180) peak as well as the extra peak at lower angles. As shown later, this also caused a loss of specific capacity in the planar electrodes. However, in the case of nanotube array electrodes, the thin nanotube wall thicknesses of ~ 17 nm resulted in the full lithiation of the material, causing a complete shift in the (180) plane.

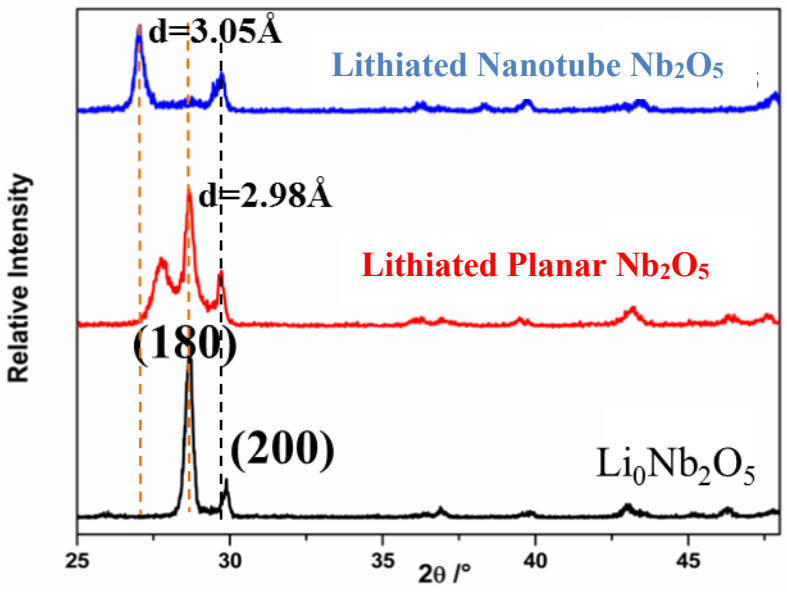

Figure 4.7: XRD patterns for T-Nb_2O_5 at states of full charge (x = 0) and full discharge ($x \approx 2$). The intercalation of Li^+ ions occurs in the (180) planes with a low-diffusion barrier.

4.3.3.3 Effect of Electrode Morphology on Charge Storage

To gain a qualitative understanding of the effect of the electrode morphology on the charge storage kinetics of the T-Nb_2O_5, CV was carried out for each morphology at various scan rates from 0.5 to 500 mV/s. Nanotube array and planar electrodes of the same geometrical surface area (1 cm^2) were used. As seen in Figure 4.8, the nanotube array electrodes exhibited significantly higher specific currents than the planar electrodes, especially at higher scan rates.

The excellent kinetic response of the T-Nb_2O_5 nanotube array electrodes, even in the absence of electron conductive additives, strongly suggests that this morphology allowed for faster Li^+ ion transport than the planar morphology. The absence of electron conductive additives in T-Nb_2O_5 was previously shown to be detrimental to lithiation by Koshiba et al., and they attributed the poor intercalation behavior to the poor conductivity of T-Nb_2O_5 [11]. The active electrochemical areas of the nanotube array and planar electrodes were measured as 1 ± 0.1 and 9.9 ± 1 cm^2/cm^2, respectively. Electrochemical surface areas were measured using CV measurements in a small cycling window where no redox activity occurs (3.4 – 3.45 V in the case of T-Nb_2O_5). The method is described in section 3.3.1 of this dissertation. Our observation that there was negligible surface charge storage suggests that the higher electrochemical surface area of the nanotube arrays allowed for an increased exposure of the low-energy (180) intercalation planes to the electrolyte, resulting in increased specific currents. Moreover, the thin nanotube walls resulted in shorter diffusion time scales and faster kinetic responses. Guo et al. also suggested that the nanotube array structure would allow for the one-dimensional transport of electrons, as opposed to the tortuous electron pathway in planar electrodes [1]. In our work, we did not conduct experiments to investigate the path of charge carriers during electrochemical cycling. One way to carry out such an investigation might be the use of single-crystal Nb_2O_5. By selectively orienting the (180) planes (where lithiation occurs) perpendicular or parallel to the long axis of the nanotube arrays, one could probe whether or not there is orthogonalization of Li^+ ion and electron transport. However, fabricating single-crystals is a major challenge. The disparity in the electrochemical performance between the nanotube array and planar electrodes is also evident in the kinetic responses of the two morphologies at high scan rates. Higher cycling rates resulted in increased redox peak separations, especially in the planar electrodes. Larger

peak separations are typically a result of higher over-potentials necessary to deliver higher current densities [12], which were likely more significant for the planar electrodes due to longer ion diffusion lengths. Large over-potentials also manifest as increased hysteresis between the charge and discharge profiles during cycling [12].

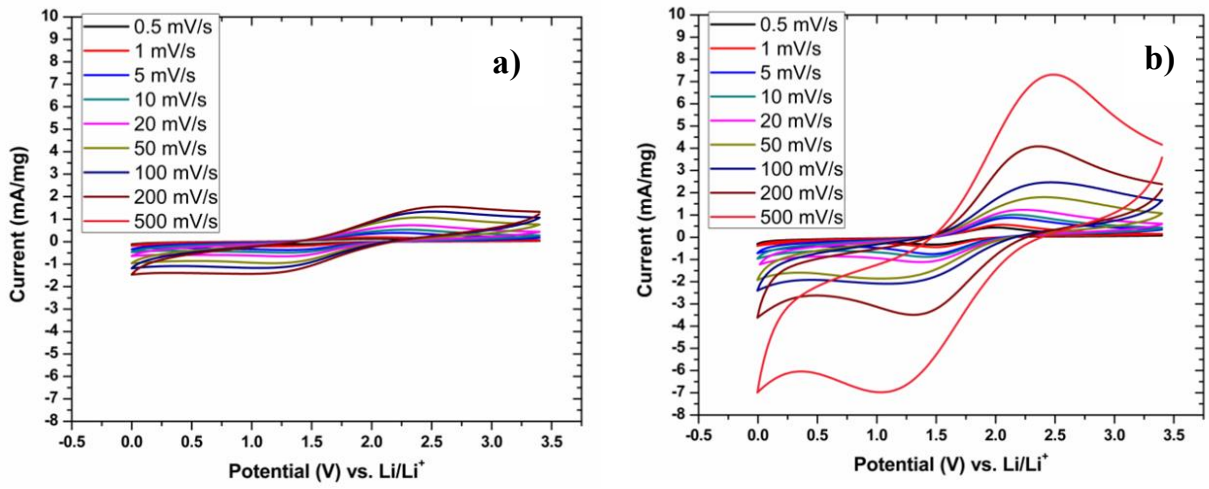

Figure 4.8: Cyclic voltammograms of a) planar, and b) nanotube array electrodes at varying scan rates shows a disparity in the kinetic response of the two morphologies.

A slightly different perspective of the CV results is presented in Figure 4.9, which shows the peak oxidation (de-intercalation) currents extracted from Figure 4.8. At low scan rates (below 25 mV/s), both morphologies show increasing peak oxidation currents with increasing scan rate. This is a result of the low scan rates allowing enough time for the intercalation of Li^+ ions into the T-Nb_2O_5 crystal structure. However, at scan rates ≥ 50 mV/s, the scan rate outpaces the low diffusivity of the Li^+ ions in the T-Nb_2O_5 crystal, resulting in smaller current increase. This effect is magnified in the planar electrodes due to the longer diffusion distances of the planar electrodes than those of the nanotube array electrodes. Hence the peak current reaches a plateau in the planar electrodes, an indication of mass transfer limitations in this morphology. As discussed earlier, the polycrystallinity of the materials also played a role as this led to the

misalignment of the (180) intercalation planes, impeding further lithiation in the planar electrodes. For the nanotube array electrodes, the peak current was still rising even at very high scan rates, showing that there were no transport limitations to the intercalation of Li^+ ions for this morphology. We attributed this to the short Li^+ ion diffusion length scale and the one-dimensional electron transport in the nanotube arrays.

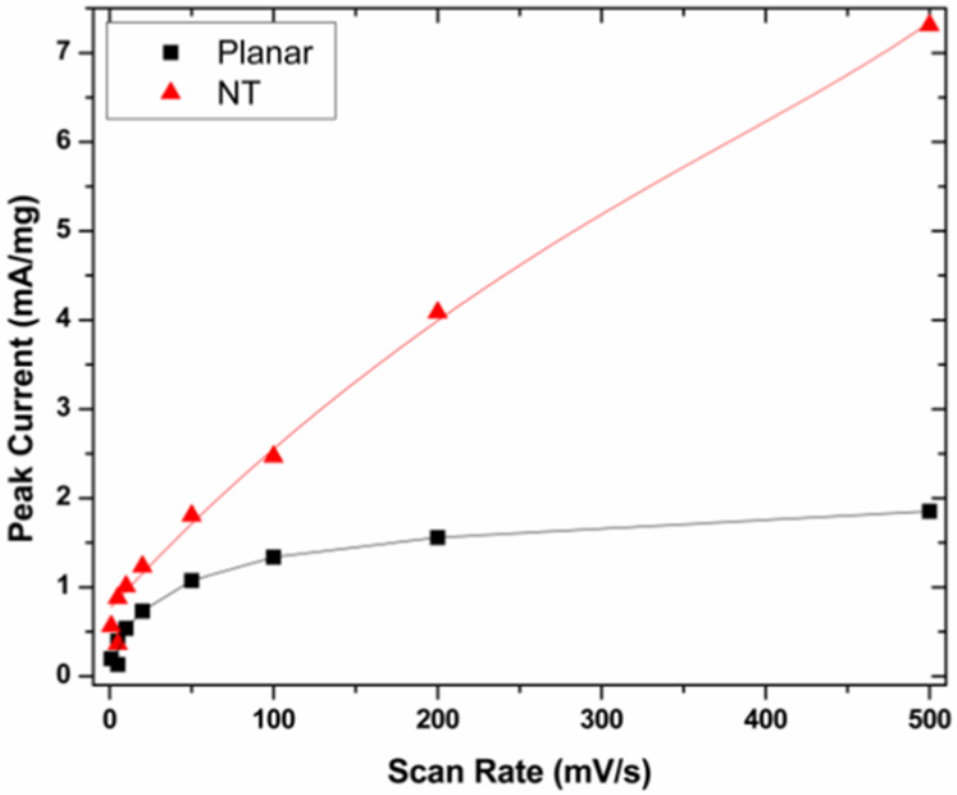

Figure 4.9: Peak oxidation currents for planar and nanotube array electrodes. Planar electrodes show diffusion limitations at high scan rates. Nanotube array electrodes show excellent intercalation kinetics even at high scan rates due to small diffusion distances and one-dimensional electron transport.

To further investigate the effect of the electrode morphology on the electrochemical behavior of the T-Nb_2O_5, electrochemical impedance measurements of the samples at different states of discharge, *x*, in $Li_xNb_2O_5$, were carried out. The results are shown in Figure 4.10. Samples were lithiated under potentiostatic conditions at 0.1 V for 15 h to attain a state of full

lithiation ($x \approx 2$), estimated based on the current and the voltage profile during discharge. To obtain a partially lithiated state, $x = x_{partial}$, the materials were first fully discharged, then recharged at a voltage of 1.6 V for 15 h. At all states of discharge, the nanotube array morphology exhibited a charge transfer resistance that was at least four times lower than that of the planar morphology. For example, at $x \approx 2$, the nanotube array electrodes had a charge transfer resistance of ~45 Ω compared to the ~225 Ω exhibited by the planar electrodes. These results corroborated our findings from CV and were attributed to the shorter diffusion length scale and one dimensional electron transport in the nanotube arrays compared to that of the planar electrodes [1]. Note that the charge transfer resistance for both morphologies decreased significantly with lithiation. Previous studies by Dunn et al. showed that the electrical conductivity of T-Nb_2O_5 increased with lithiation and attributed this finding to an increase in the concentration of Li^+ ion dopants [12]. Therefore, it may be possible that the decrease in the charge transfer resistance that we observed with lithiation can be explained on a similar argument.

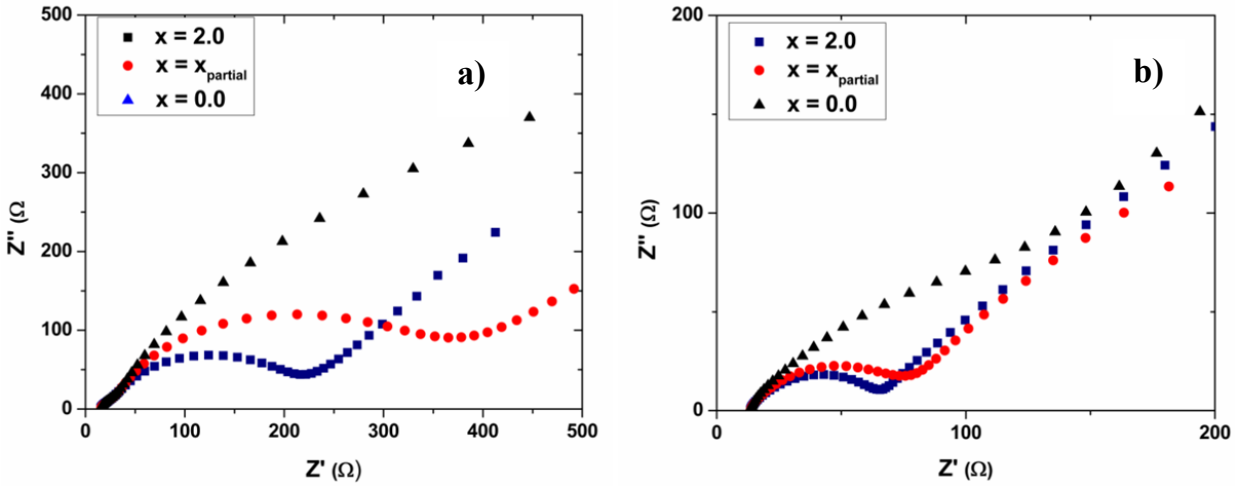

Figure 4.10: Electrochemical impedance measurements at various states of discharge reveal a four-fold reduction in the charge transfer resistance from a) planar, to b) nanotube array morphologies.

The rate capabilities of the nanotube array and planar electrodes were tested using charge/discharge (C/D) experiments. The C/D profiles for planar and nanotube arrays cycled at a rate of ~ C/5 are shown in Figure 4.11. Both morphologies exhibited continuous, monotonic variations in the voltage, indicating that a single-phase reaction was occurring during lithiation and de-lithiation [12, 20]. At this C/D rate, the planar electrodes showed more hysteresis than the nanotube array electrodes, likely due to the higher charge transfer resistance in the planar electrodes. Even at the lowest C/D rate (0.03C) that we characterized the nanotube array electrodes, a significant amount of hysteresis remained. Yushin et al. suggested that the hysteretic behavior observed in many intercalation systems is a result of poor electrical conductivities [24]. T-Nb_2O_5 is insulating, with an electrical conductivity of ~$3x10^{-6}$ S/cm [25], which would explain the hysteresis observed in our electrodes. Gaberscek et al. used a many-particle thermodynamics ensemble to understand the origin of hysteresis in intercalation batteries. Their calculations revealed that hysteresis in intercalation materials is not entirely of kinetic origins, with thermodynamics playing a role as well [26].

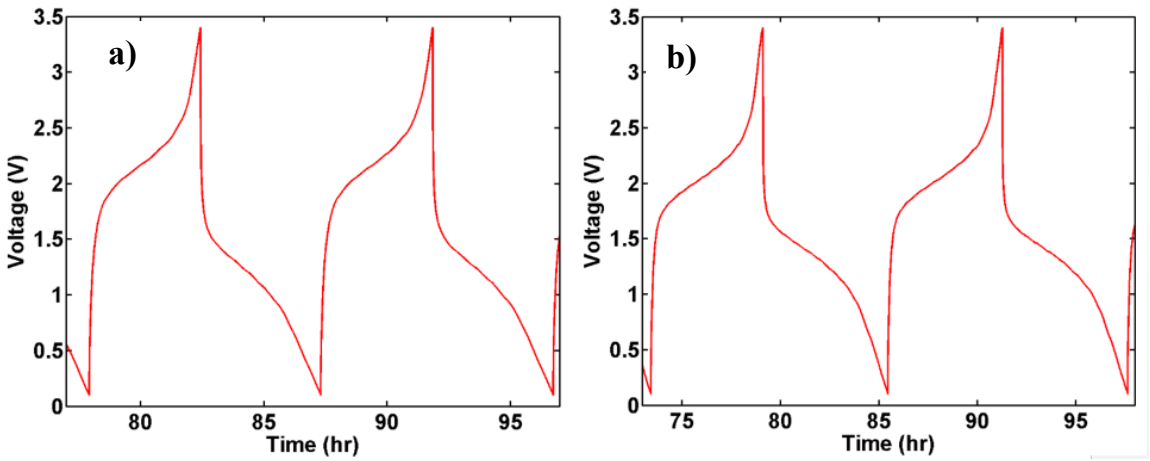

Figure 4.11: Charge/Discharge profiles for a) planar and b) nanotube array electrodes cycled at a rate of ~ C/5. Planar electrodes exhibited more hysteresis due to their higher charge transfer resistance.

The nanotube array morphology exhibited significantly higher specific capacities over the planar morphology in the medium-range discharge rates (between 0.1 and 2C), as shown in Figure 4.12. As discussed earlier, the enhanced rate performance of the nanotube array electrodes over that of planar electrodes was a result of the increased exposure of the energetically favored (180) diffusion planes, as well as rapid one-dimensional electron transport in the nanotubes. At low discharge rates of less than 0.03C, the specific capacity of the planar electrodes approached those of nanotube array electrodes. This was a result of low discharge rates allowing enough time for Li^+ ions to intercalate through the T-Nb_2O_5, likely through grain boundaries [27]. Cycling at rates higher than 2C resulted in similar specific capacities for nanotube array and planar electrodes. Such high cycling rates do not allow sufficient time for Li^+ ions to diffuse into the T-Nb_2O_5. Instead, most electrochemical activity is restricted to the surface of the electrodes, resulting in low capacities of less than 30 mAh/g.

As determined by ICP, the capacity of the nanotube samples discharged at the low rate of 0.03C was 189 mAh/g, corresponding to a state of discharge of $x = 1.8$, which approaches the fully discharged state of $x = 2.0$. Surprisingly, even with the thin nanotube wall thickness, the state of discharge did not reach the theoretical value of 2.0. Dunn et al. argued that Li^+ ion intercalation slows down at higher Li^+ concentrations owing to lower availability of unoccupied intercalation sites and more electrostatic repulsion between Li^+ and Nb^{5+} ions [12]. Koshiba et al. also suggested that it is likely that the arrangement of niobium ions in the intercalation planes became slightly disordered beyond a discharge state of $x = 1$ [11]. The disordering might suggest a thermodynamic resistance to further lithiation, limiting the experimental discharge state to $x < 2.0$. This led us to hypothesize that the limitations to achieving the full discharge state of $x = 2$ in

T-Nb_2O_5 might be the availability of low-energy intercalation sites and the cationic electrostatic repulsion between Nb^{5+} and Li^+ ions.

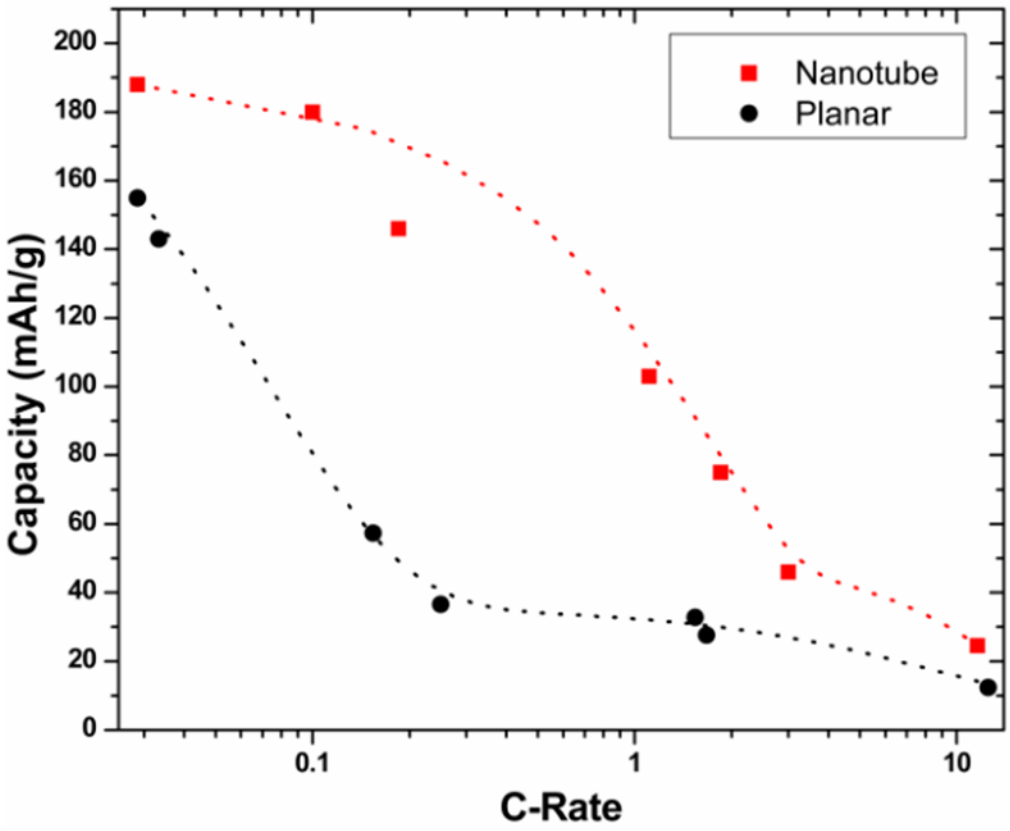

Figure 4.12: Rate capabilities of planar and nanotube array electrodes. The nanotube array electrodes exhibited significantly higher specific capacities at discharge rates between 0.1 and 2C.

4.4 Summary and Conclusions

This chapter investigated Nb_2O_5 for application in electrochemical energy storage. Nb_2O_5 in two morphologies, planar and nanotube arrays, were synthesized via the electrochemical anodization of niobium foils in electrolytic solutions containing ammonium fluoride ions. A study of the electrochemical behavior of Nb_2O_5 revealed that crystallinity plays a crucial role in the intercalation of Li^+ ions in Nb_2O_5. Amorphous Nb_2O_5 exhibited negligible Li^+ intercalation

behavior compared to that of orthorhombic Nb_2O_5 (T-Nb_2O_5). Intercalation proceeded via the (180) planes. These planes were previously observed to present the smallest barrier to Li^+ diffusion and therefore provided a low diffusion energy pathway for the high rate, reversible intercalation of Li^+ ions into the T-Nb_2O_5 crystal [11, 12]. Furthermore, a comparative study of the effect of nanostructure on the electrochemical behavior of T-Nb_2O_5 showed a significant enhancement in the Li^+ ion intercalation kinetics, rate capability, and total Li^+ capacity in the nanotube array morphology over that of the planar morphology. For instance, at some discharge rates, it was observed that planar electrodes were only partially lithiated, as compared to full lithiation in nanotube array electrodes. At a discharge rate of 0.2C, the specific capacity of the nanotube array electrodes was more than four times higher than that of planar electrodes. Such a significant increase in the capacity of the nanotube array electrodes over that of planar electrodes was attributed to the higher electrochemical surface area of the nanotube arrays, which allowed increased access to the low energy (180) diffusion planes. In the case of planar electrodes, we hypothesized that poly-crystallinity resulted in the misalignment of the (180) planes of adjacent crystallites and the blockage of further lithiation that caused the reduction in the specific capacity. Furthermore, the reduction in the diffusion length scale of the nanotube arrays allowed for the observed high-rate performance. This reduction in the length scale was observed in SEM, as well as inferred from the fact that the charge transfer resistance of the nanotube array electrodes was more than four times lower than that of planar electrodes. The nanotube array structure also allowed for the one-dimensional electron transport, as opposed to the tortuous electron pathway in planar electrodes. High specific capacities of ~ 190 mAh/g were observed for nanotube arrays of T-Nb_2O_5 electrodes. The high specific capacities and high rate

performance was observed in the absence of carbon additives, demonstrating the promise of nanostructured T-Nb_2O_5 as a high-rate cathode for secondary electrochemical energy storage.

4.5 References

[1] Guo, Y.-G.; Hu, J.-S. Wan, L.-J. Nanostructured Materials for Electrochemical Devices. *Adv. Mater*. **2008**, *20*, 2878.

[2] Goodenough, J. B.; Kyu-Sung Park, K. S. The Li-Ion Rechargeable Battery: A Perspective *J. Am. Chem. Soc.* **2013**, *135*, 1167.

[3] Wang, Y.; Takahashi, K.; Lee, K. H.; Cao, G. Z. Nanostructured Vanadium Oxide Electrodes for Enhanced Lithium-Ion Intercalation. *Adv. Funct. Mater*. **2006**, *16*, 1133.

[4] Islam, M. S.; Fisher, C. A. J. Lithium and Sodium Battery Cathode Materials: Computational Insights into Voltage, Diffusion and Nanostructural Properties. *Chem. Soc. Rev.* **2014**, *43*, 185.

[5] Morgan, D.; Van der Ven, A.; Ceder, G. Li Conductivity in Li_xMPO_4 (M = Mn, Fe, Co, Ni) Olivine Materials. *Electrochem. Solid St.* **2004**, *7*, A30-A32.

[6] Zhao, Y.; Peng, L.; Liu, B.; Yu, G. Single-Crystalline $LiFePO_4$ Nanosheets for High-Rate Li-Ion Batteries. *Nano Lett.* **2014**, *14*, 2849.

[7] Wang, J.; Sun, X. Olivine $LiFePO_4$: the Remaining Challenges for Future Energy Storage. *Energy Environ. Sci.* **2015**, *8*, 1110.

[8] Yin, Y.; Hu, Y.; Wu, P.; Zhang, H.; Cai, C. A Graphene–amorphous $FePO_4$ Hollow Nanosphere Hybrid as a Cathode Material for Lithium Ion Batteries. *Chem. Commun.* **2012**, *48*, 2137.

[9] Lee, Y. J.; Belcher, A. M. Nanostructure Design of Amorphous $FePO_4$ Facilitated by a Virus for 3 V Lithium Ion Battery Cathodes. *J. Mater. Chem.* **2011**, *21*, 1033.

[10] Masquelier, C.; Reale, P.; Wurm, C.; Morcrette, M.; Dupont, L.; Larchera, D. Hydrated Iron Phosphates $FePO_4$-nH_2O and $Fe_4P_2O_7$-3-nH_2O as 3 V Positive Electrodes in Rechargeable Lithium Batteries. *J. Electrochem. Soc.* **2002**, *149*, A1037.

[11] Kumagai, N.; Koishikawa, Y.; Komaba, S.; Koshiba, N. Thermodynamics and Kinetics of Lithium Intercalation into Nb_2O_5 Electrodes for a 2 V Rechargeable Lithium Battery. *J. Electrochem. Soc.* **1999**, *146*, 3203.

[12] Augustyn, V.; Come, J.; Lowe, M. A.; Kim, J. W.; Taberna, P-L.; Tolbert, S. H.; Abruna, H. D.; Simon, P.; Dunn, B. High-rate Electrochemical Energy Storage through Li^+ Intercalation Pseudocapacitance, *Nature Mater.* **2013**, *12*, 518.

[13] Zhang, L.; Wu, H. B.; Lou, X. W. Iron-Oxide-Based Advanced Anode Materials for Lithium-Ion Batteries, *Adv. Energy Mater.* **2014**, *4*, 1300958.

[14] Chan, C. K.; Peng, H.; Liu, G.; McIlwrath, K.; Zhang, X. F.; Huggins, R. A.; Cui, Y. High-Performance Lithium Battery Anodes Using Silicon Nanowires, *Nat. Nanotechnol.* **2008**, *3*, 31.

[15] Mushove, T.; Breault, T. M.; Thompson, L. T. Synthesis and Characterization of Hematite Nanotube Arrays for Photocatalysis. *Ind. Eng. Chem. Res.* **2015**, *54*, 4285.

[16] Bard, A. J.; Faulkner, L. R. Electrochemical Methods: Fundamentals and Applications, 2nd Edition. *John Wiley and Sons, Inc.* **2001**.

[17] Yu, D. Y. W.; Fietzek, C.; Weydanz, W.; Donoue, K.; Inoue, T.; Kurokawa, H.; Fujitania, S. Study of $LiFePO_4$ by Cyclic Voltammetry. *J. Electrochem. Soc.* **2007**, *154*, A253.

[18] Yu, D. Y. W.; Donoue, K.; Inoue, T.; Fujimoto, M.; Fujitani, S. Effect of Electrode Parameters on $LiFePO_4$ Cathodes. *J. Electrochem. Soc.* **2006**, *153*, A835.

[19] Kodama, R.; Terada, Y.; Nakai, I.; Komaba, S.; Kumagai, N. Electrochemical and In Situ XAFS-XRD Investigation of Nb_2O_5 for Rechargable Lithium Batteries. *J. Electrochem. Soc.* **2006**, *153*, A583.

[20] Kumagai, N.; Ishiyama, I.; Tanno, K. Electrochemical and Structural Characteristics of Niobium (V) Oxide in a Rechargeable Lithium Battery. *J. Power. Sources* **1987**, *20*, 193.
[21] Come, J.; Augustyn, V.; Kim, J. W.; Rozier, P.; Taberna, P.-L.; Gogotsi, P.; Long, J. W.; Dunn, B.; Simon, P. Electrochemical Kinetics of Nanostructured Nb_2O_5 Electrodes. *J. Electrochem. Soc.* **2014**, *161*, A718.
[22] Romeroa, R.; Dalchieleb, E. A.; Martína, F.; Leinena, D.; Ramos-Barradoa, J. R. Electrochromic Behaviour of Nb_2O_5 Thin Films with Different Morphologies Obtained by Spray Pyrolysis. *Solar Energy Materials and Solar Cells* **2009**, *93*, 222.
[23] Kang, K.; Ceder, G. Factors That Affect Li Mobility in Layered Transition Metal Oxides., *Phys. Rev. B.* **2006**, *74*, 094105.
[24] Nitta, N.; Wu, F.; Lee, J. T.; Yushin, G. Li-ion Battery Materials: Present and Future. *Mater. Today* **2015**, *18*, 252.
[25] Rani, R. A; Zoolfakar, A. S.; O'Mullane, A. P.; Austin, M. W.; Kalantar-Zadeh, K. Thin Films and Nanostructures of Niobium Pentoxide: Fundamental Properties, Synthesis Methods and Applications. *J. Mater. Chem. A* **2014**, *2*, 15683.
[26] Dreyer, W.; Jamnik, J.; Guhlke, C.; Huth, R.; Moskon, J.; Gaberscek, M. The Thermodynamic Origin of Hysteresis in Insertion Batteries. *Nat. Mater.* **2010**, *9*, 448.
[27] Balke, N.; Jesse, S.; Morozovska, A. N.; Eliseev, E.; Chung, D. W.; Kim, Y.; Adamczyk, L.; Garcıa, R. E.; Dudney, N.; Kalinin, S. V. Nanoscale Mapping of Ion Diffusion in a Lithium-ion Battery Cathode. *Nature Nanotech.* **2010**, *5*, 749.

Chapter 5

Photodeposition of Nanostructure-Controlled M/WO_3 (M = Au, Ag, Pt) Catalysts for α,β–Aldehyde Hydrogenation

5.1 Introduction

Heterogeneous catalysts play a major role in many chemical industries [1], in pollution control, and in energy applications [2]. The application of noble metal nanoparticles is prevalent in a variety of chemical reactions that involve hydrogenation, partial/complete oxidation, and reduction [3]. Traditionally, the use of heterogeneous catalysts has focused on achieving high reaction rates [4]. However, with accelerating industrialization, several new applications have emerged. In complex reactions, it is important not only to achieve the desired products at appreciable yields, but also to avoid side reactions.

So far, the design of heterogeneous catalysts exhibiting high selectivity towards desired products has been a major challenge [5]. Traditional catalyst design and synthesis methods such as incipient wetness impregnation typically result in materials with a wide distribution of geometries and sizes, resulting in low product selectivity [5-6]. The development of new synthesis techniques enabling the precise control over material nanostructure has become essential and has grown into a very active research area.

In nanostructured heterogeneous catalysts, a unique and fascinating phenomenon emerges. In these materials, changes in the nanostructural features such as geometry and size can result in variations in the crystallographic facets of the catalyst that are in contact with the reactants. Typically, some facets with certain crystallographic orientations are more capable of facilitating

the adsorption of reactant molecules onto the catalyst surfaces than those with other orientations [5-6], leading to structure sensitivity in certain reactions. For instance, Li et al. reported the shape-dependent catalytic activity of silver metal nanoparticles in styrene oxidation [6]. Varying the geometry of the silver nanoparticles resulted in drastically different catalytic activities during the oxidation of styrene. In their study, truncated triangular silver nanoplates and spherical nanoparticles had predominantly (111) crystallographic planes on the surface, as opposed to silver nanocubes, which were dominated by (100) planes. The nanocubes exhibited a styrene oxidation rate that was at least 14 times higher than that of the nanoplates that was already four times higher than that of the spherical nanoparticles over a 3 h time period. The styrene oxidation rates were normalized to the surface areas of the silver catalysts that were determined from nitrogen adsorption experiments [6]. Li et al. also showed that the adsorption and activation of ethylene and oxygen were more thermodynamically favorable on the higher energy (100) planes [6], leading to the different observed reactivity [6].

As discussed in Chapter One, the use of light as a synthesis technique is a nascent but promising route for achieving heterogeneous catalysts with controlled nanostructure [7-9]. In this chapter, we sought to develop a simple photodeposition procedure using light for the synthesis of noble metal (M = Ag, Au, and Pt) nanoparticle catalysts, with precisely controlled geometry and size, supported on WO_3. We chose WO_3 (with a bandgap of 2.6 eV) as the support because of its wide absorption range in both the visible and ultraviolet portions of the electromagnetic spectrum, which allowed us to study the effects of different wavelengths on the photodeposition process. Silver and gold were selected for photodeposition because of their excellent plasmonic properties in the UV-vis spectrum, which facilitates photodeposition [10]. Platinum was also

selected for photodeposition because of the wide variety of reactions such as partial hydrogenation and oxidation that it can catalyze [11-12].

We aimed to gain a fundamental mechanistic understanding of the effect of various parameters governing the nucleation and growth of the noble metals during the photodeposition process. We carried out systematic experimental and statistical studies on the influence of the light flux, photon wavelength, illumination time, and metal precursor concentration on the photodeposited metal nanoparticle shape, size, and metal loading. The photodeposited nanoparticles were evaluated for the selective hydrogenation of crotonaldehyde, a model reaction for unsaturated α,β-aldehyde hydrogenation. The hydrogenation reaction activities and selectivities were then correlated with the nanostructural properties of the noble metal particles. Results from this study were expected to assist the development of simple synthesis techniques for the design of noble metal catalysts with controlled nanostructure for other reactions of interest.

5.2 Experimental Method

5.2.1 Materials

Precursor materials chloroplatinic acid hexahydrate (H_2PtCl_6), tetrachloroauric acid ($HAuCl_4$), and silver nitrate ($AgNO_3$), as well as the support materials (monoclinic-phase tungsten trioxide (WO_3) powders) for the photodeposition process, were purchased from Alfa Aesar. Ultrapure water (resistance 18.2 MΩ) to prepare the precursor/WO_3 suspensions was obtained from a Millipore Milli-Q water purification system. Chemicals used to perform the catalytic hydrogenation tests, crotonaldehyde (≥ 99.5%) and ethanol (100%), were purchased from Sigma Aldrich and Decon Labs, Inc., respectively.

5.2.2 Experimental Design

To investigate the effects of the primary factors on the photodeposition of noble metals on WO_3, two factorial experimental designs were constructed. The first experimental design investigated the primary factors at two levels, chosen at the extremes of the experimental ranges of each factor. We studied the effect of light irradiance (20 and 100 mW/cm^2), wavelength (350 and 460 nm), illumination time (10 and 120 minutes), and metal ion concentration (0.1 and 2 mM) on the loading of the photodeposited metals. From this first design, the few statistically significant factors and factor interactions that had the most influence on the extent of the total photodeposited metal loading were identified using the statistical analysis of variance (ANOVA). In-depth studies were then carried out to investigate the effects of these significant parameters on the shape and size of the photodeposited nanoparticles.

5.2.3 Material Synthesis

To synthesize the photodeposited M/WO_3 catalysts, suspensions of 50 mg WO_3 in 0.1 and 2 mM metal precursor solutions were prepared. Uniform dispersions of the WO_3 support were achieved by isolating the smaller WO_3 particle sizes by mixing in ethanol, allowing the larger particles to settle for 15 minutes, then decanting and drying the mixture overnight in a vacuum oven. Average crystallite sizes of the WO_3 were ~26 nm. Uniform WO_3 dispersion was important to achieve higher rates of photodeposition. To reduce electron-hole recombination rates during photodeposition, 0.15 M methanol was added to the mixture. The methanol acted as a hole scavenger for the photogenerated holes so that the photogenerated electrons could be fully utilized for the photodeposition process. The suspension was sonicated for 30 minutes in the dark in order to uniformly disperse the WO_3 nanoparticles in the precursor solution.

Photodeposition was performed by illuminating the metal precursor/WO_3 suspension with simulated AM 1.5G solar-spectrum light from a 300 W xenon lamp (Solar Light 16S-300) under continuous stirring using a magnetic bar and constant $N_{2(g)}$ purging. The xenon lamp was equipped with an AM 1.5 filter to simulate solar irradiation on the surface of the Earth. The desired illumination wavelengths were achieved via the filtration of the white light generated by the xenon lamp using light filters of 20 nm bandwidth centered at 350 (ultra-violet), 410 (violet), and 460 nm (blue). All photodeposition experiments were performed at room temperature and pressure. The photodeposited materials were recovered by centrifugation at 10 000 rpm for 10 minutes, washed with ultrapure water five times, and then dried in a vacuum oven at 80 ˚C for an hour.

5.2.4 Materials Characterization

The phase composition of the materials was determined by X-Ray Diffraction (XRD). XRD patterns were recorded on a Rigaku 600 Miniflex X-ray diffractometer equipped with a graphite monochromator and Cu Kα radiation (λ = 1.5 Å). Patterns were collected at a step size and scan rate of 0.02°/step and 2.00°/min, respectively. Phases were identified using MDI Jade version 10. The crystallite sizes of the WO_3 support and the photodeposited noble metals were estimated from peak broadening of the XRD patterns using the Scherrer equation.

The morphology and dispersion of the photodeposited nanoparticles for catalysts that were active for the hydrogenation of crotonaldehyde were studied using Transmission Electron Microscopy (TEM). Samples for TEM were prepared by dispersing the materials in an ethanol solution using an ultrasonicator then dropping small amounts onto a carbon grid. The samples were dried overnight before analysis with a JEOL 3100R05 Double Cs-Corrected TEM instrument.

A Varian 710-ES Inductively Coupled Plasma - Optical Emission Spectrometer (ICP-OES) was used to quantify the loadings of the noble metals photodeposited on the WO_3 support. This technique is capable of quantifying elements at the parts per million level. Approximately 50 mg of the catalyst materials were dissolved overnight in aqua regia. Thereafter, 2 mL of the mixtures were diluted by a factor of seven before being tested for noble-metal content using ICP-OES.

UV–vis spectroscopy was used to monitor changes in the plasmonic responses of the materials during the photodeposition process. Surface plasmons occur at the interface of metals and represent the resonance of oscillating surface electrons in response to an electromagnetic field. For a metal, the resonance frequency of these oscillations varies with the geometry and size of the nanoparticles [13-15]. Therefore, the geometry and size evolution of the materials during the photodeposition process could be inferred through measurements of the materials' plasmonic responses. Small samples of the material solutions were collected at regular time intervals during the photodeposition process and absorbance spectra for these materials were recorded using an Agilent-Cary 5000 spectrophotometer. A metal precursor/WO_3 mixture collected prior to the photodeposition process was used for background correction. However, because the plasmonic response is a function of both geometry and size [14-15], the use of UV-vis alone is insufficient for a complete characterization of the morphologies of the photodeposited nanoparticles. This necessitated the utilization of other techniques such as SEM and TEM to supplement UV-vis observations.

The hydrogenation reaction mixtures were analyzed using a Varian 450 Gas Chromatograph (GC) equipped with a flame ionization detector. The selectivity of each reaction product was calculated as the molar fraction of the product with respect to the total products. All

crotonaldehyde conversions were less than 10%. This meant the batch reactors were under differential conditions. Under differential conditions, the conversion is sufficiently low that the catalytic system is not limited by mass transport and, therefore, measured reactivities reflect the intrinsic kinetic rates of the reaction [16-17].

5.2.5 Catalytic Hydrogenation Tests

Prior to hydrogenation experiments, the catalyst materials were reduced in flowing hydrogen at a flow rate of 90 ml/min. Following previously reported experimental procedures, Ag/WO_3 and Au/WO_3 catalysts were reduced at 200 ˚C for 3 h [1, 18] and Pt/WO_3 catalysts were reduced at 450 ˚C for 4 h [18]. The catalytic activities and selectivities of the materials were tested in the hydrogenation of crotonaldehyde. The reaction mixture with 50 mg of catalyst suspended in a 0.07 M crotonaldehyde/ethanol solution was loaded in a 3 ml Swagelok batch reactor. The reactor was then placed under vacuum for three cycles of 30 s to remove oxygen. Between cycles, helium was used to purge the batch reactor. The reaction mixture was agitated with magnetic stirring, at a pressure of 400 kPa and a temperature of 70 ˚C. Blank experiments, carried out in the absence of noble metals, with only the crotonaldehyde mixture or with the crotonaldehyde mixture and the catalyst support (WO_3), were performed to isolate the catalytic activities of the photodeposited noble metals from those of the WO_3 support and those of the reactor. Prior to reaction, the support was treated using the same protocols as those for the M/WO_3 catalysts.

5.3 Results and Discussion

5.3.1 Silver Photodeposition

5.3.1.1 Effects of Irradiance, Wavelength, Time, and Concentration on Metal Loading

The initial screening to identify factors affecting the photodeposition process was carried out using silver. Table 5.1 shows the p-values for the correlation between each factor and the silver metal loading. Each p-value was computed from an F-statistic determined by ANOVA using the Minitab software. Lower p-values indicate stronger correlation between the factor and the metal loading. The illumination time was the most significantly correlated factor with the metal loading in the photodeposition of silver. This was expected, as increasing the illumination time allows for an increase in the electron-hole pair generation, resulting in the reduction of more Ag^+ ions by the photogenerated electrons.

The initial Ag^+ concentration was a marginally significant factor for the total silver loading. This result could be explained on the basis of an increased amount of Ag^+ ions available for reduction at higher concentrations. However, it was surprising to note that the irradiance did not play a significant role towards increased photodeposition. One plausible explanation for this observation is that the photodeposition process was limited by the low concentrations of the photoactive support (WO_3). The illumination wavelength showed the weakest correlation with the silver metal loading. This was expected as any illumination wavelength shorter than the absorption threshold of the WO_3 support would be capable of generating an electron-hole pair, resulting in similar loadings for these wavelengths. However, as discussed below, the illumination wavelength played an important role in the control of particle geometry.

Table 5.1: p-values for the correlation between each primary factor and the silver metal loading. The illumination time showed the strongest correlation, while the wavelength showed the weakest correlation with the metal loading.

Factor	Irradiance	Wavelength	Illumination Time	Ag^+ Concentration
p-value	0.44	0.79	0.010	0.17

5.3.1.2 Interactions between Factors

Figure 5.1 shows the ANOVA interaction plot for the factors of interest with regard to the total silver metal loading. An interaction between two factors exists when the response to varying one factor depends on the level of the other factor [19]. The black and red lines represent the low and high levels of each factor, respectively. As shown in Figure 5.1, there was no significant change to the metal loading after varying the wavelength at both low and high irradiance, indicating that there was no interaction between the irradiance (*i*) and the wavelength (λ), as expected. Also, at the low and high levels of both λ and *i*, an increase in the illumination time (*t*) resulted in increased metal loading, with a weak interaction between *t* and *I*. This result corroborates the significant p-value for *t* observed in Table 5.1. As there were no significant changes in the total metal loading with changes in the concentration (*c*) at the two levels of λ, there was no interaction between *c* and λ. Both *i* and *t* had interactions with *c*, with *t* showing a stronger interaction. This was expected, as raising the concentration of the Ag^+ ions and increasing the illumination time would result in a higher number of electron-hole pairs being generated over an extended time, and there are enough Ag^+ ions in solution to be reduced, resulting in much higher metal loadings.

The statistical analysis identified the metal precursor concentration and illumination time as the main factors affecting the total metal loading. Similar trends were observed for platinum,

and because gold exhibits a stronger plasmonic response than that of platinum [10], we assumed similar trends for gold as well. Because *i* only weakly correlated with the total metal loading and showed only weak interaction with both *t* and *c*, this factor was not investigated further; the irradiance for all further experiments was set at 100 mW/cm^2. Also, because an appreciable total metal loading was desirable, the metal salt concentration was kept at the higher level, 2 mM, for all further photodeposition experiments.

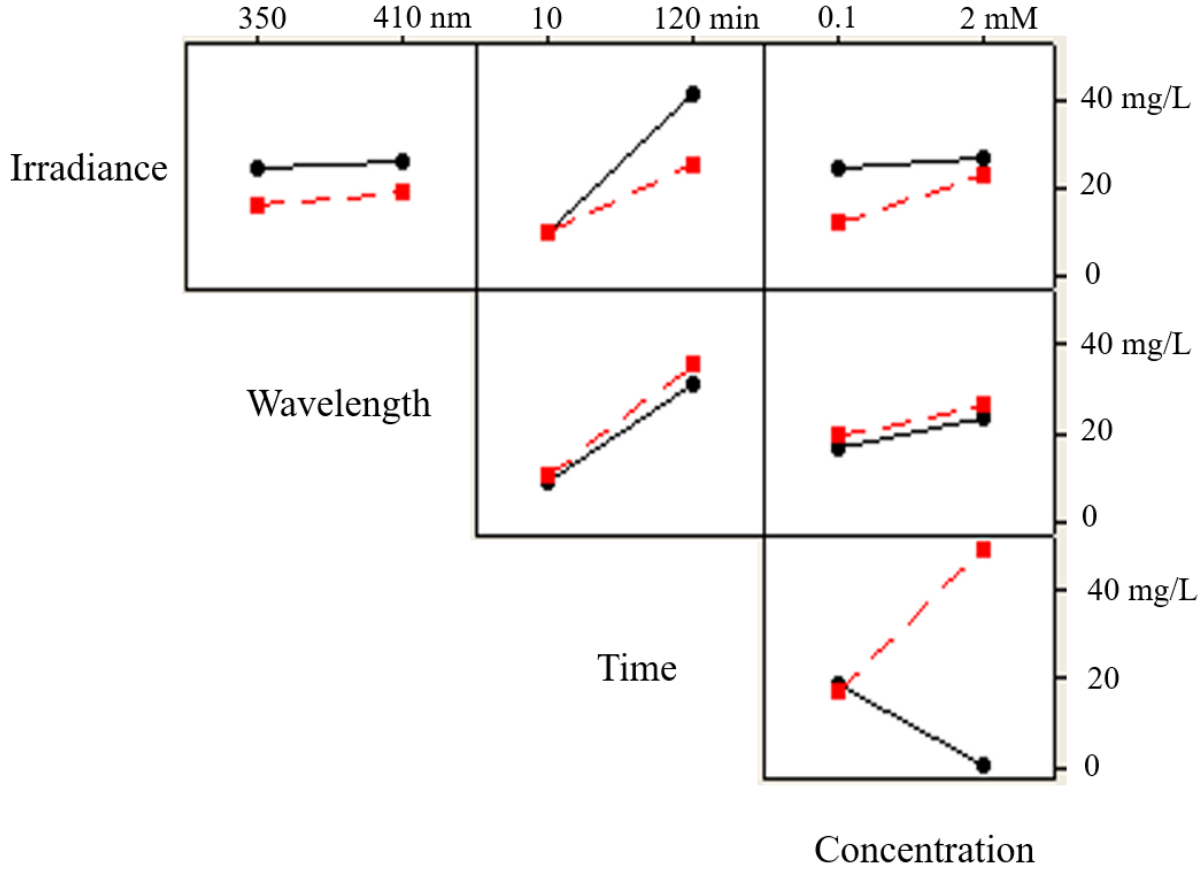

Figure 5.1: ANOVA factor interaction plot for the silver metal loading. Time and concentration showed the strongest interaction. There was no interaction between irradiance and wavelength. Interpretations of these observations are explained in the main text.

5.3.1.3 Bulk, Elemental, and Optical Characterization of Ag/WO_3 Materials

The XRD patterns for the Ag/WO_3 materials photodeposited at 350, 410, and 460 nm are shown in Figure 5.2. In all cases, the deposited nanoparticles were too small for detection by

XRD. The detection limit for XRD was approximately 0.3 nm. However, the photodeposited silver could be detected by ICP. The detection of the silver by ICP but not by XRD suggested that the silver nanoparticles were amorphous or well dispersed on the WO_3 support.

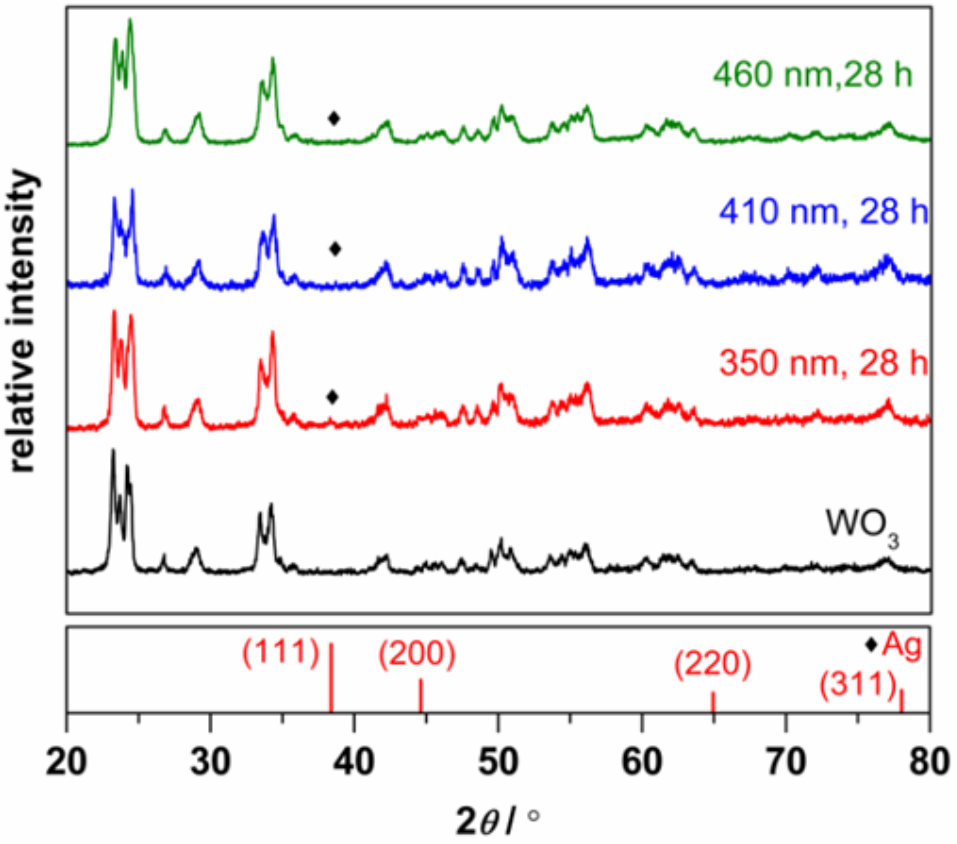

Figure 5.2: XRD patterns for silver nanoparticles photodeposited at various wavelengths. The nanoparticle sizes were below the detection limit of XRD.

Figure 5.3 shows the ICP results for the silver loading as a function of illumination time during the photodeposition process for experiments with an initial concentration of 3.6 mM. This initial concentration was selected to achieve the target silver weight loading of 18%. Dotted lines in this figure, and in all other ICP plots in this chapter, were fitted using a third degree polynomial and represent the best fits to the data. These lines carry no physical meaning and were used only to guide the eye. The metal loading increased rapidly up to 6 h; the increase was

more gradual between 6 and 12 h, likely due to the decreasing concentration of Ag^+ ions in the solution. After 20 h the metal loading plateaued at ~16 wt. % silver. This value also corresponded to the total silver content in the precursor solution. In other words, after 20 h of photodeposition all Ag^+ ions were consumed from the original solution. The fact that such a high loading of the photodeposited silver was not detected by XRD strongly suggests that the silver nanoparticles were amorphous.

The independence of the total silver weight loadings observed under the different illumination wavelengths after 20 h was not a surprise as the reduction of the Ag^+ ions only depends on the availability of the photogenerated electrons. In our investigations with WO_3, which exhibits an absorption onset of 460 nm, all incident light was energetic enough to generate electron-hole pairs. Experimental conditions of no illumination resulted in negligible silver nanoparticle formation, indicating that light played a central role in the deposition process.

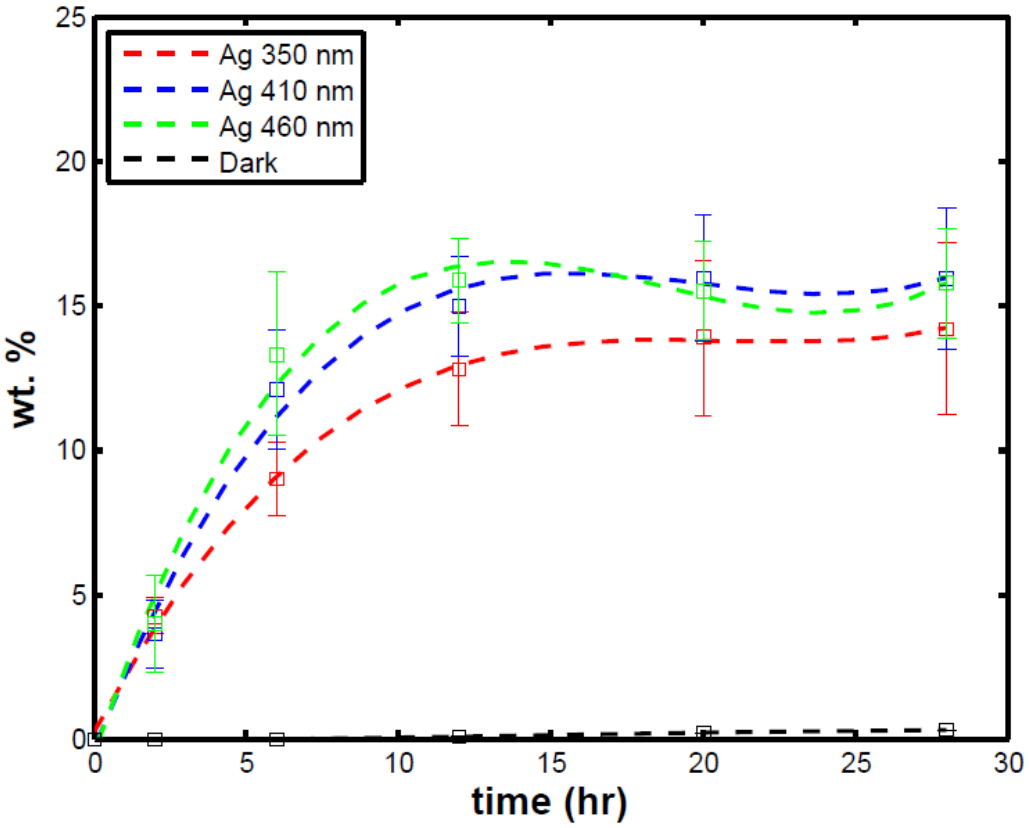

Figure 5.3: Silver metal weight loading as a function of time for nanoparticles photodeposited at various wavelengths. The loading plateaued at ~ 16% due to the complete consumption of silver precursor materials. Samples run under dark conditions showed negligible deposition in comparison to those run under illumination, indicating that light played a key role in the deposition process.

The time evolution of the photodeposition process for the silver nanoparticles at 350, 410, and 460 nm illumination wavelengths was observed by tracking the changes in the plasmonic responses of the materials and is shown in Figure 5.4. The characteristic plasmonic responses for the nanoparticles deposited at 350 and 410 nm illumination were similar, but different from those of nanoparticles deposited at 460 nm. A very sharp plasmonic peak was observed at ~370 nm for nanoparticles photodeposited at 350 and 410 nm. Amendola et al. observed a similar plasmonic response for silver nanoparticles with a spherical geometry and attributed the sharp peak to the small size of the nanoparticles [20]. With increasing illumination time, there was an increase in the absorbance of the solutions due to an increase in the weight

loading of the photodeposited silver. This increase in the weight loading was also observed using ICP, as discussed previously. There was also a general peak broadening, likely resulting from an increase in the size of the photodeposited silver nanoparticles [14]. The observed peak broadening could also be a result of an increase in the silver nanoparticle size distribution, as observed by Gupta et al. in the case of CdSe nanoparticles [15]. TEM for the photodeposited silver nanoparticles was not carried out in our investigation but could help understand the size and shape changes occurring during photodeposition.

Silver nanoparticles photodeposited at 460 nm exhibited two characteristic plasmonic peaks at ~475 and 525 nm. Amendola et al. attributed a similar plasmonic response for silver nanoparticles to a cuboid geometry [20]. Figure 5.5 shows photographs of materials synthesized under no illumination and for those synthesized at 350, 410, and 460 nm wavelengths. For the materials synthesized under no illumination, the color of the solution was similar to that before photodeposition. Nanoparticles photodeposited at 350 and 410 nm were similar in appearance and showed a dark grey coloration, while those photodeposited at 460 nm had a pinkish hue. This difference in color suggested the presence of differences in the geometries and physical dimensions of the silver nanoparticles photodeposited at 350 and 410 nm from those photodeposited at 460 nm.

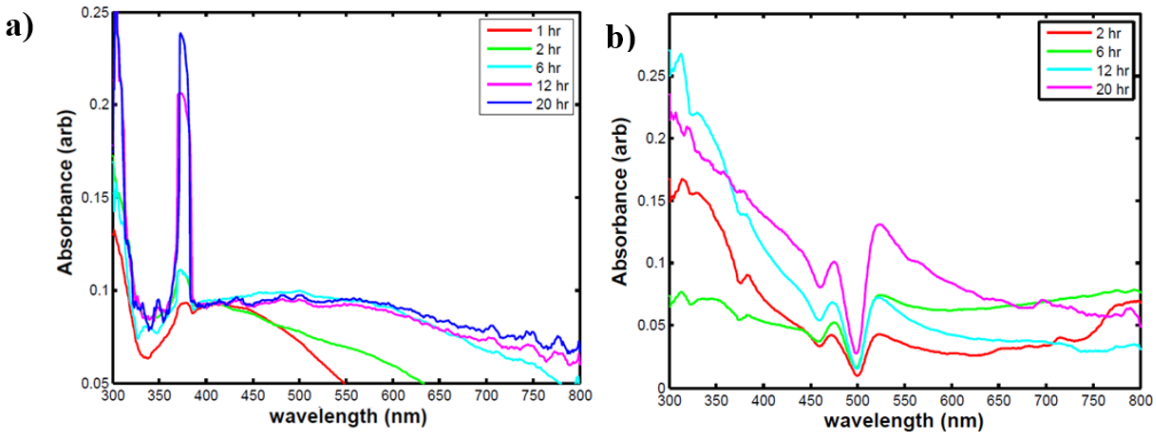

Figure 5.4: Plasmonic response of silver nanoparticles photodeposited at a) 350 and 410 nm. These materials exhibited a single, sharp peak due to their small size and likely spherical geometry. b) Nanoparticles photodeposited at 460 nm exhibited two plasmonic peaks due to anisotropy.

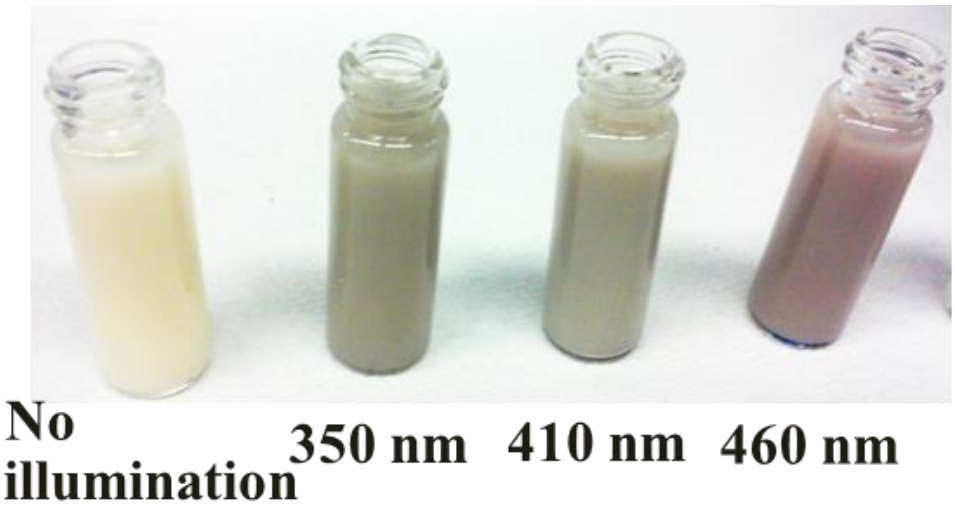

Figure 5.5: Photographs of silver nanoparticles photodeposited at various wavelengths. Differences in coloration indicate differences in nanoparticle geometry/size.

5.3.2 Gold Photodeposition

5.3.2.1 Bulk, Elemental, and Optical Characterization of Au/WO_3 Materials

Following the photodeposition of gold on WO_3, characteristic Au(111) peaks were identified in the XRD patterns for nanoparticles deposited at an illumination time of 28 h at 350, 410, and 460 nm wavelengths (Figure 5.6). Average crystallite sizes of the gold nanoparticles calculated using the Scherrer formula were 7.8, 7.2, and 7.2 nm for nanoparticles deposited at 350, 410, and 460 nm, respectively. Crystallite size determination using this formula can sometimes be inaccurate [21]. Therefore, future studies should also apply other techniques such as SEM and TEM to measure nanoparticle sizes.

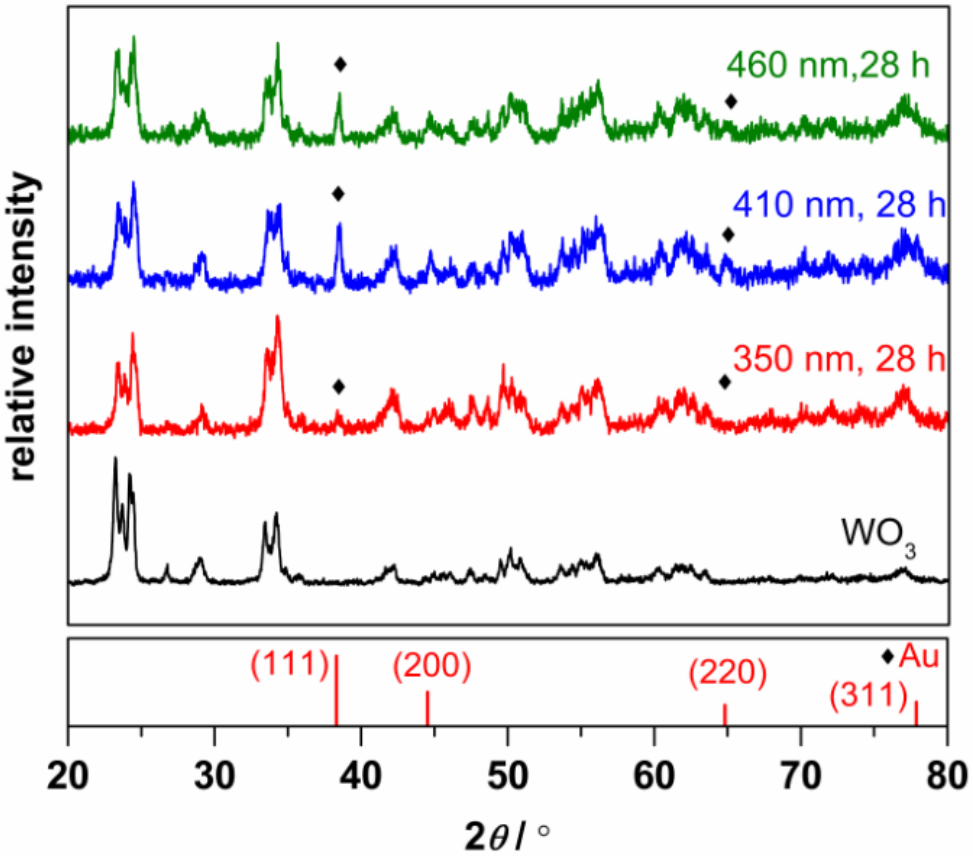

Figure 5.6: XRD patterns for gold nanoparticles photodeposited at various wavelengths. Characteristic Au(111) peaks were clearly identifiable.

The photodeposited gold loading increased with the illumination time from 0 to 20 h, as shown in Figure 5.7. After 20 h, the gold loading plateaued at ~20 wt. % gold due to the complete consumption of gold ions from the precursor solution through photodeposition on the WO_3 support. However, the photodeposition of gold nanoparticles took ~8 h longer to complete than the photodeposition of silver nanoparticles. This was likely a result of silver exhibiting a higher plasmonic quality factor than gold at each of the illumination wavelengths where photodeposition was performed.

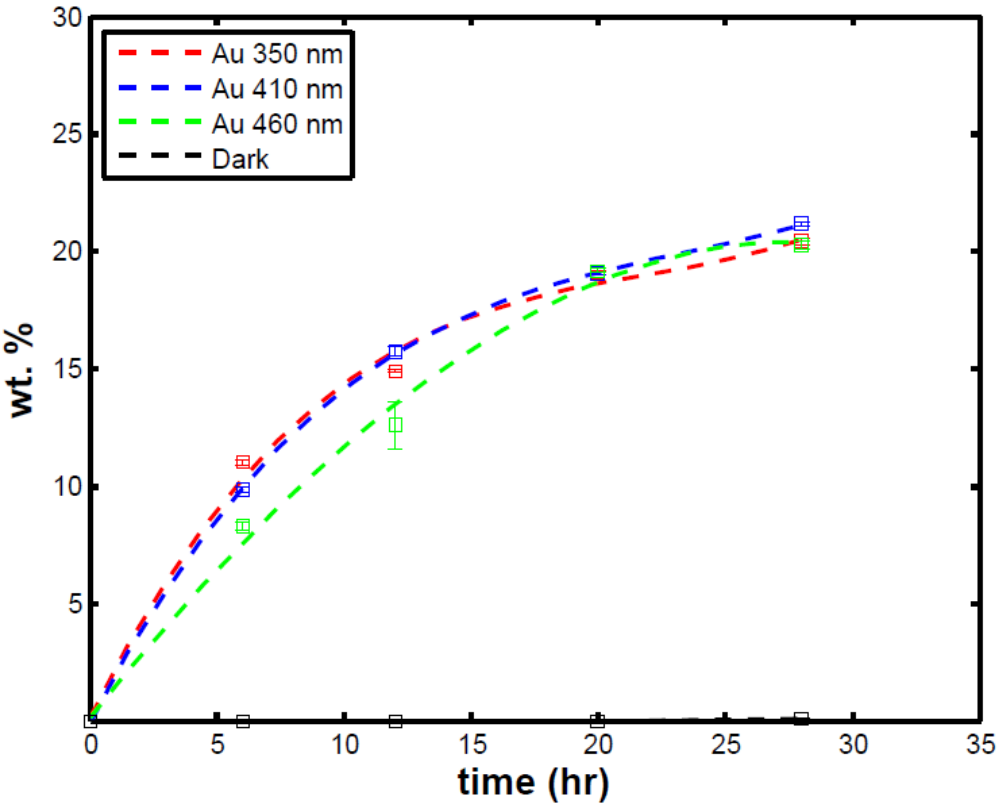

Figure 5.7: Gold metal weight loading as a function of time for gold photodeposition at various wavelengths. The loading plateaued at ~ 20% due to the complete consumption of gold precursor materials. Samples run under dark conditions showed negligible deposition in comparison to those run under illumination.

The characteristic plasmonic response of the materials photodeposited at 350 nm illumination was significantly different from those photodeposited at 410 and 460 nm. For 350 nm photodeposition, shown in Figure 5.8a, only one absorption peak centered at ~570 nm was observed, likely a consequence of the isotropy in the shape of the photodeposited nanoparticles. Also, the absorption spectra became broader and redshifted between six and 28 h. In addition, there was a slight increase in the absorbance of the solutions. As in the silver case, the redshift was attributable to an increase in the size of the gold nanoparticles in solution, while the increase in absorbance was due to an increase in the weight loading of the photodeposited nanoparticles with illumination time. The concentration increase was corroborated by ICP, as shown above. Gold photodeposited at 410 and 460 nm, shown in Figure 5.8 b/c, showed similar plasmonic responses, with two characteristic absorption peaks centered at ~465 and 570 nm. The appearance of two absorption peaks in the plasmonic response is typically a result of the photodeposited nanoparticles being anisotropic [8]. Figure 5.8d shows photographs for materials synthesized under no illumination and those synthesized at 350, 410, and 460 nm illuminations. Again, under no illumination, the solution was similar to that before photodeposition. After 350 nm photodeposition, the materials showed a light-grey color. The gold nanoparticles photodeposited at 410 and 460 nm both showed a pink coloration. This was to be expected, as these nanoparticles exhibited roughly similar absorbance spectra.

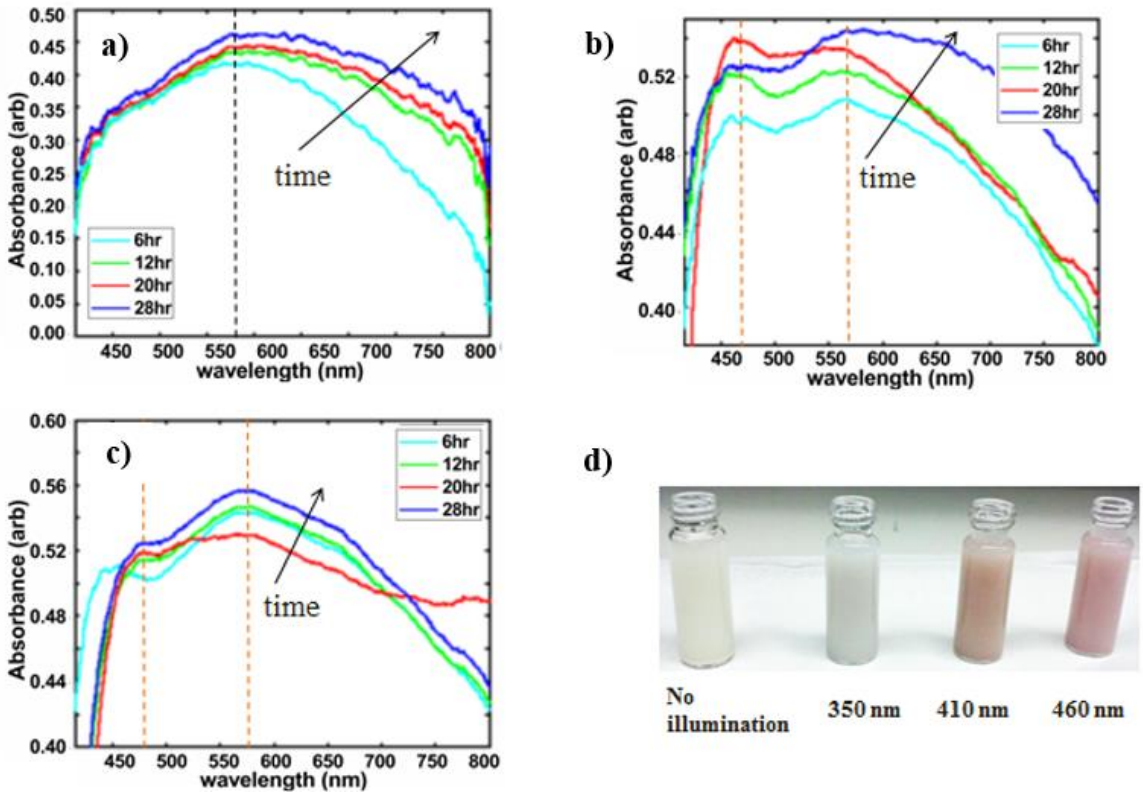

Figure 5.8: Plasmonic response of gold nanoparticles photodeposited at a) 350, b) 410, c) 460 nm. Nanoparticles photodeposited at 350 nm exhibited a single peak due to their spherical geometry, while nanoparticles photodeposited at 410 and 460 nm exhibited two plasmonic peaks due to anisotropy. d) Photographs of nanoparticles photodeposited at the various wavelengths. Differences in coloration indicate differences in nanoparticle geometry/size.

Representative TEM images for the photodeposited gold are shown in Figure 5.9.

Photodeposition at 350 nm resulted in a spherical geometry for the nanoparticles, with diameters ranging from approximately 100 to 200 nm. In contrast, nanoparticles photodeposited at 410 nm were a mixture of pentagonal (edge size of approximately 60 nm) and hexagonal (edge size of approximately 40 nm) geometries. As discussed above, results from UV-vis spectroscopy for the gold nanoparticles showed that photodeposition at 350 and 410 nm resulted in nanoparticles that exhibited one and two absorption peaks, respectively, suggesting differences in the geometries and/or sizes of the nanoparticles. Therefore, our TEM results are consistent with our findings from UV-vis spectroscopy. The differences in the nanoparticle geometries after illumination at

different illumination wavelengths can be explained on the basis of variations in the plasmonic responses of gold across the UV-vis spectrum. The optical absorption of metal nanoparticles is due to the excitation of surface plasmons as well as interband transitions. For gold, interband transitions are dominant for wavelengths less than 400 nm; surface plasmon excitations play a role between 400 and 600 nm [22]. The photogeneration of charges at the surface of the nanoparticles due to plasmon excitations likely causes the face-selective reduction of gold cations, resulting in the anisotropy observed at 410 nm. Mirkin et al. showed that an anisotropic distribution of charges on gold nanoparticle surfaces results in the anisotropic reduction of gold cations, resulting in non-spherical nanoparticles [23-24]. Mirkin also proposed the selective adsorption of cations on different nanoparticle faces as a possible alternative mechanism for the anisotropic growth [24]. However, this mechanism was unlikely in our case, as selective adsorption would then result in the growth of anisotropic nanoparticles at all illumination wavelengths, which is not observed at 350 nm. For our gold nanoparticles, due to the lack of surface plasmonic excitations at 350 nm [22], photodeposition at this wavelength resulted in the formation of isotropic spherical particles.

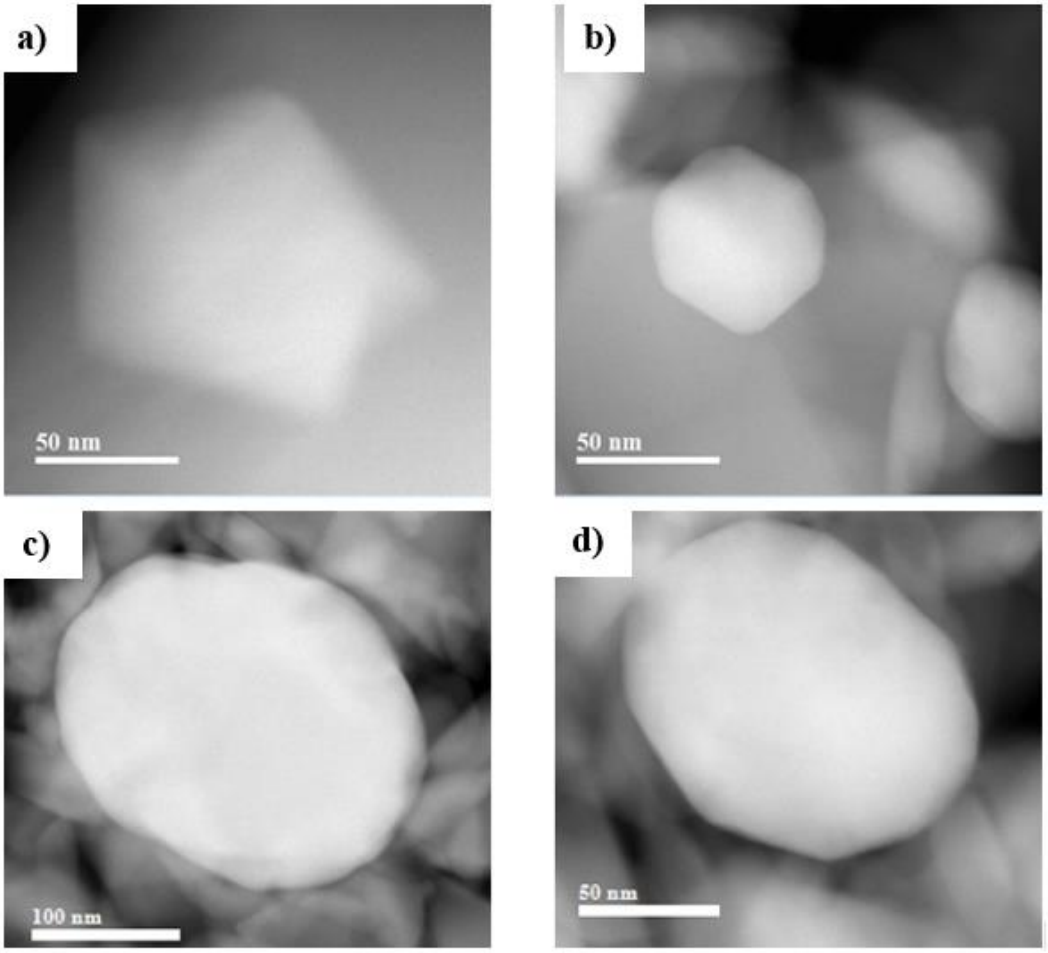

Figure 5.9: TEM images of gold nanoparticles photodeposited at a/b) 410 nm, c/d) 350 nm. Nanoparticles photodeposited at 410 nm had a pentagonal or hexagonal geometry, while nanoparticles photodeposited at 350 nm were spherical.

5.3.3 Platinum Photodeposition

5.3.3.1 Bulk, Elemental, and Optical Characterization of Pt/WO_3 Materials

The photodeposition of platinum on WO_3 resulted in identifiable Pt(111) peaks in XRD patterns as shown in Figure 5.10. However, complete photodeposition of the nanoparticles took ~50 h, more than 20 h longer than the illumination times observed for silver and gold photodeposition. It is possible that this relatively slow photodeposition process was a result of

the poor quality factor of platinum metal in the UV-vis part of the electromagnetic spectrum. Average crystallite sizes of the photodeposited nanoparticles calculated using the Scherrer formula were 8.4, 8.4, and 8.3 nm for illumination wavelengths of 350, 410, and 460 nm, respectively. As mentioned above, nanoparticle crystallite size determination using the Scherrer formula can be inaccurate [21], and other techniques such as SEM and TEM may be required for accurate size determination.

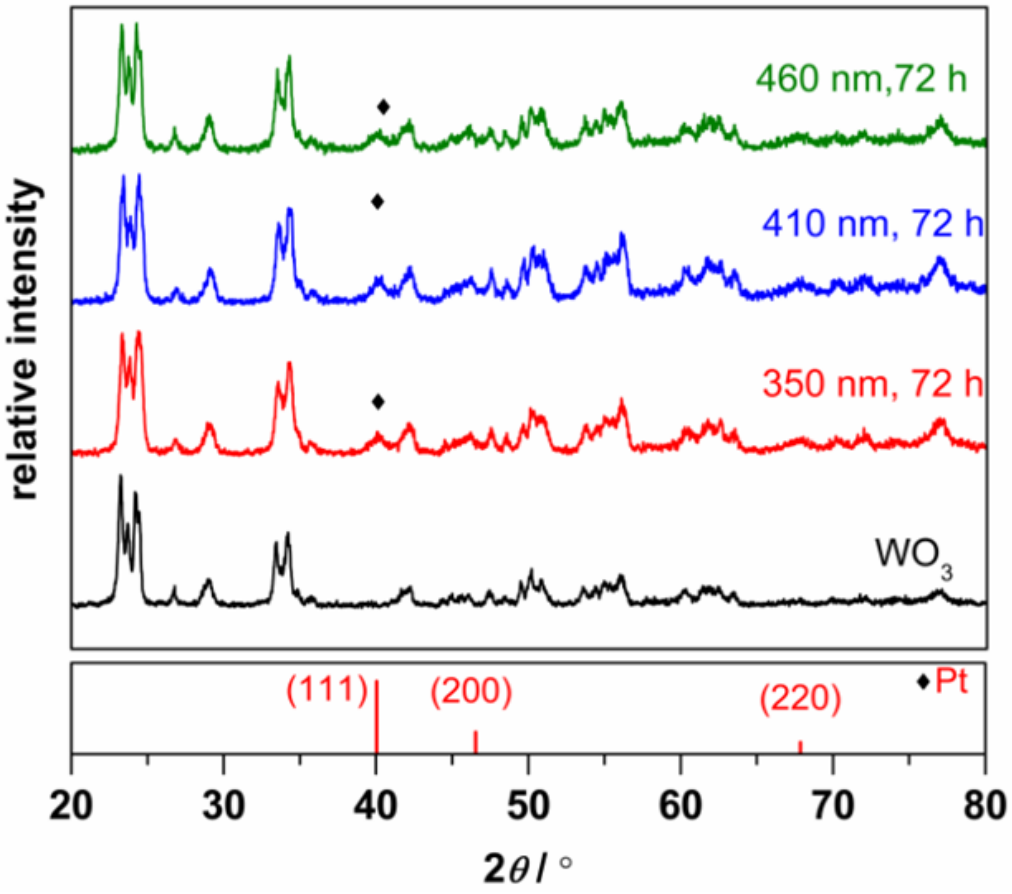

Figure 5.10: XRD patterns for platinum nanoparticles photodeposited at various wavelengths. Characteristic Pt(111) peaks were clearly identifiable.

The platinum metal loading increased steadily up to 35 h illumination time before plateauing at ~20% weight loading after 50 h (Figure 5.11). As with the cases of silver and gold, this value corresponded to the total deposition of the platinum precursor onto the WO_3 support.

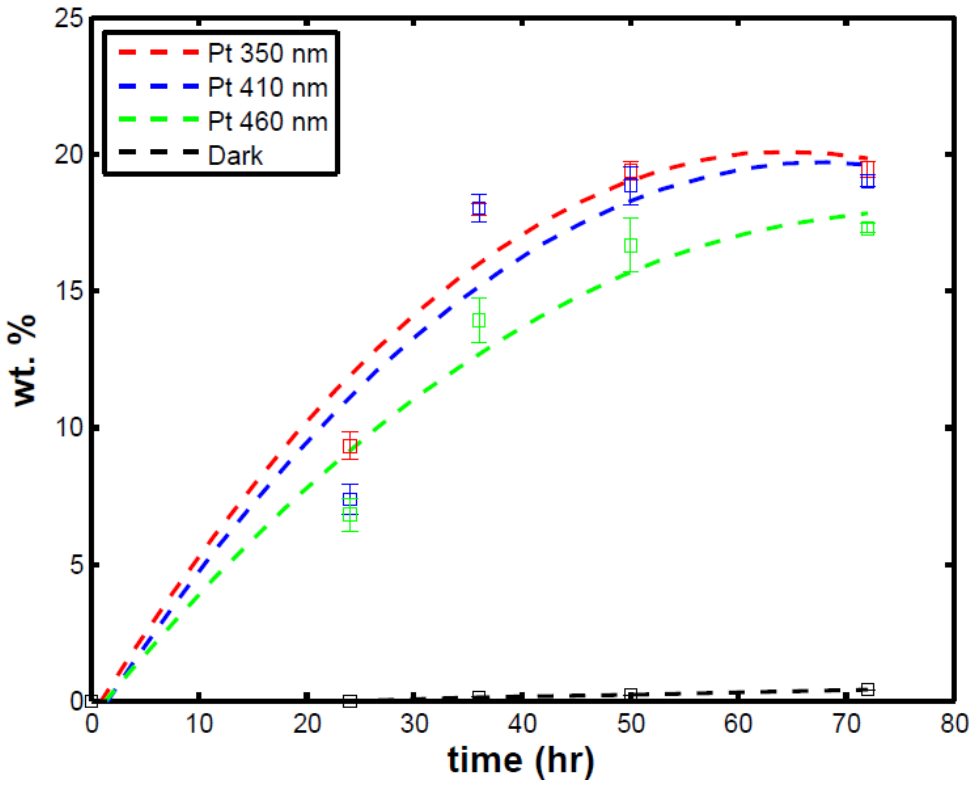

Figure 5.11: Platinum metal weight loading as a function of time for nanoparticles photodeposited at various wavelengths. The loading plateaued at ~ 20% due to the complete consumption of platinum precursor materials. Samples run under dark conditions showed negligible deposition in comparison to those run under illumination.

Due to the poor plasmonic response of platinum, the time evolution of the platinum photodeposition process could not be tracked using UV-vis spectroscopy, and it was not possible to correlate the platinum particle nanostructure with the illumination wavelength. The nanoparticles photodeposited at 350, 410, and 460 nm all had a similar dark blue color (Figure 5.12), suggesting they possessed comparable geometry and size after 72 h.

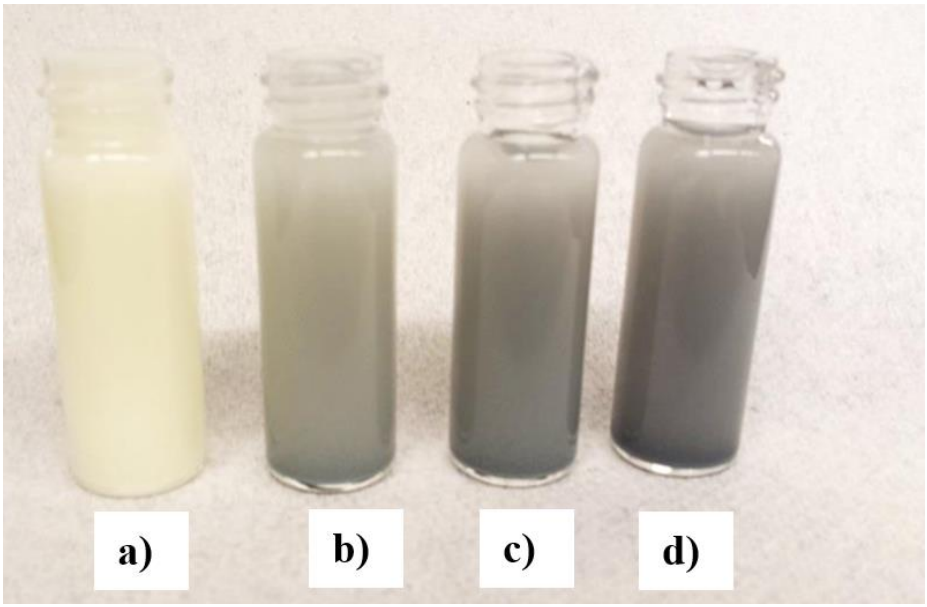

Figure 5.12: Photographs of nanoparticles photodeposited at various wavelengths: a) no illumination, b) 350 nm, c) 410 nm, d) 460 nm. Similarities in the coloration suggest similarities in nanoparticle geometry and size.

5.3.4 Catalytic Reaction Tests: Crotonaldehyde Hydrogenation

The catalytic activities of the photodeposited silver, gold, and platinum nanoparticles were evaluated for the hydrogenation of crotonaldehyde. Table 5.2 summarizes the reactivities and corresponding H_2 dissociation energies for each of the M/WO_3 catalysts. No catalytic activity was observed for WO_3, Au/WO_3, or Ag/WO_3. Touroude et al. reported that the limiting step for crotonaldehyde hydrogenation reactions was the dissociation of molecular hydrogen [25]. The lack of hydrogenation activity is attributable to the positive hydrogen dissociation energies for WO_3 [26], Au, and Ag [27], which present a thermodynamic barrier to the hydrogenation of crotonaldehyde. Touroude et al. also showed that gold nanoparticles below 4 nm in size could dissociate molecular hydrogen due to an increased fraction of low-index crystallographic planes [25]. As mentioned earlier, crystallite sizes of as-synthesized gold nanoparticles in our study were 7.8, 7.2, and 7.2 nm for nanoparticles photodeposited at 350, 410, and 460 nm, respectively. These sizes increased to 15.8, 12, and 10 nm, respectively, after

pretreatment of the materials in flowing hydrogen. Therefore, the size of our gold nanoparticles was too large to be able to dissociate molecular hydrogen. Our attempts to reduce the size of the photodeposited gold nanoparticles through varying the initial gold precursor concentration were unsuccessful.

Table 5.2: Activities and molecular H_2 dissociation energies for the M/WO_3 catalysts. Only Pt catalysts show thermodynamically favorable energies for dissociating H_2.

Catalyst	**WO_3**	**Au/WO_3**	**Ag/WO_3**	**Pt/WO_3 (350 nm)**	**Pt/WO_3 (410 nm)**	**Pt/WO_3 (460 nm)**
Activity at 8 h (μmol/h/mg)	0	0	0	0.185	0.345	0.195
H_2 dissociation energy (eV)	0.436 [25]	1.21 [27]	1.18 [26]	-0.813 [27]	-0.813 [27]	-0.813 [27]

The XRD patterns for pretreated silver materials before and after hydrogenation reactions are shown in Figure 5.13. The silver nanoparticles were still undetectable by XRD, suggesting that the silver remained amorphous or that there was no significant sintering in the materials following reduction in hydrogen, and the materials were unaffected by the hydrogenation reaction. In the future, it may be possible to identify other reactions that the silver and gold nanoparticles are capable of catalyzing.

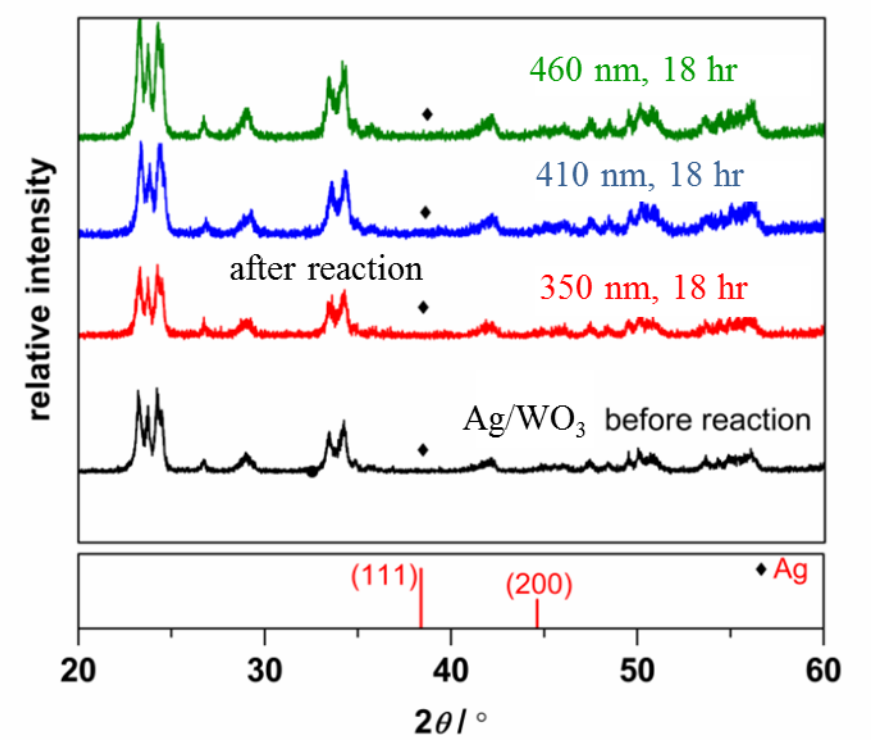

Figure 5.13: XRD patterns for silver nanoparticles after pretreatment in hydrogen and after hydrogenation reactions. No evidence of sintering was observed; neither were the nanoparticles changed by the reactions.

Because Pt has a negative hydrogen dissociation energy, Pt/WO_3 was the only material that resulted in measurable hydrogenation activity. The selectivity towards hydrogenation products of Pt/WO_3 materials synthesized at 410 nm is shown in Figure 5.14. Similar results were obtained using materials synthesized at 350 and 460 nm. The hydrogenation reactions were carried out for up to 12 h. The selectivity towards crotyl alcohol increased between 0 and eight hours but decreased after 12 h, likely due to the formation of non-hydrogenated products, such as hemiacetals, at longer reaction times. Therefore, all future hydrogenation reactions were run for 8 hours. Butyraldehyde was the other major hydrogenation product. Butanol, the full hydrogenation product, was only produced in small amounts and had a selectivity less than 8%. These results demonstrate that Pt/WO_3 was highly selective for the partial hydrogenation of crotonaldehyde and is a good candidate for the hydrogenation of other α,β-aldehydes.

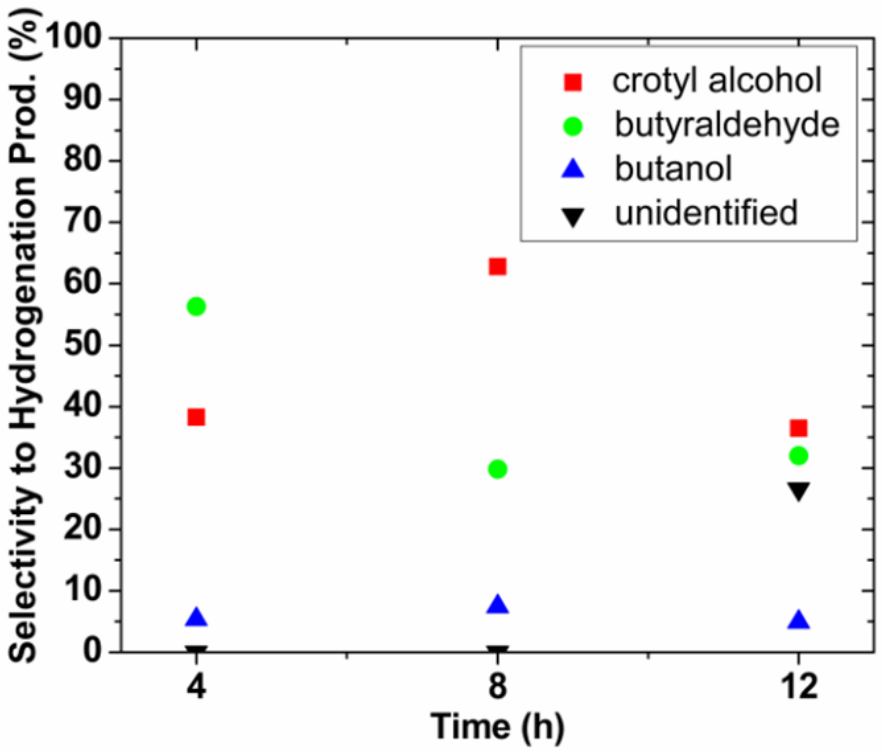

Figure 5.14: Selectivity of Pt/WO_3 materials synthesized at 410 nm towards hydrogenation products. The highest selectivity towards crotyl alcohol fell after 8 h.

The product selectivities of the Pt/WO_3 materials synthesized at 350, 410, and 460 nm for reaction times of eight hours are shown in Figure 5.15. The selectivity towards crotyl alcohol was around 60% for materials photodeposited at 350 and 410 nm and ~45% for materials photodeposited at 460 nm. The similarities in the selectivities of these materials were due to similarities in the platinum geometry. However, the total crotyl alcohol product as a function of time for the 410 nm Pt/WO_3 catalyst was approximately twice as high as that for either the 350 or 460 nm Pt/WO_3 catalysts (Figure 5.16). TEM micrographs (Figure 5.17) suggest that this difference is due to considerable agglomeration of Pt following synthesis at 350 or 460 nm, resulting in nanoparticle clusters more than 100 nm in diameter. In comparison, nanoparticles from materials synthesized at 410 nm were much less agglomerated, with diameters less than 50

nm. The reasons for the agglomeration are not clear but might be a consequence of slight differences between the plasmonic response of Pt at 410 nm and those at 350 and 460 nm.

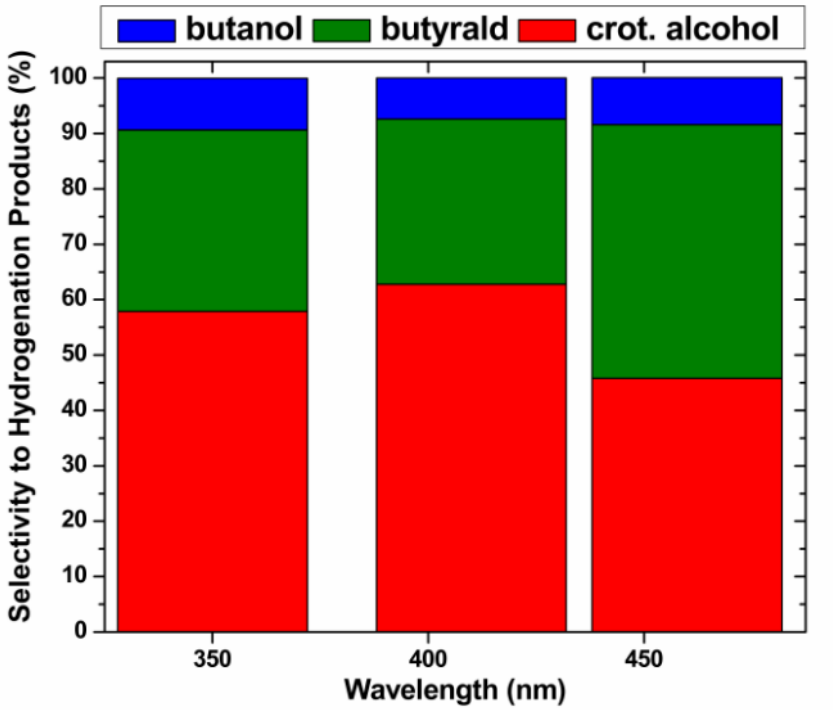

Figure 5.15: Product selectivities of the Pt/WO_3 materials synthesized at 350, 410, and 460 nm for reaction times of 8 h. The roughly similar selectivities observed were due to similarities in the Pt particle geometry.

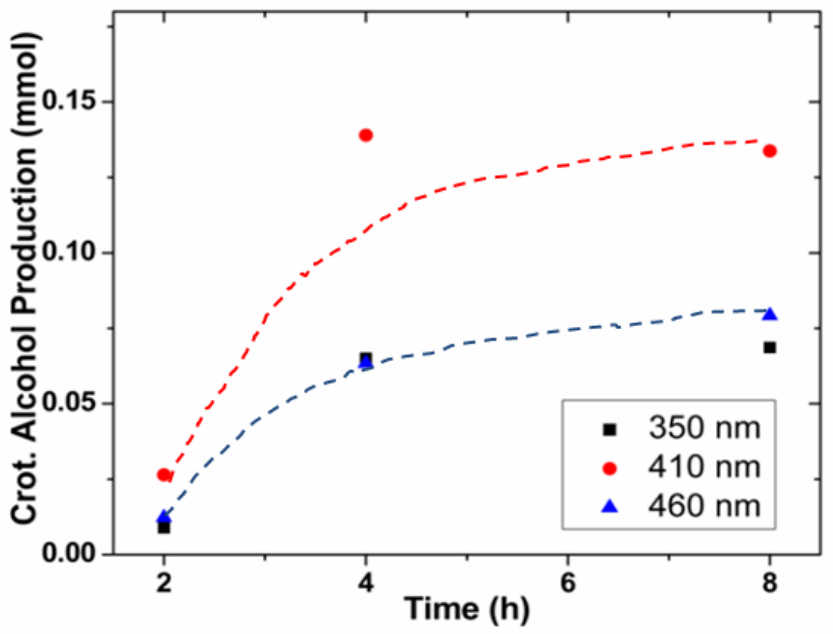

Figure 5.16: Crotyl alcohol formation as a function of time for the Pt nanoparticles synthesized at 350, 410, and 460 nm. Approximately twice the amount of crotyl alcohol was formed by the materials synthesized at 410 nm than those synthesized at 350 and 410 nm. Dashed lines were added to guide the eye.

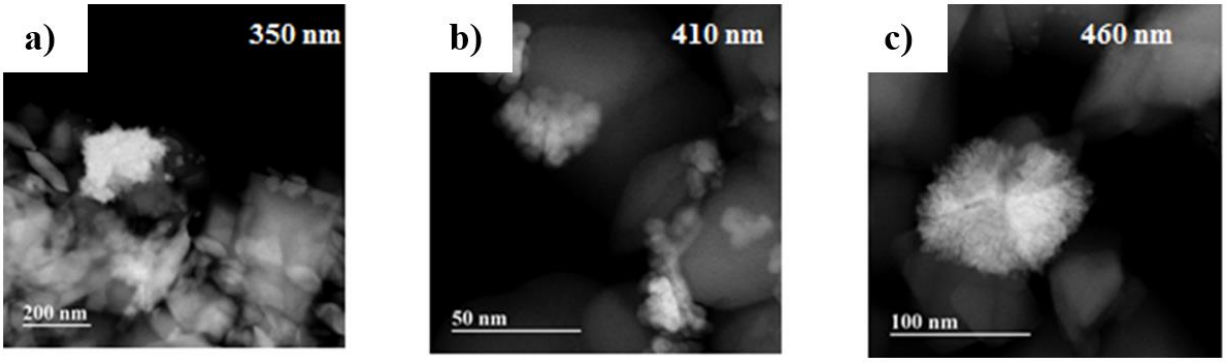

Figure 5.17: TEM micrographs for Pt nanoparticles photodeposited at a) 350, b) 410, and c) 460 nm. Considerable agglomeration of Pt nanoparticles was observed for materials synthesized at 350 and 460 nm.

5.4 Summary and Conclusions

In this chapter, we demonstrated the photodeposition of silver, gold, and platinum nanoparticles on a WO_3 support. Through a statistical analysis, ANOVA, we identified the key parameters affecting the photodeposition process. The noble metal loading was shown be strongly correlated to the illumination time and metal precursor concentration. The changes in the plasmonic response of the noble metals during the photodeposition process were monitored using UV-vis spectroscopy. The absorbance spectra were observed to broaden and become red-shifted with illumination time, indicating that the nanoparticle sizes were increasing. The illumination wavelength did not affect the metal loading. However, the geometry of the photodeposited nanoparticles could be tuned by varying the illumination wavelength. Spherical, pentagonal, and hexagonal gold nanoparticles, as well as spherical and cuboid silver nanoparticles, were achieved.

The photodeposited materials were evaluated for the selective hydrogenation of crotonaldehyde, which is a model reaction for unsaturated α,β-aldehyde hydrogenation. The limiting step in hydrogenation is the dissociation of molecular hydrogen. The Ag/WO_3 and Au/WO_3 materials were not active for crotonaldehyde hydrogenation due to their unfavorable hydrogen dissociation energies. However, the Pt/WO_3 materials were active and exhibited similar selectivities towards crotyl alcohol for materials synthesized at all our deposition wavelengths. This was attributed to similarities in the size and geometry of these materials. Pt nanoparticles photodeposited at 410 nm showed higher product yield to crotyl alcohol than did Pt nanoparticles photodeposited at 350 and 460 nm. This was a result of the materials synthesized at 410 nm having smaller Pt particle sizes, as compared to those synthesized at 350 or 460 nm, which showed considerable agglomeration. Results from this study were expected to assist the

development of simple synthesis techniques for the design of noble metal catalysts with controlled nanostructure for unsaturated α,β-aldehyde hydrogenation and other reactions of interest.

5.5 References

[1] Claus, P.; Hofmeister, H.; Electron Microscopy and Catalytic Study of Silver Catalysts: Structure Sensitivity of the Hydrogenation of Crotonaldehyde. *J. Phys. Chem. B.* **1999**, *103*, 2766.
[2] Liu, J.; Chen, F. Plasmon Enhanced Photoelectrochemical Activity of Ag-Cu Nanoparticles on TiO_2/Ti Substrates. *Int. J. Electrochem. Sci.* **2012**, *7*, 9560.
[3] Iwamoto, M. Air Pollution Abatement through Heterogeneous Catalysis. *Studies Surf. Sci. Catal.* **2000**, *130*, 23.
[4] J. N. Armor. A History of Industrial Catalysis. *Catal. Today* **2011**, *163*, 3.
[5] Zaera F. Nanostructured Materials for Applications in Heterogeneous Catalysis. *Chem. Soc. Rev.* **2013**, *42*, 2746.
[6] Xu, R.; Wang, D.; Zhang, J.; Li, Y. Shape-Dependent Catalytic Activity of Silver Nanoparticles for the Oxidation of Styrene. *Chem. Asian J.* **2006**, *1*, 888.
[7] Sun, Y.; Xia, Y. Shape-Controlled Synthesis of Gold and Silver Nanoparticles. *Science* **2002**, *298*, 2176.
[8] Jin, R. C.; Cao, Y. W.; Mirkin, C. A.; Kelly, K. L.; Schatz, G. C.; Zheng, J. G. Photoinduced Conversion of Silver Nanospheres to Nanoprisms, *Science* **2001**, *294*, 1901.
[9] Stamplecoskie, K. G.; Scaiano, J. C. Light Emitting Diode Irradiation Can Control the Morphology and Optical Properties of Silver Nanoparticles, *J. Am. Soc.* **2010**, *1325*, 1825.
[10] Rycenga, M.; Cobley, C. M.; Zeng, J.; Li, W.; Moran, C. H.; Zhang, Q.; Qin, D.; Xia, Y. Controlling the Synthesis and Assembly of Silver Nanostructures for Plasmonic Applications. *Chem. Rev*. **2011**, *111*, 3669.
[11] Englisch, M.; Jentys, A.; Lercher, J. A. Structure Sensitivity of the Hydrogenation of Crotonaldehyde over Pt/SiO_2 and Pt/TiO_2, *J. Catal*. **1997**, *166*, 25.
[12] Periana, R. A.; Taube, D. J.; Gamble, S.; Taube, H.; Satoh, T.; Fujii, H. Platinum Catalysts for the High-Yield Oxidation of Methane to a Methanol Derivative. *Science* **1998**, *280*, 560.
[13] Wolfe, D. B.; Oldenburg, S. J.; Westcott, S. L.; Jackson, J. B.; Paley, M. S.; Halas, N. J. Photodeposition of Molecular Layers on Nanoparticle Substrates. *Langmuir* **1999**, *15*, 2745.
[14] Willets, K. A.; Van Duyne, R. P. Localized Surface Plasmon Resonance Spectroscopy and Sensing. *Annu. Rev. Phys. Chem.* **2007**, *58*, 267.
[15] Gupta, P.; Ramrakhiani, M. Influence of the Particle Size on the Optical Properties of CdSe Nanoparticles. *The Open Nanoscience Journal* **2009**, *3*, 15.
[16] Zangeneh, F. T.; Taeba, A.; Gholivanda, K.; Sahebdelfar, S. Kinetic Study of Propane Dehydrogenation and Catalyst Deactivation over $Pt\text{-}Sn/Al_2O_3$ Catalyst. *Journal of Energy Chemistry* **2013**, *22*, 726.[17] Usman, M. R.; Aslam, R.; Saleem, M. Chemical Engineering Terminology, Revised Edition. *Lulu Enterprises, Inc*. **2015**.
[18] Wang, G.; Schaidle, J. A.; Katz, M. B.; Li, Y.; Pan, X. Alumina Supported Pt–Mo_2C Catalysts for the Water–gas Shift Reaction. *Journal of Catalysis* 2**013**, *304*, 92.
[19] Winer, B. J. Statistical Principles in Experimental Design. *McGraw-Hill Kogakusha, Ltd*. **1971**, Second Edition.
[20] Amendola, V.; Bakr, O. M. A Study of the Surface Plasmon Resonance of Silver Nanoparticles by the Discrete Dipole Approximation Method: Effect of Shape, Size, Structure, and Assembly. *Plasmonics* **2010**, *5*, 85.
[21] Balzar, D.; Audebrand, N.; Daymond, M. R.; Fitch, A.; Hewat, A.; Langford, J. I.; Le Bail, A.; Louer, D.; Masson, O.; McCowan, C. N.; Popa, N. C.; Stephens, P. W.; Toby, B. H. Size-Strain Line-Broadening Analysis of the Ceria Round-Robin Sample. *J. Appl. Cryst.* **2004**, *37*, 911.

[22] Thimsen, E.; Le Formal, F.; Gratzel, M.; Warren, S. C. Influence of Plasmonic Au Nanoparticles on the Photoactivity of Fe_2O_3 Electrodes for Water Splitting. *Nano Lett*. **2011**, *11*, 35.
[23] Xue, C.; Metraux, G. S.; Millstone, J. E.; Mirkin, C. A. Mechanistic Study of Photomediated Triangular Silver Nanoprism Growth. *J. Am. Chem. Soc*. **2008**, *130*, 8337.
[24] Xue, C.; Millstone, J. E.; Li, S.; Mirkin, C. A. Plasmon-Driven Synthesis of Triangular Core-Shell Nanoprisms from Gold Seeds. *Angew. Chem. Int. Ed*. **2007**, *46*, 8436.
[25] Zanella, R.; Louis, C.; Giorgio, S.; Touroude, R. Crotonaldehyde Hydrogenation by Gold Supported on TiO_2: Structure Sensitivity and Mechanism, *J. Catal*. **2004**, *223*, 328.
[26] Song, J.; Huang, Z. –F.; Pan, L.; Zou, J.; Zhang, X.; Wang, L. Oxygen-Deficient Tungsten Oxide as Versatile and Efficient Hydrogenation Catalyst. *ACS Catal*. **2015**, *5*, 6594.
[27] Pozzo, M.; Alfe, D.; Amieiro, A.; French, S.; Pratt, A. Hydrogen Dissociation and Diffusion on Ni- and Ti-doped Mg Surfaces. *J. Chem. Phys.* **2008**, *128*, 094703.

Chapter 6

Summary, Conclusions, and Recommendations for Future Work

6.1 Summary and Conclusions

Materials with precisely controlled nanostructures are needed to significantly enhance the efficiencies of next-generation systems for chemical conversions and energy storage. This dissertation sought to identify simple techniques of controlling nanostructure for catalytic and electrochemical energy storage materials. The result was a set of nanostructure-function relationships for three material systems: hematite (α-Fe_2O_3) nanotube arrays for photoelectrochemical water oxidation, orthorhombic niobium pentoxide (T-Nb_2O_5) planar and nanotube array electrodes for Li^+ ion intercalation, and photodeposited noble metal (Ag, Au, Pt) nanoparticles for the selective hydrogenation of α,β-unsaturated aldehydes. These relationships should inform efforts to design and synthesize materials with superior performance. In addition to providing new insights into the synthesis and properties of the nanostructured materials, the research presented in this dissertation reaffirmed reports by other researchers.

Electrodes of α-Fe_2O_3 with controlled structure and dimensions were fabricated via the electrochemical anodization of high-purity iron foils in electrolytic solutions containing ammonium fluoride, ethylene glycol, and water. During fabrication, the current response of the films was tracked to characterize the growth process. Four distinct stages were identified with regard to the evolution of the nanotube arrays: an ohmic response stage, an oxide film formation stage, a chemical dissolution/pitting stage, and a steady-state growth stage. Morphological,

optical, and photoelectrochemical properties of the electrodes were characterized using X-ray diffraction (XRD), scanning electron microscopy, UV-vis diffuse reflectance spectroscopy, linear sweep voltammetry, electrochemical impedance spectroscopy, and incident photon to current efficiency (IPCE) measurements. The IPCE of the wave-like nanotube arrays at 350 nm was ~3 times that of the single layer nanotube arrays and ~12 times that for the multilayer nanotube arrays. Charge carrier transport and the active electrochemical surface areas of the different α-Fe_2O_3 morphologies were identified as underlying causes of the differences in the photocatalytic performance.

Nb_2O_5 nanotubular electrodes were synthesized via the electrochemical anodization of high-purity niobium foils in electrolytes containing ammonium fluoride, glycerol, and water. Nb_2O_5 planar electrodes were fabricated in a similar manner, except the anodization process was halted before the onset of the chemical dissolution stage. Li^+ intercalation into the electrodes was analyzed using XRD, charge/discharge measurements, and inductively coupled plasma spectroscopy. Charge storage in the amorphous Nb_2O_5 was negligible compared to that for the T-Nb_2O_5, revealing the key role played by the crystallinity of the electrodes in the charge storage mechanism. Li^+ intercalation was shown to favor the low energy {180} family of crystallographic planes. The nanotube array T-Nb_2O_5 electrodes exhibited a four-fold increase in the specific charge storage capacity when compared to planar electrodes. This performance difference was explained by the greater accessibility of the (180) planes in the nanotube array morphology. Moreover, reduced Li^+ ion diffusion limitations were observed in the nanotube array electrodes due to the short diffusion lengths. On the other hand, transport limitations were observed in planar electrodes at high charging rates due to long diffusion length scales.

Light at varying wavelengths was used to control the photodeposition of noble materials on tungsten trioxide (WO_3) supports. The noble metal particle sizes and total metal loadings were strong functions of the illumination time, while nanoparticle shape was controlled by the illumination wavelength. Intrinsic variations in the plasmonic responses of the noble materials across the UV-vis spectrum allowed for control of the nanoparticle shapes. These photodeposited materials were evaluated for the selective hydrogenation of crotonaldehyde, a model α,β-unsaturated aldehyde, and the results were correlated with key nanostructural properties of the noble metal particles. Pt/WO_3 catalysts were active for the hydrogenation of crotonaldehyde, with similar selectivities (~60%) towards crotyl alcohol for materials photodeposited at 350, 410, and 460 nm. Pt photodeposition at 350, 410, and 460 nm resulted in nanoparticle agglomeration, with diameters over 100, 30, and 100 nm, respectively. Selectivities were similar because all three materials were spherical. However, Pt/WO_3 catalysts synthesized at 410 nm showed a higher conversion to crotyl alcohol than those photodeposited at 350 and 460 nm. This may be due to the smaller Pt particle sizes for materials deposited at 410 nm, which would result in a higher surface area exposed for chemical reaction. The reason for the differences in the nanoparticle sizes for materials synthesized at different wavelengths was not established but could be linked to slight differences in the plasmonic response of Pt. No crotonaldehyde hydrogenation activity was observed for either Au/WO_3 or Ag/WO_3 catalysts. Literature reports suggest that this was a result of the high thermodynamic barriers to the dissociation of molecular hydrogen that are associated with these catalysts [1-2].

6.2 Limitations of Current Research and Recommendations for Future Work

6.2.1 Limitations of Current Research

Our work provided a foundation for future experiments to further understand the impact of nanostructure on materials' functionality. The conclusions reached in this dissertation were based on results from a variety of experimental techniques. As discussed in Chapter Three, one technique (Mott-Schottky analysis) had fundamental limitations when applied to single layer, multilayer, and wave-like hematite nanotube arrays. The mathematical derivations involved in Mott-Schottky analysis assume a smooth, planar electrode [3]. To date, there is no theoretical framework to extend the application of this analysis to complex nanostructured geometries such as nanotube arrays. Our analysis of single layer, multilayer, and wave-like nanotube arrays yielded results that were not meaningful for a comparison of charge photo-generation across morphologies. This was likely due to complications such as extra roughness in the wave-like nanotube arrays and the interfaces in the multilayer nanotube arrays [3]. As such, experiments that utilized Mott-Schottky analysis warrant further experimental investigation and/or the use of alternative analysis techniques. One possible approach is to apply a re-formulated Mott-Schottky analysis. Hansen reported significant progress in the development of a new theoretical formulation that would allow the extension of the Mott-Schottky method to nanostructured materials [4]. The authors demonstrated the accurate application of a modified analysis to nanoporous titania electrodes synthesized by anodization. Though their results are preliminary and require further interpretation, they suggest that a proper mathematical treatment that takes nanostructural geometry into account might yield useful results from Mott-Schottky analysis.

Other techniques, such as terahertz time domain spectroscopy [5], are also worth considering for the measurement of charge carrier generation. However, the geometry

dependence of this technique is not well established. The development of novel techniques and new theoretical frameworks will be crucial for a full analysis of charge photogeneration in complex electrodes.

6.2.2 Recommendations for Future Work

6.2.2.1 Silicon-doped Hematite for Photocatalysis

The study of the optical properties of hematite revealed two bandgaps of 1.9 and 2.4 eV. Although both bandgaps are energetically sufficient to drive the water photo-oxidation reaction, photocatalytic efficiency (IPCE) measurements showed that only the 2.4 eV bandgap was efficiently utilized for water oxidation. In their studies of silicon-doped dendritic hematite nanostructures, Durrant et al. concluded that avoiding the ultrafast electron-hole recombination was crucial for optimizing the utilization of photogenerated charge carriers [6]. They demonstrated that electron trapping in localized states in the space-charge layer of hematite competed with electron-hole recombination and therefore facilitated the efficient transfer of holes to the semiconductor-electrolyte interface. In essence, the dopants increased the density of localized states associated with the 1.9 eV bandgap in hematite, thus slowing the recombination process and allowing for photogenerated charges to be utilized for water oxidation. Durrant et al. hypothesized that the presence of dopants in hematite nanowires was the reason for the significant enhancement in the photocatalytic performance of hematite nanowires over undoped nanowires that was reported by Li et al [7]. An easy and inexpensive technique to dope nanostructured hematite materials with controlled concentrations of silicon is dip coating. For instance, Braun et al. used a dip-coating method to add a layer of a tetra ethyl ortho-silicate precursor to iron oxide electrodes. Subsequent thermal treatment steps at 500 and 760 °C for 30 minutes in air for each step allowed them to dope up to 8 wt. % Si into the iron oxide crystal

lattices. At 2 wt. % dopant levels, the silicon-doped hematite electrodes exhibited enhanced photocurrent generation (0.9 mA/cm^2) over the pristine hematite electrodes (0.4 mA/cm^2) at 1.3 V *vs.* the reversible hydrogen electrode [8]. The application of a similar technique to our hematite nanotube arrays could lead to the efficient utilization of photons absorbed by both the direct and indirect bandgaps of hematite.

6.2.2.2 Mg^{2+} Intercalation in Nb_2O_5

This dissertation explored the application of nanostructured Nb_2O_5 for Li^+ ion storage. Over the last few years, magnesium (Mg^{2+}) has gained increasing attention as an attractive alternative to Li^+ [9]. The divalent nature of Mg^{2+} promises the achievement of higher energy densities (as high as 300 mAh/g [10]) than monovalent Li^+. However, a basic understanding of the thermodynamics governing Mg^{2+} intercalation chemistry is lacking. Moreover, the development of electrolytes that are compatible with magnesium intercalation materials is still in its infancy [11]. Efforts to understand Mg^{2+} intercalation include the work of Zhang et al., who demonstrated the insertion of Mg^{2+} ions into V_2O_5 in aprotic electrolytes with capacities as high as 160 mAh/g [12]. Because the polymorphs of Nb_2O_5 are similar to those of V_2O_5, and the diameter of Mg^{2+} ions (1.30 Å) is smaller than the inter-planar spacing (2.98 A) of the low-energy (180) planes where Li^+ ion intercalation occurred, it should be possible to extend the Li^+ intercalation work we demonstrated in Nb_2O_5 to Mg^{2+} and achieve higher energy densities.

6.2.2.3 Nanostructured Nb_2O_5 / Carbon Nanotube Hybrid

The T-Nb_2O_5 nanotube array electrodes that we developed for electrochemical energy storage (described in Chapter Four) did not contain any conductivity additives. Because T-Nb_2O_5 is insulating, with an electrical conductivity of ~$3x10^{-6}$ S/cm [13], the incorporation of a conductive network of carbon with the electrode materials could significantly improve the

capacity and rate capability of the materials. Chen et al. designed a hybrid nanomaterial of hematite nanoparticles wrapped in carbon nanotubes that exhibited more than double the discharge capacity of bare hematite nanoparticles [14]. The carbon nanotubes were created by the oxidation of Fe nanoparticles in a carbon dioxide atmosphere. The electrochemical performance improvement was due to a five-fold increase in the conductivity of the hybrid nanostructure due to the conductive carbon network. Similarly, a carbon nanotube network on Nb_2O_5 could enhance the capacity and rate performance of the electrodes.

6.2.2.4 Single-Crystal Nb_2O_5

In Chapter Four, we hypothesized that poly-crystallinity in the planar Nb_2O_5 morphology caused the misalignment of the (180) planes of adjacent crystallites, resulting in the blockage of these low diffusion energy channels and reduced specific capacity. The development of single-crystal planar electrodes might increase overall capacities and rate capabilities to levels similar to those achieved using the nanotube array morphology. This would improve the gravimetric capacitance of the planar electrodes over that of nanotube array electrodes, increasing the practical significance of nanostructured Nb_2O_5 for electrochemical storage applications. However, growing single crystals is extremely difficult; a calcination procedure that results in single-crystalline materials after synthesis using the electrochemical anodization technique is yet to be reported. Some literature reports have shown that the development of single-crystalline Nb_2O_5 nanostructures is possible using a hydrothermal technique [15-16]. An interesting study to carry out would be to investigate the feasibility of achieving single-crystalline Nb_2O_5 nanomaterials using electrochemical anodization followed by a calcination procedure.

6.2.2.5 Identifying Reactions Catalyzed by Ag/WO_3 and Au/WO_3

Our investigations of the use of Ag/WO_3 and Au/WO_3 catalysts for the selective hydrogenation of crotonaldehyde showed negligible activity for these materials. The rate-limiting step for the hydrogenation reaction is the dissociation of molecular hydrogen, a reaction that these catalysts are ineffective for. However, Ag/WO_3 has been found to effectively catalyze various oxidation reactions. For instance, Bal et al. reported a 99% selectivity (and 55% conversion) in the room temperature selective oxidation of cyclo-octene to cyclo-octene oxide over Ag nanoparticles supported on WO_3, in the presence of hydrogen peroxide [17]. The same authors also reported Ag/WO_3 catalysts to be active in the selective oxidation of styrene. This would be an interesting target for the Ag/WO_3 catalysts.

Cho and co-workers performed density functional theory calculations to characterize the adsorption of NO molecules on clean WO_3 surfaces, as well as on Ag-deposited and Au-deposited WO_3 surfaces [18]. They showed thermodynamically favorable energies for the adsorption of NO molecules on WO_3 (−0.48 eV), Ag/WO_3 (−1.41 eV), and Au/WO_3 (−1.32 eV) catalysts. Noble metals have been shown to be active in the catalytic reduction of NO_x gases from vehicle exhausts [19]. The nanostructure-controlled noble metal catalysts synthesized in this dissertation could be applied towards the catalytic reduction of NO_x gases.

6.2.2.6 Synthesis of Nanostructured Bimetallic Catalysts

Another interesting prospect is the use of shape-controlled bimetallic catalysts. Bimetallic catalysts have been shown to exhibit higher catalytic activities than catalysts with a single active species [20]. The catalytic enhancements have partly been attributed to synergistic effects between the various active species [20]. Leclercq et al. demonstrated the photocatalytic deposition of well-dispersed noble metal (Pt, Pd, Ag, Rh, Au, Ir, Cu) nanoparticles on various

photosensitive supports, including oxides (TiO_2, Nb_2O_5, ZrO_2, ZnO) and sulfides (CdS) [21]. Under similar experimental conditions (50 mg TiO_2 in 10 cm^3 1 mM metal salt solution), they established a general pattern for the ease of photodeposition of the noble metals on TiO_2: Ag > Pd > Au > Pt >> Ir >> Cu = Ni = 0 [21]. As shown in Figure 5.2, Ag, Pd, Au and Pt all have strong plasmonic responses in the UV-vis spectrum, which allows them to easily grow once a nucleus is formed. There are no studies on the surface plasmon resonance of Ir, likely because it is immeasurably low, which would explain its poor photodeposition in Leclercq's study. The lack of Ni deposition on TiO_2 was attributed to the misalignment of the flat band potentials of TiO_2 with the redox potential of the Ni^{2+}/Ni^0 couple [21]. Leclercq's one surprising finding was the failure to photodeposit Cu, given the strong surface plasmonic response of the metal in the UV-vis spectrum. Leclercq suggested the re-oxidation of metallic Cu to Cu^+ on opening the photodeposition reactor as an explanation for this observation [21]. It might also be possible that solution conditions, such as the pH, might affect the growth of the Cu nuclei during photodeposition. Further experimental studies with variations to solution conditions are suggested to better understand the photodeposition of Cu. Similar noble metal photodeposition trends were reported for different semiconducting supports [21].

Leclercq et al. also explored the synthesis of bimetallic catalysts (Pt-Pd, Pd-Ag, Pt-Ir) on TiO_2, with reported alloy formation based on TEM results [21]. For the various noble metal combinations, the only case where there was incomplete photodeposition of the materials was Pt-Ir; only 80% of the Pt and 20% of the Ir were deposited. These results were consistent with experimental findings for the photodeposition rates of the noble metals in the absence of other metals [21]. This suggests that the successful synthesis of bimetallic catalysts can be simply extended from the synthesis of single metal catalysts. However, the synthesis of nanostructure-

controlled bimetallic catalysts is poorly understood. This presents an exciting new opportunity to investigate a large combination of noble metals on various photoactive supports for a wide range of catalytic applications. We can extend the synthesis techniques developed in this dissertation towards the synthesis of nanostructure-controlled bimetallic catalysts.

6.3 Conclusion

This chapter presented a summary of key research findings and conclusions for the three materials systems investigated in this thesis. The research described in this dissertation contributes to the understanding of the behavior of nanostructured materials when applied to photocatalysis (hematite), electrochemical energy storage (niobium pentoxide), and heterogeneous catalysis (Ag/WO_3, Pt/WO_3, Au/WO_3) and confirmed the findings of other researchers. This dissertation employed simple but powerful synthesis techniques to control the nanostructure of different material classes. Nanostructure-function relationships were elucidated for the aforementioned materials systems.

Limitations of this research and recommendations for future experiments are also discussed. We identified several exciting pathways the research presented herein could take. For instance, the doping of the hematite nanostructures we synthesized with silicon was suggested as a possible way of utilizing both the direct and indirect bandgaps of hematite, allowing for enhanced photocatalytic performance. We also recommended lining Nb_2O_5 nanotube arrays synthesized in this work with carbon nanotubes to enhance the rate capabilities and experimenting with Mg^{2+} ion intercalation to increase the energy densities of these materials. Even though it is a major challenge, research on the synthesis of Nb_2O_5 single crystals was suggested to isolate favorable ion diffusion pathways, thereby increasing the storage capacity. Moreover, since we were able to control the nanostructure of Ag/WO_3 and Au/WO_3 materials,

but the materials were inactive for the hydrogenation of crotonaldehyde, the identification of alternative reactions where these catalysts can be applied, such as in NO_x reduction, was suggested. Finally, the opportunity to investigate the photodeposition of a variety of noble metals and different bimetallic combinations on several photoactive supports was identified. Controlling the nanostructure of these materials will help understand how their structures affect their functions in various chemical reactions, which could have a tremendous effect on the field of catalysis. Ultimately, the insights from this work and the extensions we recommended, will facilitate the development of general design rules for the synthesis of materials with precisely controlled nanostructures, which will be needed to achieve significantly greater efficiencies required for next-generation devices for heterogeneous catalysis and energy conversion/storage.

6.4 References

[1] Zanella, R.; Louis, C.; Giorgio, S.; Touroude, R. Crotonaldehyde Hydrogenation by Gold Supported on TiO_2: Structure Sensitivity and Mechanism, *J. Catal.* **2004**, *223*, 328.

[2] Pozzoa, M.; Alfèa, D. Hydrogen Dissociation and Diffusion on Transition Metal-doped Mg(0001) Surfaces. *Int. J. Hydrogen Energ.* **2009**, *34*, 1922.

[3] Cardon, F.; Gomes, W. P. On the Determination of the Flat-band Potential of a Semiconductor in Contact With a Metal or an Electrolyte From the Mott-Schottky Plot. *J. Phys. D: Appl. Phys.* **1978**, 11, L63.

[4] Hansen, J. E. M. Analysis of an Impedance Model for Porous Semiconductor Electrodes, PhD Thesis – Norwegian University of Science and Technology, **2012**.

[5] Nashima, S.; Morikawa, O.; Takata, K.; Hangyo, M. Measurement of Optical Properties of Highly Doped Silicon by Terahertz Time Domain Reflection Spectroscopy. *Appl. Phys. Lett.* **2001**, *79*, 3923.

[6] Pendlebury, R. S.; Wang, X.; Le Formal, F.; Cornuz, M.; Kafizas, A.; Tilley, S. D.; Grätzel, M.; Durrant, J. R. Ultrafast Charge Carrier Recombination and Trapping in Hematite Photoanodes under Applied Bias. *J. Am. Chem. Soc.* **2014**, *136*, 9854.

[7] Ling, Y.; Wang, G.; Reddy, J.; Wang, C.; Zhang, J. Z.; Li, Y. The Influence of Oxygen Content on the Thermal Activation of Hematite Nanowires. *Angew. Chem. Int. Ed.* **2012**, *51*, 4074.

[8] Hu, Y.; Bora, D. K.; Boudoire, F.; Haussler, F.; Graetzel, M.; Constable, E. C.; Braun, A. A Dip Coating Process for Large Area Silicon-Doped High Performance Hematite Photoanodes. *Journal of Renewable and Sustainable Energy*. **2013**, *5*, 043109.

[9] Chang, Z.; Yang, Y.; Wang, X.; Li, M.; Fu, Z.; Wu, Y.; Holze, R. Hybrid System for Rechargeable Magnesium Battery with High Energy Density. *Scientific Reports* **2015**, *5*, 11931.

[10] Orikasa, Y.; Masese, T.; Koyama, Y.; Mori, T.; Hattori, M.; Yamamoto, K.; Okado, T.; Huang, Z-D.; Minato, T.; Tassel, C.; Kim, J.; Kobayashi, Y.; Abe, T.; Kageyama, H.; Uchimoto, Y. High Energy Density Rechargeable Magnesium Battery Using Earth-Abundant and Non-toxic Elements, *Scientific Reports* **2014**, *4*, 5622.

[11] Levi, E.; Gofer, Y.; Aurbach, D. On the Way to Rechargeable Mg Batteries: The Challenge of New Cathode Materials. *Chem. Mater.* **2010**, *22*, 860.

[12] Yu, L.; Zhang, X. Electrochemical Insertion of Magnesium Ions into V_2O_5 from Aprotic Electrolytes with Varied Water Content. *J. Colloid. Interface Sci.* **2004**, *278*, 160.

[13] Rani, R. A; Zoolfakar, A. S.; O'Mullane, A. P.; Austin, M. W.; Kalantar-Zadeh, K. Thin Films and Nanostructures of Niobium Pentoxide: Fundamental Properties, Synthesis Methods and Applications. *J. Mater. Chem. A.* **2014**, 2, 15683.

[14] Yan, N.; Zhou, X.; Li, Y.; Wang, F.; Zhong, H.; Wang, H.; Chen, Q. Fe_2O_3 Nanoparticles Wrapped in Multi-walled Carbon Nanotubes With Enhanced Lithium Storage Capability. *Scientific Reports* **2013**, 3, 3392.

[15] Liu, J.; Xue, D. Single-Crystalline Nanoporous Nb_2O_5 Nanotubes. *Nanoscale Res Lett.* **2011**, *6*, 138.

[16] Zhang, H; Wang, Y..; Liu, P.; Chou, S. L.; Wang, J. Z.; Liu, H.; Wang, G.; Zhao, H. Highly Ordered Single Crystalline Nanowire Array Assembled Three-Dimensional $Nb_3O_7(OH)$ and Nb_2O_5 Superstructures for Energy Storage and Conversion Applications. *ACS Nano.* **2016**, *10*, 507.

[17] Ghosh, S.; Acharyya, S. S.; Kumar, M.; Bal, R. One-pot Preparation of Nanocrystalline Ag–WO_3 Catalyst for the Selective Oxidation of Styrene. *RSCAdv*. **2015**, *5*, 37610.

[18] Ren, X.; Zhang, S.; Li, C.; Li, S.; Jia, Y.; Cho, J. Catalytic Activities of Noble Metal Atoms on WO_3 (001): Nitric Oxide Adsorption. *Nanoscale Res Lett.* **2015**, *10*, 60.
[19] Sakamoto, Y.; Matsunaga, S.; Okumura, K.; Kayama, T.; Yamazaki, K.; Takahashi, N.; Tanaka, T.; Kizaki, Y.; Motohiro, T.; Shinjoh, H. Effect of Precious Metals and NO_x Storage Materials on Hydrogen Reduction of Stored NO_x on Millisecond Time Scale. *Applied Catalysis A: General* **2012**, *445*, 133.
[20] Sankar, M.; Dimitratos, N.; Miedziak, P. J.; Wells, P. P.; Kiely, C. J.; Hutchings, G. J. Designing Bimetallic Catalysts for a Green and Sustainable Future. *Chem. Soc. Rev.* **2012**, *41*, 8099.
[21] Herrmann, J.; Disdier, J.; Pichati, P.; Leclerq, C. Photo-assisted Deposition of Noble Metals: Investigation of a New Route for Metallic and Bi-metallic Catalyst Preparation. *Stud. Surf. Sci. Catal.* **1987**, *31*, 285.